

---

DIRECT ELECTRON TRANSFER  
TO CYTOCHROME C OXIDASE  
INVESTIGATED BY ELECTROCHEMISTRY  
AND TIME-RESOLVED SURFACE-ENHANCED  
INFRARED ABSORPTION SPECTROSCOPY

---

DISSERTATION  
ZUR ERLANGUNG DES AKADEMISCHEN GRADES  
"DOKTOR DER NATURWISSENSCHAFTEN"  
AM FACHBEREICH 09 DER  
JOHANNES GUTENBERG UNIVERSITÄT IN MAINZ

DENISE SCHACH  
GEBOREN AM 02. JUNI 1984 IN MAINZ

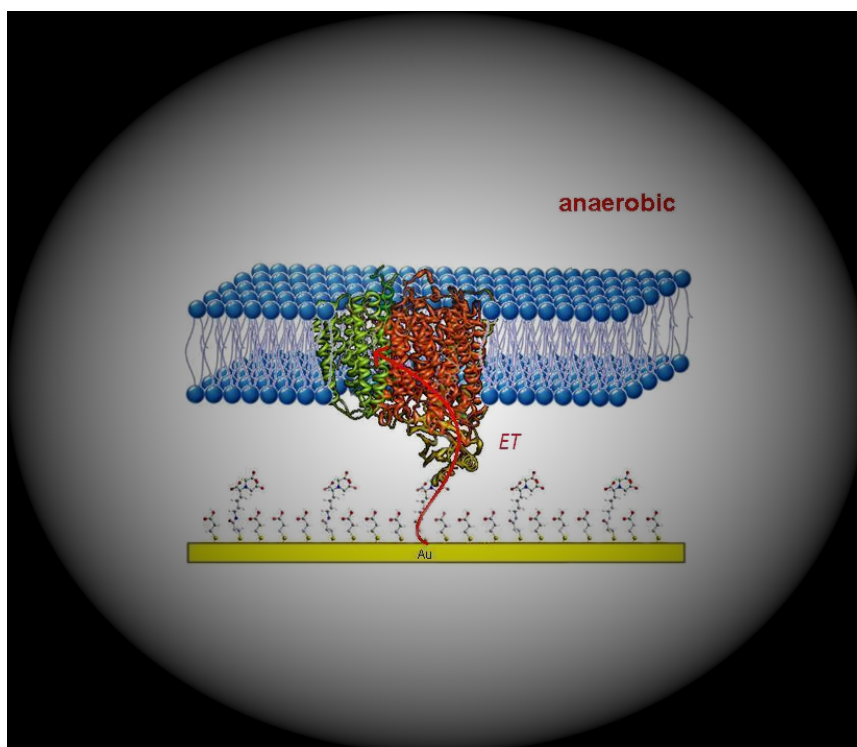
MAY, 2011



---

DIRECT ELECTRON TRANSFER  
TO CYTOCHROME C OXIDASE  
INVESTIGATED BY ELECTROCHEMISTRY  
AND TIME-RESOLVED SURFACE-ENHANCED  
INFRARED ABSORPTION SPECTROSCOPY

---



Die vorliegende Arbeit wurde am Max-Planck-Institut für Polymerforschung in Mainz sowie am Austrian Institute of Technology in Wien im Zeitraum zwischen März 2009 und Mai 2011 angefertigt.

**Betreuung durch:**

**Dekan:**

**1. Gutachter:**

**2. Gutachter:**

**Tag der mündlichen Prüfung:**



## Erklärung

Hiermit versichere ich, dass ich die vorliegende Arbeit selbstständig verfasst und keine anderen als die angegebenen Quellen und Hilfsmittel benutzt habe, dass alle Stellen der Arbeit, die wörtlich oder sinngemäß aus anderen Quellen übernommen wurden, als solche kenntlich gemacht sind und dass die Arbeit in gleicher oder ähnlicher Form noch keiner Prüfungsbehörde vorgelegt wurde.

Wien, den 01.05.2011

.....

## Abstract

Cytochrome c Oxidase (CcO), which is complex IV of the respiratory chain is a member of the superfamily of heme-copper containing terminal oxidases, and plays a crucial role in the metabolism of cells. The protein complex contains four prosthetic groups and is located in the inner membrane of mitochondria and the cell membrane of many aerobic bacteria. It catalyzes the transfer of electrons from cytochrome c to molecular oxygen, being available for the intrinsic reaction that takes place in the  $\text{Cu}_B$ -heme  $a_3$  binuclear center. A consumption of four protons to form two water molecules per oxygen molecule ( $\text{O}_2$ ) is connected to an electrogenic translocation (pumping) of four protons per reaction cycle across the membrane, thus generating a difference in electrochemical potential of protons between matrix and intermembrane space. Despite their significance membrane proteins, such as CcO are still not much investigated. As a result the mechanism of the respiratory chain is not yet fully understood.

It is the aim of this thesis to extend the fundamental understanding of the functionality of CcO. Therefore, CcO from *Rhodobacter sphaeroides* was tethered to the functionalized metal electrode in a strict orientation, by means of a his-tag engineered to the C-terminus of subunit II. The first electron acceptor is directed towards the metal surface. A lipid bilayer was then reconstituted in-situ around the bound proteins, forming a protein-tethered bilayer lipid membrane (ptBLM). For this purpose the ideal mixing ratio of linking and spacing molecules had to be found. Electrochemical impedance spectroscopy (EIS), surface plasmons resonance spectroscopy (SPR) as well as cyclic voltammetry (CV) were applied to characterize the activity of CcO as a function of the packing density. Another aim of the thesis is to investigate direct electron transfer to CcO. The combination of time-resolved surface-enhanced infrared-absorption spectroscopy (tr-SEIRAS) and electrochemistry has shown to be valuable in this context. Direct electron transfer was therefore investigated using fast scan cyclic voltammetry. Cyclic voltammograms were measured at different scan rates with CcO in the non-activated and the activated state. The activated state was obtained after catalytic turnover of the protein in presence of oxygen. A four-electron transfer model was then designed to analyze the cyclic voltammograms. This method enables us to discriminate between the mechanism of sequential and independent electron transfer to the four redox centers  $\text{Cu}_A$ , heme a, heme  $a_3$  and  $\text{Cu}_B$ . Furthermore, values such as redox potentials and kinetic coefficients of electron transfer could be obtained. Based on these results we can conclude, that direct electron transfer to CcO most likely follows the sequential mechanism thus mimicking the electron transfer from cytochrome c, the genuine electron donor of CcO. On the basis of these results we utilized tr-SEIRAS in the step scan mode to extend the scope of the investigation into the time domain. For this purpose, periodic potential pulses were applied to CcO. SEIRAS in the ATR mode was used to obtain spectra within defined time slides. It was the aim of this project to gain information about vibrational modes of amino acids and peptide groups in conjunction with redox transitions. Bands were tentatively assigned to the redox centers on the basis of data obtained by potentiometric titrations of CcO, e.g. [184]. Band areas, indicating the redox kinetics of the centers were then plotted against time. Four-ET model was again fitted to the data to obtain the specific standard redox potentials and kinetic coefficients. The results of both studies give strong evidence for the sequential electron transfer that is natural to the enzyme.

## Zusammenfassung

Cytochrom c Oxidase (CcO), der Komplex IV der Atmungskette, ist eine der Häm-Kupfer enthaltenden Oxidasen und hat eine wichtige Funktion im Zellmetabolismus. Das Enzym enthält vier prosthetische Gruppen und befindet sich in der inneren Membran von Mitochondrien und in der Zellmembran einiger aerober Bakterien. Die CcO katalysiert den Elektronentransfer (ET) von Cytochrom c zu  $O_2$ , wobei die eigentliche Reaktion am binuklearen Zentrum ( $Cu_B$ -Häm  $a_3$ ) erfolgt. Bei der Reduktion von  $O_2$  zu zwei  $H_2O$  werden vier Protonen verbraucht. Zudem werden vier Protonen über die Membran transportiert, wodurch eine elektrochemische Potentialdifferenz dieser Ionen zwischen Matrix und Intermembranphase entsteht. Trotz ihrer Wichtigkeit sind Membranproteine wie die CcO noch wenig untersucht, weshalb auch der Mechanismus der Atmungskette noch nicht vollständig aufgeklärt ist.

Das Ziel dieser Arbeit ist, einen Beitrag zum Verständnis der Funktion der CcO zu leisten. Hierzu wurde die CcO aus *Rhodobacter sphaeroides* über einen His-Anker, der am C-Terminus der Untereinheit II angebracht wurde, an eine funktionalisierte Metallelektrode in definierter Orientierung gebunden. Der erste Elektronenakzeptor, das  $Cu_A$ , liegt dabei am nächsten zur Metalloberfläche. Dann wurde eine Doppelschicht aus Lipiden in situ zwischen die gebundenen Proteine eingefügt, was zur sog. proteingebundenen Lipid-Doppelschicht Membran (ptBLM) führt. Dabei musste die optimale Oberflächenkonzentration der gebundenen Proteine herausgefunden werden. Elektrochemische Impedanzspektroskopie (EIS), Oberflächenplasmonenresonanzspektroskopie (SPR) und zyklische Voltammetrie (CV) wurden angewandt um die Aktivität der CcO als Funktion der Packungsdichte zu charakterisieren. Der Hauptteil der Arbeit betrifft die Untersuchung des direkten ET zur CcO unter anaeroben Bedingungen. Die Kombination aus zeitaufgelöster oberflächenverstärkter Infrarot-Absorptionsspektroskopie (tr-SEIRAS) und Elektrochemie hat sich dafür als besonders geeignet erwiesen. In einer ersten Studie wurde der ET mit Hilfe von fast scan CV untersucht, wobei CVs von nicht-aktivierter sowie aktivierter CcO mit verschiedenen Vorschubgeschwindigkeiten gemessen wurden. Die aktivierte Form wurde nach dem katalytischen Umsatz des Proteins in Anwesenheit von  $O_2$  erhalten. Ein vier-ET-modell wurde entwickelt um die CVs zu analysieren. Die Methode erlaubt zwischen dem Mechanismus des sequentiellen und des unabhängigen ET zu den vier Zentren  $Cu_A$ , Häm a, Häm  $a_3$  und  $Cu_B$  zu unterscheiden. Zudem lassen sich die Standardredoxpotentiale und die kinetischen Koeffizienten des ET bestimmen. In einer zweiten Studie wurde tr-SEIRAS im step scan Modus angewandt. Dafür wurden Rechteckpulse an die CcO angelegt und SEIRAS im ART-Modus verwendet um Spektren bei definierten Zeitscheiben aufzunehmen. Aus diesen Spektren wurden einzelne Banden isoliert, die Veränderungen von Vibrationsmoden der Aminosäuren und Peptidgruppen in Abhängigkeit des Redoxzustands der Zentren zeigen. Aufgrund von Zuordnungen aus der Literatur (z.B. [184]), die durch potentiometrische Titration der CcO ermittelt wurden, konnten die Banden versuchsweise den Redoxzentren zugeordnet werden. Die Bandenflächen gegen die Zeit aufgetragen geben dann die Redox-Kinetik der Zentren wieder und wurden wiederum mit dem vier-ET-Modell ausgewertet. Die Ergebnisse beider Studien erlauben die Schlussfolgerung, dass der ET zur CcO in einer ptBLM mit großer Wahrscheinlichkeit dem sequentiellen Mechanismus folgt, was dem natürlichen ET von Cytochrom c zur CcO entspricht.

# Contents

<b>1</b>	<b>Introduction</b>	<b>1</b>
<b>2</b>	<b>Motivation</b>	<b>3</b>
<b>3</b>	<b>Cytochrome c Oxidase and its Environment</b>	<b>6</b>
3.1	Biological Membranes and Lipids . . . . .	7
3.2	Respiratory Chain and Phosphorilation . . . . .	8
3.3	Structure and Function . . . . .	11
3.4	Catalytic Cycle . . . . .	14
3.5	Electron and Proton Pathways . . . . .	17
<b>4</b>	<b>Artificial Membrane Systems</b>	<b>21</b>
<b>5</b>	<b>Methods</b>	<b>23</b>
5.1	Surface Plasmon Resonance . . . . .	23
5.2	Electrochemistry . . . . .	27
5.2.1	The Electrical Double Layer . . . . .	27
5.2.2	Electrochemical Impedance Spectroscopy . . . . .	28
5.2.3	Cyclic Voltammetry . . . . .	32
5.2.4	ET Model for the Analysis of CcO CVs . . . . .	36
5.2.4.1	General Concept . . . . .	36
5.2.4.2	Electron Transfer at Pseudo-Equilibrium . . . . .	38
5.2.4.3	Sequential Electron Transfer (ECCC Mechanism) . . . . .	39
5.2.4.4	Independent Electron Transfer (EEEE Mechanism) . . . . .	39
5.3	Infrared Spectroscopy . . . . .	40
5.3.1	Absorption of Light . . . . .	40
5.3.2	General Concept . . . . .	41
5.3.2.1	Molecular Vibrational Modes . . . . .	44
5.3.2.2	Classical Model for Stretching Vibrations . . . . .	45
5.3.2.3	Quantum Mechanical Model for Stretching Vibrations . . . . .	46
5.3.3	Infrared Spectroscopy with Proteins . . . . .	49
5.3.3.1	Amide Bands . . . . .	49
5.3.4	Fourier-transform Infrared Spectrometers . . . . .	50
5.3.5	Surface Enhancement Effect . . . . .	53
5.3.6	Time-Resolved Surface Enhanced Infrared Absorption Spectroscopy (tr-SEIRAS) . . . . .	56
5.3.7	Combination of tr-SEIRAS and Electrochemical Excitation of CcO by means of Square Wave Potential Pulses . . . . .	58
5.3.7.1	Analysis of the Redox Kinetics . . . . .	59
5.3.8	Model Simulation and Parameter Fitting . . . . .	60
<b>6</b>	<b>Results and Discussion</b>	<b>61</b>
6.1	Oriented Immobilization of Cytochrome c Oxidase . . . . .	61
6.1.1	Electrochemical Impedance Spectroscopy at Different Surface Concentrations . . . . .	62
6.1.2	Cyclic Voltammetry of CcO at Different Surface Concentrations . . . . .	65

6.1.3	Surface Plasmon Resonance . . . . .	67
6.1.4	Summary and Conclusion . . . . .	68
6.2	Activation of CcO . . . . .	70
6.2.1	Summary and Conclusion . . . . .	72
6.3	Analysis of Fast Scan Cyclic Voltammograms of CcO using multistep-ET models . . . . .	74
6.3.1	Activated CcO . . . . .	74
6.3.2	Non-Activated CcO . . . . .	76
6.3.3	Summary and Conclusion . . . . .	78
6.4	Time-Resolved Surface-Enhanced Infrared Spectroscopy of CcO . . . . .	80
6.4.1	Anaerobic Conditions . . . . .	80
6.4.1.1	Activated CcO . . . . .	80
6.4.1.2	Non-Activated CcO . . . . .	89
6.4.2	Aerobic Conditions . . . . .	89
6.4.3	Summary and Conclusion . . . . .	92
<b>7</b>	<b>Overall summary</b>	<b>94</b>
<b>8</b>	<b>Materials and Methods</b>	<b>96</b>
8.1	Preparation of Samples . . . . .	96
8.1.1	Ultraflat Gold Surfaces: Template Stripped Gold . . . . .	96
8.1.2	Two-Layer Gold Surface . . . . .	96
8.1.3	Immobilization of the Protein . . . . .	96
8.2	Measuring Cells, Setups and Methods . . . . .	98
8.2.1	Surface Plasmon Resonance . . . . .	98
8.2.2	Electrochemistry . . . . .	99
8.2.3	Spectro-Electrochemistry . . . . .	99
8.2.3.1	Time-Resolved (tr) Surface-Enhanced IR Absorption Spectroscopy (SEIRAS) . . . . .	101
8.3	Chemicals . . . . .	103
8.4	Materials and Machines . . . . .	104
<b>9</b>	<b>Symbols</b>	<b>106</b>
<b>10</b>	<b>Acronyms and Abbreviations</b>	<b>108</b>
<b>11</b>	<b>Appendix</b>	<b>110</b>
.1	Curriculum Vitae . . . . .	110
.2	List of Publications . . . . .	111

---

# 1 Introduction

Proteins were first mentioned by the Dutch chemist Gerhardus Johannes Mulder and named by the Swedish chemist Jöns Jakob Berzelius in 1838. Believing that "flesh makes flesh", early nutritional scientists predicted the essential importance of proteins as nutrients for maintaining the tissue of the body [186]. Yet, the society did not become aware of the significance of proteomics until the mid-1950s, when the first protein, insulin, was sequenced by Frederick Sanger. He won the Nobel Prize for this achievement in 1958. In the same year, Max Perutz and Sir John Cowdery Kendrew solved the structures of hemoglobin and myoglobin, respectively [148][149]. It was the beginning of x-ray crystallography for resolving three-dimensional protein structures. Both scientists were honored with the Nobel Prize in Chemistry in 1962. In the course of time, various techniques for protein purification have been established. This achievement made accessible research of protein structure and functionality. Nowadays, methods such as immunohistochemistry, site-directed mutagenesis, nuclear magnetic resonance, mass- and optical spectroscopy as well as x-ray crystallography are commonly used. In 1971, the Protein Data Bank (PDB) was set up by Walter Hamilton and in the past, the number of structures in the PDB has grown at an approximately exponential rate. Nevertheless, since 2007, the rate of accumulation of new proteins seems to have plateaued, with about 7,000 new entries per year [203].

Inspired by the evolutionary optimized specificity and efficiency of proteins, scientists design artificial systems including these biological molecules for technological applications. Since the early 1970s, the real impact of enzymes as analytical tools was felt [127]. One example for an enzyme which serves as an analytical tool is Glucose Oxidase. Glucose Oxidase can be used for the selective determination of glucose. Clinical and industrial applications for Glucose Oxidase have been commercialized in the recent years, particularly as analytical products for diabetes patients and the food processing industry. The latest challenge in this field of research seems to be integrating membrane proteins as analytical tool into biosensors and lab-on-a-chip (LOC) devices.

The fundamental significance of protein function and interaction for the vitality of organisms is a further reason to investigate proteins. More than half of all proteins interact with lipid membranes and approximately 25-30 % are predicted to be embedded in biological membranes [21][76]. However, membrane proteomics is still not much investigated and experimental accessibility of membrane proteins remains challenging due to their amphiphilic character and the difficulties occurring when purifying, crystallizing, solubilizing, stabilizing and identifying them. As indication for that serves a simple comparison between the total number of published protein structures in the PDB (state: August 2010) which is more than 67,000 whereas the total number of published membrane protein structures which is only about 684. The complexity of handling membrane proteins might also be a reason for the above mentioned stagnation of PDB entries per year. Membrane proteins perform diverse functions in cells, including signal transduction, energy conversion, enzymatic catalysis, detoxification and transport of electrons, protons or other ions. Dependent on the functionality, membrane proteins can be classified. Transporter and channel proteins help establish and control the ion gradient across the plasma membrane of cells, enzymes catalyze processes of metabolism, receptor proteins are involved in signal transduction, connexins assemble to form gap junctions and so on. Additionally, particular enzymes account for two key reactions of biochemistry: res-

piration and photosynthesis [170]. It is easily imaginable that dysfunction of membrane proteins leads to diseases. Considering for example a metabolic rate of ATP of about 80 kg per day for a human being, the essential role of the involved enzymes becomes obvious [203]. It is already known that for instance defects in the respiratory chain can induce fatal health detriments. Affected organs can be the central nervous system [163], skeletal muscles, retina, heart, kidney and liver [53]. They all have in common a highly active metabolism. Diseases including cancer, epilepsy, dementia and cardiac insufficiency have been attributed to defects in the respiratory chain [163][53][29].

One particular membrane-bound enzyme involved in respiration is Cytochrome c Oxidase (CcO), also denoted as complex IV. It is the terminal complex of the respiratory chain of mitochondria and many aerobic bacteria. This multi-redox site protein contains the four redox centers  $\text{Cu}_A$ , heme a, heme  $a_3$  and  $\text{Cu}_B$ . It catalyzes the electron transfer (ET) from reduced cytochrome c to molecular oxygen ( $\text{O}_2$ ) which is reduced to water at the catalytic center.  $\text{Cu}_A$  is the first electron acceptor and is reduced by cytochrome c. A potential gradient between the redox centers gives rise to a transfer of electrons to heme a and the catalytic center which consists of heme  $a_3$  and  $\text{Cu}_B$ . The enzyme consumes four substrate protons from the matrix per  $\text{O}_2$  in the synthesis of water. Moreover, four additional protons are pumped across the membrane, which causes a net charge separation of four charges per turnover [193]. Thus the free energy gained from the oxidation of cytochrome c by  $\text{O}_2$  is used for the generation of an electrochemical potential difference for protons across the inner mitochondrial membrane (for a detailed description of functionality see section 3).

---

## 2 Motivation

Electrochemistry had proved to be powerful for the investigation of electron transfer (ET) mechanisms in multi-redox site proteins. Protein films were adsorbed onto gold or carbon electrodes and were investigated by means of fast scan voltammetry [5][4][6]. In the case of adsorbed species, a one-step electrochemical reaction can be analyzed by means of the Butler-Volmer equation. For this purpose, Laviron developed a method which can be used for the analysis of data obtained from linear potential sweep voltammetry [97]. This is known as the trumpet plot in which peak potentials are plotted against the log of scan rate. ET to various redox proteins has been analyzed by means of the trumpet plot [5][4][41]. Catalytic activity of proteins in the presence of substrates, however, was investigated employing the rotating disc electrode [5][4][3]. The reduction of the catalytic center was treated as a chemical reaction following an electron uptake via a number of redox centers. By means of the Jellyfit software, square wave voltammograms have been simulated [6]. However, the program operates with a considerable number of simplifications so that it allows for only two fit parameters, namely the redox potential  $E_o$  and the electrochemical rate constant  $k_s$  of the catalytic center.

As an alternative to these methods our group introduced a system that opens the possibility for the complete analysis of multi-step ET reactions initiated by direct ET to the first electron acceptor of a redox chain. A redox enzyme of the respiratory chain, CcO from *R. sphaeroides*, was adsorbed to an electrode in a strict orientation by means of a histidine (his)-tag engineered onto the enzyme. A lipid bilayer was then reconstituted in-situ around the bound proteins, forming a protein-tethered bilayer lipid membrane (ptBLM) [88][66]. Direct ET to CcO had previously shown to take place employing cyclic voltammetry, surface-enhanced resonance Raman spectroscopy (SERRS) and surface-enhanced Infrared absorption spectroscopy (SEIRAS). Four electrons were shown to be taken up by the redox centers of the enzyme. Moreover, the enzyme was shown to be catalytically active in the presence of oxygen [135]. Potentiometric titrations were performed under anaerobic conditions followed by SEIRAS. Evidence for conformational changes in the protein backbone was gained from this study. Two states of CcO, the activated and the non-activated, could be identified [132]. It was the aim of this work to find the exact conditions for the transformation into the activated state. Since CcO is attached via his-tag at the C-terminus of the SU II to the electrode,  $Cu_A$  is directed towards the metal surface. A parameter that seems to be important for the effective ET is the protein packing density. The packing density is determined by the surface concentration of chelator molecules containing a terminal nitrilo-triacetic acid group (NTA). These molecules were prepared in-situ from a surface-bound active ester (DTSP) according to a previous publication of our group [88]. Since the control over the surface concentration using in-situ synthesis is unsatisfactory, the chelator molecules (DTNTA) were now synthesized ex-situ. The metal surface will therefore be functionalized by means of a self-assembled monolayer of DTNTA and dithio-dipropionic acid (DTP) with a defined mixing ratio. The mixing ratio determines the final surface concentration of proteins. It is the next aim of this work to find the optimum mixing ratio and consequently packing density of proteins. For this purpose cyclic voltammetry will be applied to analyze the ET kinetics. Catalytic activity can be used as a guiding principle in this study. Fast scan voltammetry over a wide range of scan rates will be used for both, the non-activated and activated state. A further part of this work is to investigate the entire four-electron transfer mechanism to



CcO in the applied configuration. The protein must be investigated in the absence of  $O_2$ . The Mechanisms of ET excited by electrochemical reduction to and within the protein was not investigated so far. The primary aim of this study was the elucidation of the mechanism. It is a great advantage of our method, that the redox state of the enzyme in our studies can be manipulated by externally applied potentials. This will allow us to analyze the details of ET mechanisms to and within the protein. Two possible mechanisms will be taken into consideration, the sequential mechanism, an ECCC process, and the independent ET mechanism, an EEEE process.

The combination of electrochemistry with vibrational spectroscopy, such as Fourier-transform infrared (FTIR) spectroscopy, had been used before for the investigation of multi-redox proteins. Potentiometric titrations were performed using CcO which was solubilized in a buffer solution [122][121][82]. Information about conformational changes as a function of redox transitions could be obtained [199][126][82][84][122]. The ET to the redox centers was thereby mediated by means of soluble redox systems [122]. These studies could only give information on static but not dynamic processes. The time-resolved (tr) spectroscopy, however, could extend the scope of the investigations into the time domain. Tr-optical absorption studies have been applied to study intramolecular ET in CcO [58][68][108][144][31][176]. The photodissociation of CO bound to the mixed-valence and the fully reduced enzyme was followed in some of these studies [31][176]. The ET processes were found to take place on the nano- to milli-second time scales. Various studies, including tr-vibrational spectroscopy, i.a. based on the photodissociation of ligands such as CO, CN or NO. By means of tr-resonance Raman (RR), heme  $a_3$  iron-bound oxy-, ferryl-, and hydroxyl intermediates could be identified [156][86][85]. The tr-FTIR spectroscopy, however, was employed to study the protein kinetics as a function of photodissociation and recombination of CO adducts of CcO [30][61][183]. A time resolution on the micro-second time scale was achieved. Photodissociation of CO has additionally been investigated by means of laser photolysis of CO adducts in the fully reduced species or the mixed valence state species [30][61][62]. However, these studies were not designed to investigate the entire sequence of ET steps to and within the protein by time-resolved vibrational spectroscopy.

Therefore, in addition to the electrochemical investigations, we applied tr-SEIRAS, which is based on the repeated recording of spectra over defined time slides. Direct ET offers the possibility to change the redox state repeatedly between oxidized and reduced state by applying periodic potential pulses at different frequencies and to measure spectra as a function of time. tr-SEIRAS can provide an access to the kinetics of redox induced structural changes. The application of the step-scan mode requires the recording of a large number of spectra as a function of time, hence the oxidation and reduction has to be repeated frequently. For this reason, the system has to be considered stable over a certain number of excitations. We expect from the spectra to contain vibrational modes of amino acids and peptide groups coupled to redox transitions occurring in the absence of oxygen. The time-dependent change of absorbance band intensities of the difference spectra responds to the applied potential, thus yielding information about the ET kinetics. Bands occurring in the spectra can then be assigned to the vibrational modes that were found in potentiostatic titrations [184]. Since the amino acid and peptide environments of the single redox centers contribute individual modes, the tr-SEIRAS allows to analyze the responses from each redox center separately. This is essential for the analysis of the kinetics of every single ET step. The final aim of this work was to find

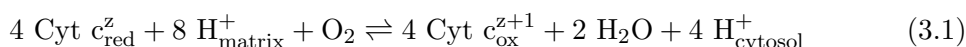
---

out whether or not tr-SEIRAS confirms the results obtained from fast scan voltammetry.

This is particularly interesting for further studies of the enzyme operating under turnover conditions, i.e. in the presence of oxygen. Differences in the conformational transitions of peptide groups in the absence and presence of oxygen can give insight into the mechanisms of electron and proton transfer in this enzyme.

### 3 Cytochrome c Oxidase and its Environment

Being the terminal complex in the respiratory chain of mitochondria and aerobic bacteria, Cytochrome c Oxidase (CcO) catalyzes ET from cytochrome c to molecular oxygen which is reduced to water. To this end, the enzyme consumes four substrate protons of the matrix per one molecular oxygen ( $O_2$ ) in the synthesis of water molecules. Connected to this reaction four additional protons are pumped across the membrane, thus generating a net charge separation of four charges per turnover. As a consequence, a membrane potential of about 160 mV is generated which, together with a pH difference of about 1 unit, constitutes the proton motive force [9] that is utilized by the  $H^+$ /ATP synthase to synthesize ATP from ADP and  $P_i$ . The reaction catalyzed by CcO can be summarized in



Since the reductive chemistry of oxygen takes place in the  $Cu_B$ -heme  $a_3$  binuclear center, CcO is counted among the superfamily of structurally and functionally homologous enzymes, the heme-copper oxidases. The enzyme is present in the inner membranes of eukaryotic mitochondria as well as in the inner cell membrane of prokaryotes.

The history of investigations on CcO began in 1925, when D. Keilin at Cambridge University discovered the cytochromes [79]. At that time, his findings were the missing link connecting the theories of Otto H. Warburg's "Atmungsferment" [189] and Heinrich O. Wieland's dehydrogenase in conjunction with the source of energy in living cells. It was the discovery of the electron transport chain [39]. It took until 1938, when the bands corresponding to cytochrome  $a_3$  were identified, it was possible to attribute cytochrome oxidase to Warburg's predicted "Atmungsferment" [39]. During the following two decades the aerobic energy transduction attracted various scientists bringing forward an enormous progress. However, during that time the enzymatic processes were not fully understood in a broader context. The significance of the membrane was not realized yet (see subsection 3.1). The first new spectroscopic observations of CcO were made in 1959, when R. Sands and R. Beinert recorded EPR spectra of the enzyme at the temperature of liquid nitrogen [13]. In the late 1960s, Peter Mitchell contributed a further important piece of the puzzle by publishing the chemiosmotic hypothesis, which earned him the Nobel Prize for Chemistry in 1978 [120]. With the help of J. Moyle, Mitchell developed a theory that explained the energetic coupling of ATP synthesis to the respiratory chain by means of an electrochemical potential difference of protons across the inner membrane [119]. The discovery of the ATP synthase could confirm Mitchell's theory. From that time on, the electron transfer chain earned the appropriate attention being accepted as the generator for proton gradients across the membrane, the driving force for the ATP synthesis. In 1977, Marten Wikstroem discovered the important role of CcO as a redox-driven proton pump [200]. Few enzymes have ever been investigated as intensively as CcO. An entire book [160] has been dedicated only to the structure and function of CcO and meetings have been organized just to discuss this particular protein [16].

Many important details and mechanisms have already been understood, however, various questions concerning issues of bioenergetics and of biochemistry still remain unanswered. The principle of proton translocation, for example, is not yet fully understood on the molecular level [194].

### 3.1 Biological Membranes and Lipids

Biological membranes consist of lipid bilayers and embedded proteins, such as peripheral and integral species (see figure 3.1) [25][136]. It is known from literature that the amount of proteins in a lipid membrane can account for up to 50 % [95]. Enclosing cellular organelles and sealing the cells itself from the external environment, the biological membranes play a crucial role in the physiology of living cells. Various types of evolutionary optimized membranes exist for different organelles and cell types or even the same organelles in different organs. Basically, they differ in lipid and protein composition. In 1967, S. Fleischer reported that heart mitochondria, for instance, contain nearly twice as much lipid as those from liver [94]. Lipids help to maintain electrochemical potential differences between two functional volumes of the cell and special lipids bound to the protein warrant a tight between protein and lipid bilayer even while proteins undergo activity-related conformational changes [188]. Particularly with regard to gradients across the

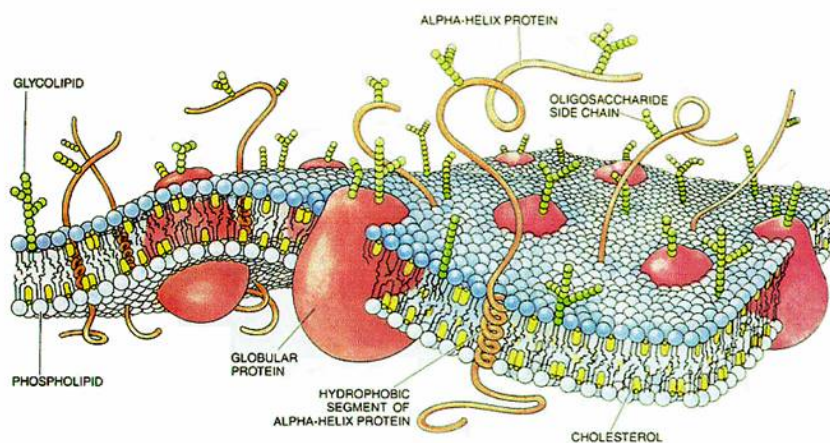


Figure 3.1: Scheme of a cell membrane.[203]

membrane, the properties of lipids have been shown to be indispensable to the viability of mitochondria [40]. In addition, lipids are important for signaling functions and the correct folding of membrane proteins. They are even essential for the protein functionality [33][98]. Since the lipid bilayer is a fluid matrix [168][136], both lipids and incorporated proteins show mobility driven by lateral diffusion. The mobility allows the enzymes to form distinct domain structures. The lipid composition has been shown to be responsible for the presence of domains in the membrane. In particular, sphingolipids and cholesterol were found to be important for membrane fluidic properties and domain formation [174]. The cholesterol is a waxy steroid metabolite, that helps to achieve stability and a proper permeability of the membrane. The mechanical properties of the membrane and even the lipid composition of growing cells are found to be highly sensitive to the temperature [75]. In general, lipids are known to be amphiphilic small molecules. The amphiphilic character of most of these molecules allows them to form structures, such as micelles, vesicles, liposomes or bilayer membranes. The phospholipid class, containing phosphatidylcholine (PC), sphingomyelin (SM), phosphatidylinositol (PI) and phosphatidylinositolphosphates (InsP), phosphatidylethanolamine (PE), phosphatidylserine (PS), phosphatidylglycerol (PG) and phosphatidic acid (PA), is the most important class of lipid molecules [99].

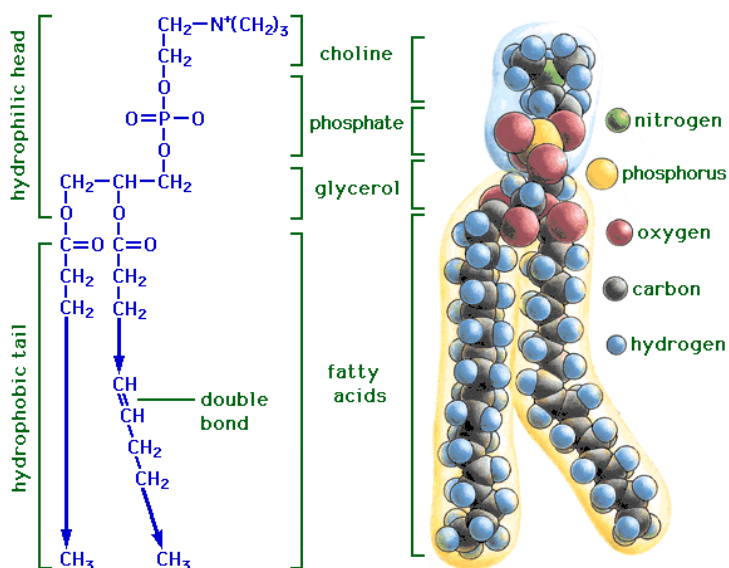


Figure 3.2: Scheme of the phospholipid structure.[138]

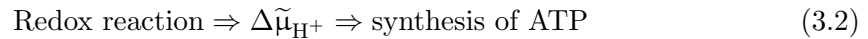
In general, the structure of a phospholipid consists of a glycerol phosphate backbone, which is covalently bound to two fatty acyl tails and a polar head group (see figure 3.2). Fatty acid chains with no double bonded carbon atoms are fully saturated with hydrogen atoms, thus known as saturated fatty acids. Unsaturated lipids, however, contain at least one double bonded carbon pair. Natural tissue consists of a varying proportion of both types. Specific lipids can have functional properties, that are important for the viability of proteins. Particularly cardiolipin (CL), a kind of diphosphatidylglycerol lipid, seems to be actively involved in maintaining mitochondrial functionality and membrane integrity. It is found almost exclusively in the inner mitochondrial membrane [166]. CL is, for example, specifically positioned at the entrance of proton uptake pathways of the  $bc_1$  complex. It is assumed that cardiolipin ensures structural integrity of the proton-conducting protein environment and it is considered to be involved directly in the proton uptake [74]. CL has been reported to act as a proton trap in membranes that conduct oxidative phosphorylation [27]. Furthermore, a reduced ET activity which was found in tumor cells has been assigned to CL abnormalities, supporting the Warburg theory of cancer [166].

### 3.2 Respiratory Chain and Phosphorilation

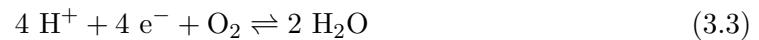
Proteins of the respiratory chain are present in the cell membrane of prokaryotes as well as in the inner membrane of eukaryotic mitochondria (see figure 3.3). The mitochondria act as generators of energy in eukaryotic cells. Nutrients are converted into chemical energy. This process is known as cell metabolism. A remarkably high quantity of mitochondria can be found in cells with highly active metabolism, such as muscle, nerve and sensory cells. Mitochondria of these cells are notably rich in the amount of respiratory enzymes. For instance, 50 % of mitochondrial bovine heart enzymes account for respiratory chain complexes [60]. Since organisms had to optimize metabolic reactions upon evolution, cell respiration emerged to a highly efficient and chemically sophisticated mechanism to synthesize ATP (see equation 3.2) [196].



Figure 3.3: Cristae-type mitochondrion and synapse (cortex cerebri, rat), kindly provided by Dr. med. H. Jastrow.



The sequence described by equation 3.2 is also known as *"the central dogma of bioenergetics"* analogous to the universal sequence of biological information transfer [196]. It is the last step in the conversion of glucose. Thereby  $\text{O}_2$  acts as a universal electron acceptor according to:



Since  $\text{O}_2$  exists in a triplet ground state, it is chemically quite inert, yet thermodynamically it is highly oxidizing. For this reason, molecular oxygen is a highly capable electron acceptor which can be transported inertly by hemoglobin or myoglobin. At the same time, it can be reduced by the activation of the bimetallic  $\text{Fe}^{2+}/\text{Cu}^{1+}$  active site of enzymes [196]. Five enzymes coordinate electron transfer and proton translocation across the membrane:

- **complex I:** NADH : ubiquinone oxidoreductase or NADH dehydrogenase
- **complex II:** succinate : ubiquinone oxidoreductase or succinate dehydrogenase
- **complex III :** coenzyme Q : cytochrome c oxidoreductase or cytochrome  $\text{bc}_1$  complex
- **complex IV:** cytochrome c : oxygen oxidoreduktase or cytochrome c oxidase
- **complex V:**  $\text{F}_0\text{F}_1$  ATPase or  $\text{H}^+$ /ATP synthase

A specific ratio of the respiratory complexes has been observed. One single complex I is followed by approximately three complexes of the type III and seven complexes of the type IV [60]. Electron transfer through the respiratory chain is driven by the reduction of oxygen by NADH and succinate at the entry points and the reduction of  $\text{O}_2$  in complex IV (see figure 3.4). The free energy gained from electron transport is converted into  $\Delta\tilde{\mu}_{\text{H}^+}$ .



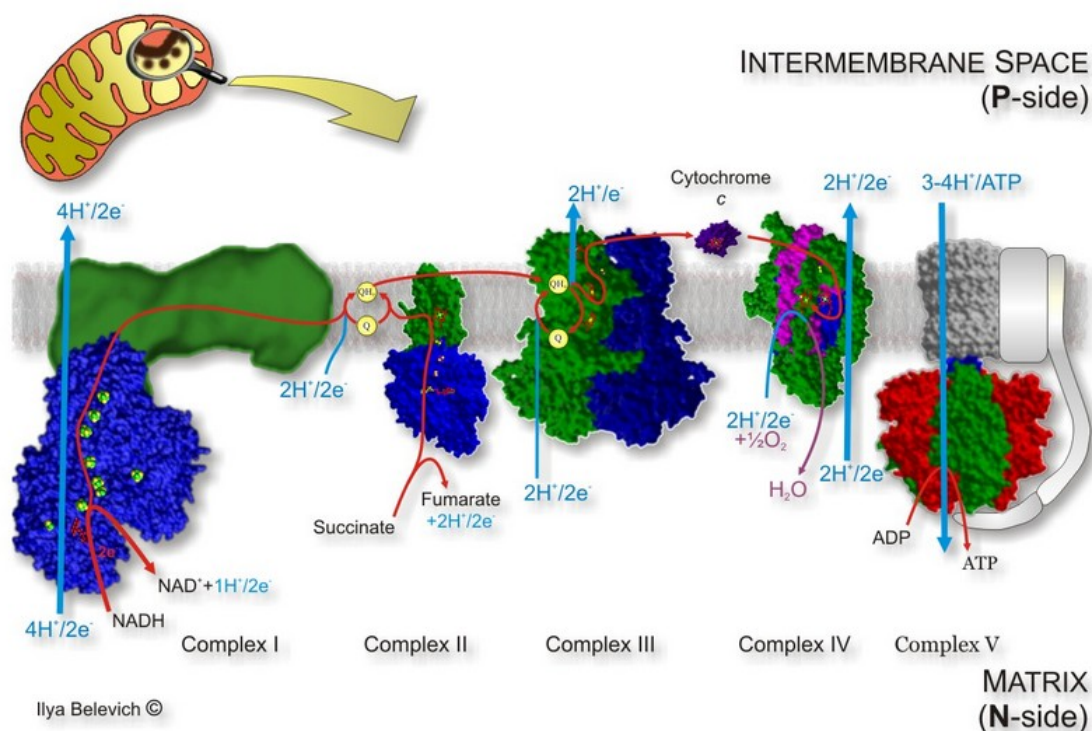
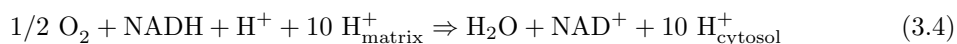


Figure 3.4: Respiratory chain of mitochondria.[72]

Finally the ATP synthase phosphorylates ADP to ATP on expense of  $\Delta\tilde{\mu}_{\text{H}^+}$ . These processes are commonly known as the oxidative phosphorylation. The final product of glucose metabolism is ATP, which serves as a ubiquitous energy supplier. It can be stored or delivered to different organelles in the cell, if required by a broad variety of biochemical reactions. NADH/H<sup>+</sup> and succinate originate from the metabolic reactions of the citric acid cycle. Complexes I-IV catalyze the reduction of oxygen stepwise. The redox cofactors which are involved in maintaining the electron transfer include flavins, iron-sulfur centers, quinones, copper centers and heme groups [196]. The electrons pass at least ten intermediate redox couples [152] (see figure 3.5). Soluble transporter molecules, such as cytochrome c and coenzyme Q, shuttle electrons between the enzymes. Cytochrome c, a water soluble protein, transports electrons from complex III to complex IV and coenzyme Q<sub>10</sub>, a lipophilic molecule, supplies complex III with protons and electrons. The overall reaction catalyzed by complexes I-IV is described by



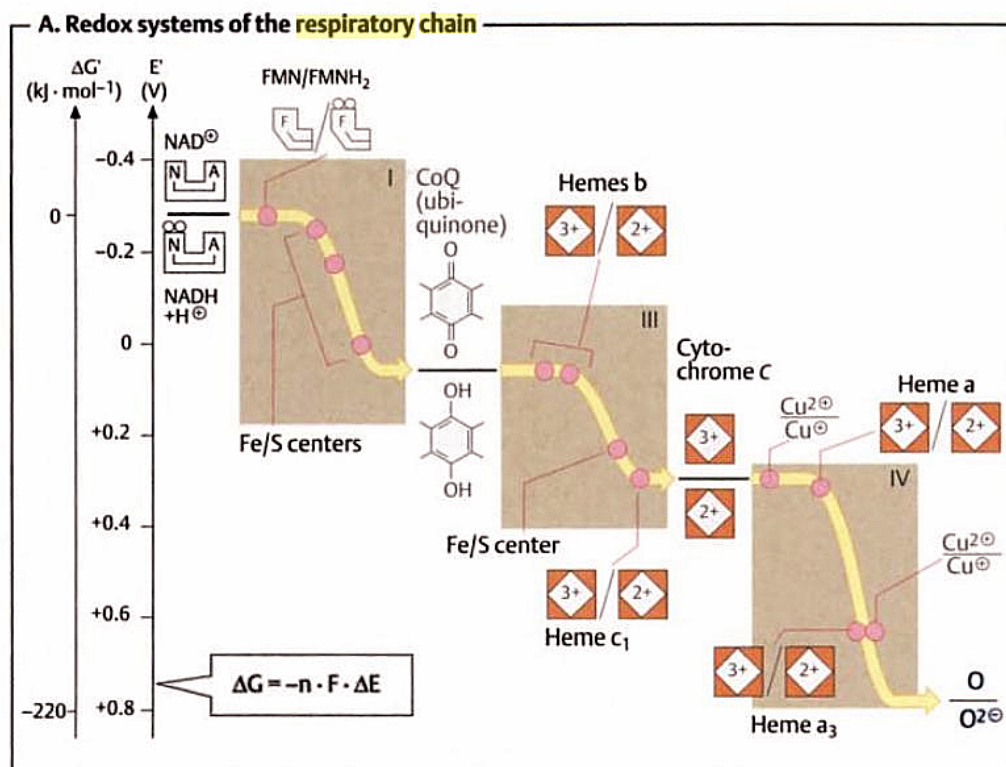


Figure 3.5: Scheme of the potential-driven redox cascade in the respiratory chain.[152]

### 3.3 Structure and Function

Since CcO plays a crucial role in metabolism, its structure and function have been the subject of extensive studies. Characterization of CcO from yeast opened the way for investigations of the enzyme [16]. Heme-copper oxidases and in particular CcO were investigated by functional analysis, advanced spectroscopy, molecular genetics, mutational analysis and crystallographic structure analysis. The latter method was recently getting more important for the study of the mechanism of electron and proton transfer at the atomic level. Some of the methods, such as DNA sequencing [50][51], EPR- [140][70], NMR- [157][165], vibrational- [124][184][182][23] and UV/Vis spectroscopy [124], as well as electron- [128][43] and X-ray crystallography [206][207][177][208][167], have been applied to investigate the structure of both mitochondrial and bacterial CcO. Furthermore, time-resolved optical as well as Resonance Raman (RR) spectroscopy could give an insight into catalytic activity.[8][139] In 1961, successful crystallization of CcO was reported for the first time [204], however the quality for high resolution structure analysis was not reached until the recent years. Nowadays, various 3D structures are available on the Protein Data Bank. The Protein Data Bank (PDB) is a commonly used platform that provides 3D physical structures of proteins and nucleic acids generated by crystallization and X-ray diffraction analysis or NMR spectroscopy. The successful elucidation of 3D structures for either the mitochondrial and several bacterial oxidases with a resolution down to about 1.8 Å helped to study structural and functional properties of the enzyme. Particularly CcO structures from bovine heart [137], *Rhodobacter sphaeroides* [37] and



*Paracoccus denitrificans* [115] are represented in the PDB. The enzyme occurs as multi-subunit complex and consists at least of the three largest basic subunits (SU), the SU I, II and III, being relatively conserved throughout evolution [164]. Prokaryotes, in general, do not have additional SUs, whereas the mammalian CcO contains up to ten additional SUs. Eukaryotic CcO is encoded in two genomes. The largest SUs (I, II and III) are coded by mtDNA and synthesized in the mitochondria, while the others are coded in the nucleus and produced in the cytoplasm [16][196]. On the basis of phylogenetic comparisons of the known archaeal enzymes with their bacterial homologues, it was suggested that the enzyme existed in a common ancestor even before the occurrence of atmospheric  $O_2$  which implies the existence of an alternative electron acceptor at that time [65][164]. Due to the same evolutionary origin, both the mitochondrial and bacterial heme-copper catalytic cores (SUs I and II) are similar in their structure and the electron and proton translocation pathways are identical [178][78]. For this reason, some bacterial CcO types may serve as simple model systems that can be studied to understand at least the basic enzyme functions [101]. Some heme-copper superfamilies are exclusively present in thermophilic archea and the properties of their proton channels have therefore changed during evolution, due to adaption to specific environments [49]. These enzymes will not be appropriate alternatives for the investigation of mitochondrial heme-copper oxidoreductase. Furthermore, some bacterial heme-copper enzymes do not only contain hemes of the type a like the  $aa_3$ -type CcO in mitochondria. These enzymes appear as ab-type or ao-type oxidases [52]. The  $aa_3$ -type CcO originating from *Rhodobacter sphaeroides* and *Paracoccus denitrificans* serves as an adequate model system, thus in our studies these particular enzymes were used.

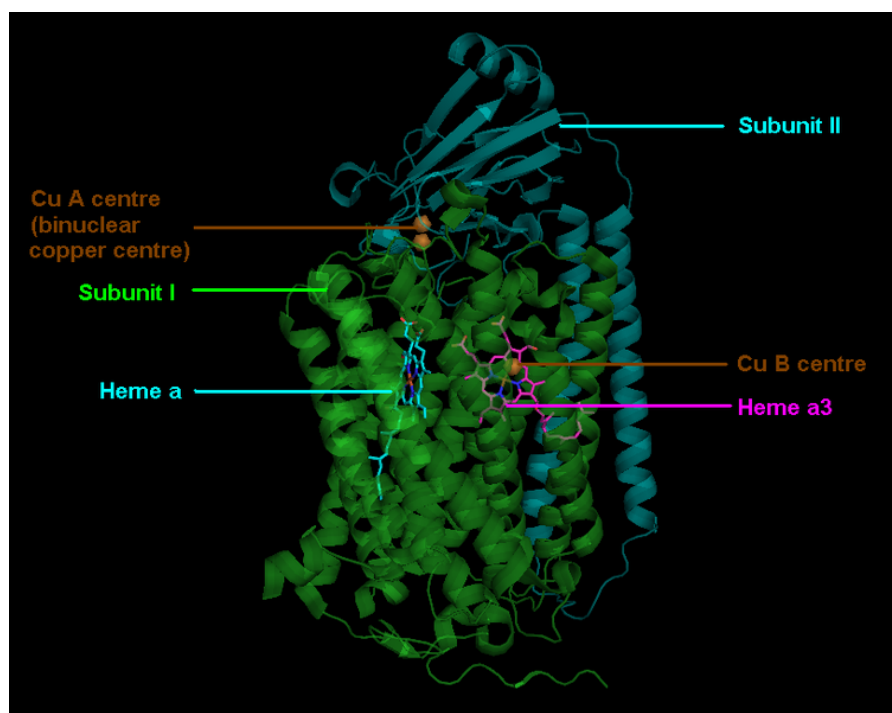


Figure 3.6: 3-Dimensional illustration of SU I and II of cytochrome c oxidase viewed parallel to the membrane. Additional SUs are excluded. [203]

CcO has a trapezoidal form and contains 22 membrane-spanning, mostly helical segments and their connections. The width of the cytoplasmic surface (bottom) is about 90 Å and the periplasmic surface (top) is about 75 Å. The height of the trapezoid is about 55 Å and has a maximum height of 95 Å at the C-terminus of the SU II [116]. Being part of the subunit II (SU II), the binuclear  $\text{Cu}_A$  center, accepts electrons from the reduced cytochrome c. Heme a, a low-spin heme, receives the electrons from  $\text{Cu}_A$  subsequently and transfers them to the catalytic center consisting of a high-spin heme  $a_3$ , and a copper atom,  $\text{Cu}_B$ . There, molecular oxygen is reduced to water. In general, all protonmotive heme-copper oxidases contain a heme-copper center in which the reductive chemistry of oxygen takes place, whereas  $\text{Cu}_A$  is exclusively present in CcO. The binuclear copper center exists in a mixed valence state ( $\text{Cu}^{1+}/\text{Cu}^{2+}$ ) and the average distance between both ions is 4.5 – 5.2 Å [101].  $\text{Cu}_A$  appears to be liganded by two histidin and two cystein residues [18]. Heme a, heme  $a_3$  and  $\text{Cu}_B$  are liganded via amino acid side chains to the SU I, the central part of the complex. Two histidines serve as axial ligands to bind heme a [24], whereas only one histidine residue binds heme  $a_3$  to the SU I [19]. The  $\text{Cu}_B$  is chelated by three histidin redidues in the reduced as well as in the oxidized form [17]. It is likely that heme  $a_3$  and  $\text{Cu}_B$  are bridged by a shared ligand that could be a sulfur-containing residue [2], a  $\mu$  peroxy group [106] or a chloride ion [17][16]. The distances between  $\text{Cu}_A$  and the iron center of heme a and heme  $a_3$  are 19.5 Å and 22.1 Å, respectively, for CcO from *Paracoccus denitrificans* [116]. Heme a and heme  $a_3$  are 12 – 16 Å apart [44][80] and heme  $a_3$  and  $\text{Cu}_B$  are 3 – 4 Å apart [17][2]. The substrate protons that are consumed in the formation of water have to be transported over a distance of about 30 Å to the active site of the protein, whereas the pumped protons have to be carried over some 55 Å corresponding to the longitudinal axix [48] (see figure 3.6). In all mitochondriandrial and most bacterial heme-copper complexes at least the SU III is present in addition to SU I and II. The function of SU III and further SUs is unknown, they seem neither be involved in the binding of redox-active prosthetic groups nor contribute to the proton pumping [116]. However, it has been proposed that the SU III acts as an oxygen reservoir [198]. It has also been suggested that the additional SUs have a stabilizing and regulatory function [101]. Since the SUs I and II are essential for proton pumping, they are also known as core or catalytic SUs (see figure 3.6). CcO consisting only of SU I and II has been isolated [162] and was still active in proton pumping [103]. In the exceptional case of the *Paracoccus denitrificans*, CcO only contains SU I and II and exhibits a molecular weight of 79 – 84 kDa. In the solubilized form it occurs as a monomer [155]. Structure analysis could identify two proton transfer pathways, one for protons consumed in water formation and one for the mechanism of proton pumping [116]. Furthermore, the electron-tunneling pathways for internal transfer have been calculated [107][143]. These aspects will be discussed in detail in section 3.5. Specific conformational changes in the protein structure, particularly near the active site, are expected to facilitate the turnover process. They have been observed in conjunction with redox transitions[38][109][32]. This process occurs as well-defined sequential changes in amino acid side chain orientations, protonation states and hydrogen bonds [46]. The opening of proton pathways and a concomitant flux of water molecules towards the active site is triggered by conformational changes. They are reversible upon reoxidation. A water molecule has been observed in the hydrophobic region. It is expected to support the connection between the proton channel and the active site [38]. It has been reported that ATP triggers a conformational change on the water-exposed surface of cytochrome c oxidase, thus influencing the kinetics of

electron transfer from cytochrome c to mitochondrial oxidase [125].

### 3.4 Catalytic Cycle

Different mechanisms describing the catalytic cycle of CcO have been the issue of controversy over the last two decades. In the late 1980s, the catalytic reaction was widely accepted, but a detailed description was still missing. However, a simple model already existed at that time (see figure 3.7).

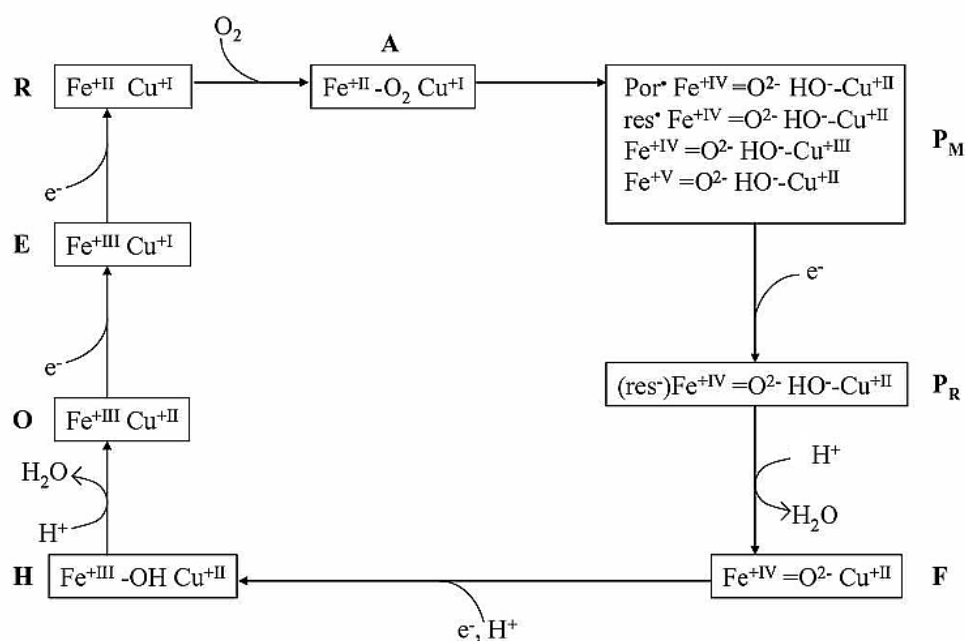


Figure 3.7: Catalytic cycle of Cytochrome c Oxidase. Only heme  $a_3$  (Fe) and  $\text{Cu}_B$  of the catalytic center are shown and proton pumping is omitted.[15]

The intermediate O corresponds to the fully oxidized state of the enzyme and is the initial state. The state E is formed by taking up one electron [153]. The uptake of a second electron leads to state R in which the protein is reduced twice.  $\text{Fe}^{2+}$  will bind molecular oxygen forming the intermediate A [100]. The transfer of four electrons between iron and copper to  $\text{O}_2$  causes the transition from A to the intermediate P<sub>M</sub>. P<sub>M</sub> is named after the peroxide or hydroperoxide which are supposed to be coordinated to  $\text{Fe}^{3+}$  and Cu of the active center [190]. Recently, it has been assumed that P<sub>M</sub> is characterized by an oxoferryl structure of heme  $a_3$  iron ( $\text{Fe}^{4+} = \text{O}^{2-}$ ) and a hydroxyde ion bound to  $\text{Cu}_B$  ( $\text{Cu}_B^{2+} - \text{OH}$ ). Three of the four electrons can be provided by the metal centers when  $\text{Fe}^{2+}$  is oxidized to  $\text{Fe}^{4+}$  and  $\text{Cu}^{1+}$  is oxidized to  $\text{Cu}^{2+}$ . The origin of the fourth electron is not definitely clear. Four different possibilities have been suggested (see figure 3.7). The first assumes the oxidation of the porphyrine ring, the second the oxidation of an amino acid residue, the third an oxidation to  $\text{Cu}^{3+}$  and the fourth an oxidation to  $\text{Fe}^{5+}$ . Considering the first two possibilities, the reduction of the porphyrine ring or the amino acid residue by uptake of an additional electron leads to the transition to the intermediate P<sub>R</sub>. The uptake of a proton and subsequent release of  $\text{H}_2\text{O}$  leads to oxoferryl state (F) and uptake

### 3.4 Catalytic Cycle

of a final electron together with a proton generates the intermediate H, named after the iron hydroxy species. Uptake of a proton and subsequent release of water regenerates state O.

In 1989, Mårten Wikström contributed an important suggestion how electron transfers in CcO are coupled to proton-pumping [191]. By means of potentiostatic titrations of mitochondria in presence of a proton motive force, he could demonstrate that the oxidative part (the P→F and the F→O transition) of the cycle is reversible. Therefrom he concluded that the protons must be pumped in this part of the catalytic cycle. Furthermore, he deduced that at each of these transitions two protons are pumped across

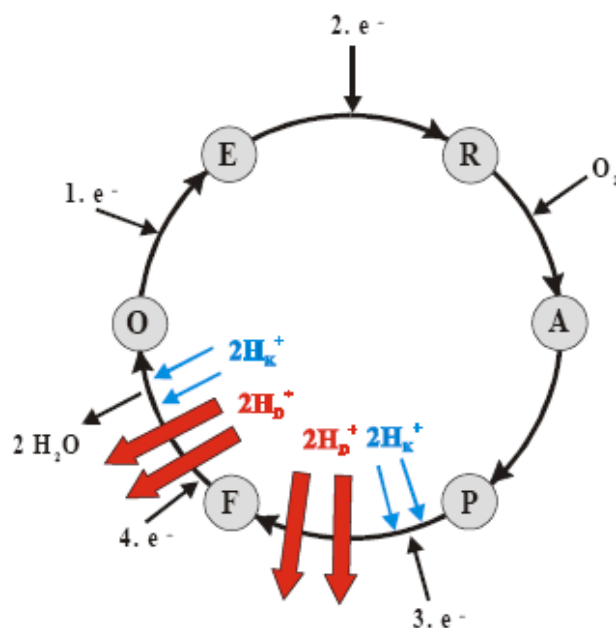


Figure 3.8: Simplified scheme of the catalytic cycle performed by CcO. This was suggested by Wikström in 1989.[158]

the membrane. At the same time one electron is expected to be transported to the catalytic center and two substrate protons are taken up for the synthesis of water. Explaining the mechanism of coupled proton translocation for the first time, however, this theory is constrained by the following assumptions: The intermediates are in thermodynamic equilibrium with each other. The membrane is impermeable to protons and the proton motive force can be calculated from concentrations of ADP and ATP. Additionally, the pH difference across the membrane must be neglected and the catalytic center must be located in the dielectric center [158].

Michel encountered several discrepancies when analysing the data and trying to understand their coherence with Wikström's classical model. The suppositional assumptions of the classical model didn't seem to reflect the enzyme's physiology. Ferguson and Soragato, for example, doubted that the intermediates would be in equilibrium even before Wikström published the classical model [169]. Furthermore, it has been shown that two protons are taken up already in the reductive part of the cycle [154]. To this end, Michel modified Wikström's cycle. His findings which are based on spectroscopic and mutagenesis data were published in 1998 (see figure 3.9) [114]. He proposed that only one proton

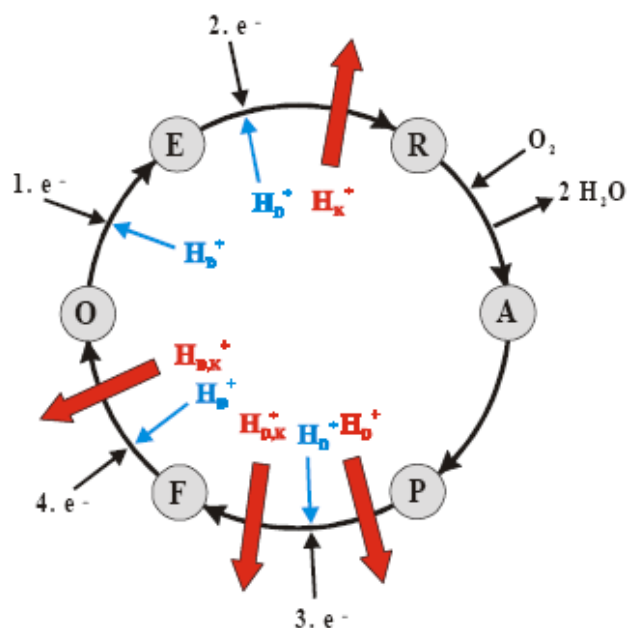


Figure 3.9: Modified scheme of the catalytic cycle performed by CcO. This was suggested by Michel in 1998.[158]

would be pumped during the  $F \rightarrow O$  transition whereas the second would be pumped during the  $E \rightarrow R$  transition. The principle of electroneutrality [154] was taken strictly into account. In Michel's model, every step of reduction of heme  $a_3$  is coupled to the proton uptake via D-channel. The protons are expected to be stored at the propionates of the heme. The electrostatic repulsion then initiates the "pumping mechanism" by taking up substrate protons [158].

Motivated by Michel's suggestions, Wikström and Verkhovskiy reconsidered their previous model. Proton translocation performed by bovine CcO was therefore investigated for the reductive as well as the oxidative part of the catalytic cycle, monitoring the pH change in the proteoliposomes in suspension [197]. Based on the results of this study, Wikström replied with a new model [192], in which he changed his previous suggestion that the four protons are pumped during the oxidative part of the cycle. He proposed that two protons are pumped in the oxidative part, whereas the other two protons are pumped in the reductive part (see figure 3.10). The latter protons are expected to be pumped exclusively if the oxidative cycle was performed shortly before. This aspect indicates the existence of an activated state which can be reached by CcO. The energy which is taken up during the oxidation is assumed to be stored and provided for the pumping of protons in the reductive part of the cycle. Wikström called this state the  $H\sim$  state. This theory is based on a histidin cycle. A His-ligand, probably the His-326, might play a key role in this context. Furthermore it is assumed that three different conformational states exist for this particular ligand.

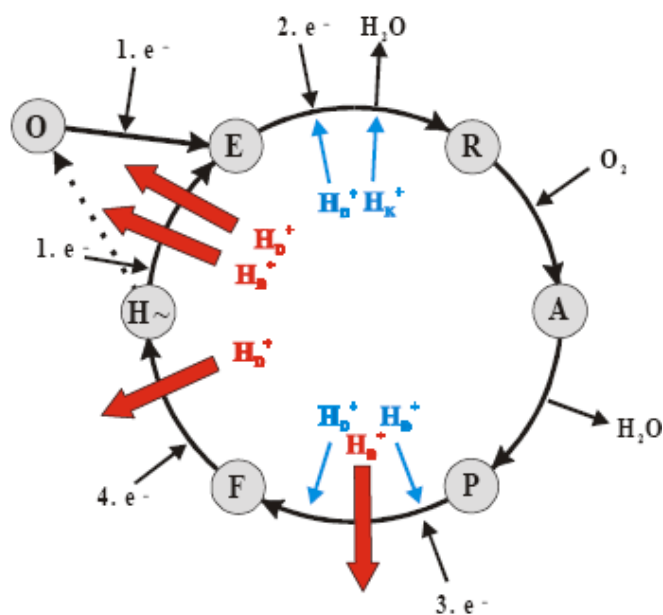


Figure 3.10: Latest model for the catalytic cycle performed by CcO. This was suggested by Wikström in 2000.[158]

### 3.5 Electron and Proton Pathways

Studies investigating electron and proton transfer pathways help to understand the mechanisms and function of CcO. Electrons and protons prefer specific translocation pathways. These pathways depend on the structure and the charge density properties.

Different electron pathways suggested for CcO have been discussed [116][107][146][172][143]. The reduction of CcO is initiated by Cyt c. In bacteria, Cyt c binds covalently to the C-terminal of the SU II [205]. A tight binding between Cyt c and CcO is present in *Paracoccus denitrificans*. This indicates a strong electrostatic force and hydrophobicity [181][26]. In contrast eucaryots contain a rather weak binding between Cyt c and CcO [111]. Purified mammalian CcO binds one molecule of substrate Cyt c at a high affinity site [111][112][14]. A ring of six or seven Lys residues of Cyt c are involved by binding to the corresponding carboxyl groups of CcO [118]. The binding of a second Cyt c at a lower affinity site has been reported, however, the function remains unclear [111][112][118][16]. Due to a close binding of Cyt c to Cu<sub>A</sub>-side, Cu<sub>A</sub> acts as the initial electron acceptor. Dominant pathway tubes and effective electronic couplings between the donors and the acceptors have been calculated [142] using the Green's function technique with an extended Hückel-like electronic Hamiltonian [143]. Simulations of the molecular dynamics for CcO in a native environment take into account the thermal motion of the protein atoms. This also influences the electron pathway. The effective coupling depends on the electron tunneling energy. Conventional theories, such as the Marcus theory, predicted that the nuclear dynamics influences the Franck-Condon factor, whereas recent studies of biological ET reactions have shown that nuclear dynamics also have an influence on the effective electronic coupling [142]. It has been shown that the ET rates which are only based on crystallographic data are much smaller compared with effective couplings. The reason for this is the thermal motion which induces a shortening of some through-

space jump distances [143][142]. ET from  $\text{Cu}_A$  to heme a is mediated by its ligands. This sort of coupling is basically weaker than the couplings provided by covalent bonds [143]. Several possible pathways from  $\text{Cu}_A$  to heme a exist (see Figure 3.11). Two pathways starting from  $\text{His}^{\text{B}204}$  and  $\text{Cys}^{\text{B}196}$  have been proposed [57]. Two other relevant pathways starting from  $\text{Cys}^{\text{B}200}$  and  $\text{Glu}^{\text{B}198}$  have been identified additionally [143]. However, the

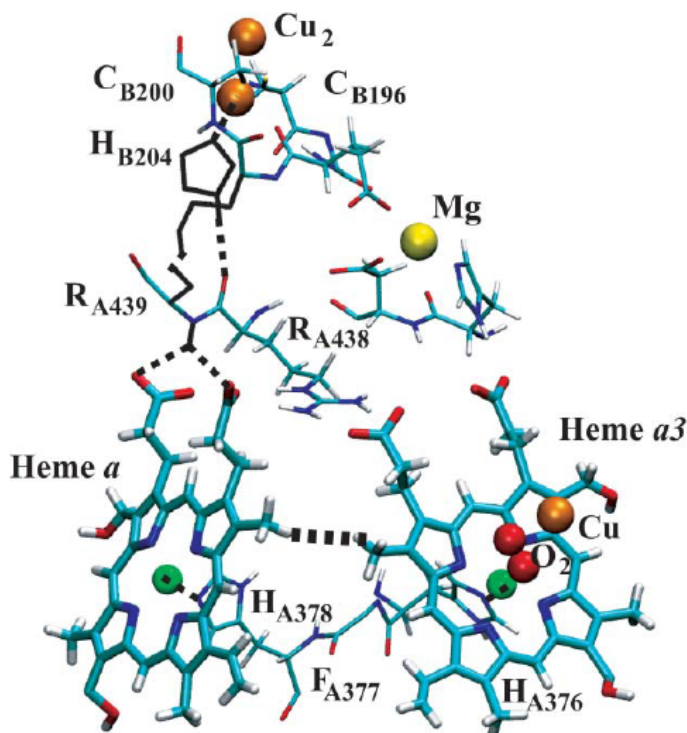


Figure 3.11: Possible ET pathways in CcO. Solid black lines indicate the pathways mediated by covalent bonds, the dashed black lines indicate the pathways mediated by hydrogen bonds or through space jumps. Thin and thick colored lines indicate bonds of residues and the heme groups, respectively. The metal atoms are shown as van-der-Waals spheres colored by atom name. [143]

pathways starting at  $\text{His}^{\text{B}204}$  and  $\text{Glu}^{\text{B}198}$  dominate the ET reactions, due to shortening of the distances in terms of the effective coupling. The shortening of the hydrogen bond between  $\text{His}^{\text{B}204}$  and  $\text{Arg}^{\text{A}438}$  is for example  $\sim 0.5\text{\AA}$ . This is the reason for an increase of the maximum ET rate by almost an order of magnitude [143]. Contrary to this reaction, the distance of the through-space jump between  $\text{Ile}^{\text{B}199}$  and  $\text{Arg}^{\text{A}438}$  increases in the equilibrium conformation by more than  $2\text{\AA}$  which leads to a substantial decrease of the ET rate through the pathway starting at  $\text{Glu}^{\text{B}198}$ . For this reason, the other two pathways do not contribute essentially [143].

For the transfer of electrons from heme a to heme a<sub>3</sub> different possible pathways have been proposed. Multiple possible pathways are mediated by groups surrounding the both hemes. Two of them have been suggested to include the fully covalent pathway. The covalent pathway is mediated by  $\text{His}^{\text{A}378}$ ,  $\text{Phe}^{\text{A}377}$  and  $\text{His}^{\text{A}376}$  [107]. Furthermore there exists a direct pathway that includes a through-space jump between the  $\delta$  propionates of the two hemes [171]. Two more relevant pathways were identified by Tan's group. One

of them is mediated by Arg<sup>A438</sup> including two hydrogen bonds and another one is mediated by His<sup>A378</sup>, Ala<sup>A375</sup> and His<sup>A376</sup> including one hydrogen bond [143]. However, the covalent and the direct pathway in the crystallographic structure dominate the effective coupling. The thermal motion effects a shortening in the distance of the through-space jump to  $\sim 2\text{\AA}$ . An increase of the corresponding ET rate by an order of magnitude results from this effect. Hence, the direct pathway is the most dominant one [143]. Recent suggestions that the ET between heme a and heme a<sub>3</sub> is facilitated by water molecules [173] is rather unlikely due to the strong hydrophobic environment of the direct pathway. Furthermore, the distance between the two hemes is too small for the water molecules [143].

Proton pathways through the inner structure of CcO are required for three specific purposes. One pathway is required for the transport of the four substrate protons from the matrix to the active site. Another two pathways are needed for the uptake of four pumped protons and for their release into the cytosol (see equation 3.1). Two different proton transfer pathways (named D- and K-pathway) channeling the substrate protons from the N-side to the binuclear heme a<sub>3</sub>-Cu<sub>B</sub> site have been identified by means of site-directed mutagenesis [1]. The presence of these two pathways was confirmed and specified by crystal structure analysis.

The D-pathway in subunit I starts at a conserved aspartic acid near the N-side. It is connected by a series of hydrophilic amino acids and some bound water molecules which are some 10 $\text{\AA}$  apart from the O<sub>2</sub> reduction site (see Figure 3.12). The K-pathway is mainly part of SU I and starts at a conserved lysine residue. It is connected via a water molecule and a serine residue of SU I, or via a conserved glutamic acid residue of SU II. This pathway passes a threonine and/or serine residue and ends up in a tyrosine residue close to the O<sub>2</sub> reduction site [195]. The exit pathway for pumped protons still remains unsolved so far. Based on experimental data, it has been suggested that this pathway starts from a domain including the D-propionate of heme a<sub>3</sub> and its ion pair, a conserved arginine [36][195]. Furthermore, the region around the protein at the P-side is rich in water molecules, hence it is complicated to identify a unique exit proton transfer pathway in the structure of the protein [195].





Figure 3.12: Scheme of SU I and II of CcO from *Paracoccus denitrificans*. The electron pathway (green) and both proton transfer pathways are marked (blue). The D-pathway starts at Asp<sup>124</sup> and leads via several polar residues to Glu<sup>278</sup>. The K-pathway passes Ser<sup>291</sup>, Lys<sup>354</sup>, Thr<sup>351</sup>, Tyr<sup>281</sup>. [158]

---

## 4 Artificial Membrane Systems

Membrane proteins are exclusively present in organelle membranes, thus being hardly accessible in the experiment. For this reason, they have to be isolated from their natural environment. The maintenance of their actual function under artificial conditions requires optimal bio-mimicking conditions.

Previously, membrane proteins were commonly stabilized in detergent solutions rather than lipid bilayers [28][184][141]. Obviously, the influence of the water- and the lipid-protein interface on the functional properties of the enzymes has been neglected. Realizing this problem, various biomimetic membrane architectures have recently been developed. Therefore, membrane-bound proteins have been reintegrated into phospholipid bilayers, thus performing their original function in a nature-mimicking environment.

To this end, functional proteoliposomes have commonly been used as artificial lipid membranes. However, proteoliposomes enclose a small volume which is hardly accessible to measurements of differences across the membrane. An alternative system that avoids inaccessible volumes is the Black Lipid Membrane (BLM). It has proven to be well suitable to electrical measurements, which is particularly important when investigating voltage gated ion channels. Yet, the BLM is inauspicious in conjunction with big membrane proteins, due to little mechanical stability [201]. Alternatively, the model membrane systems have been immobilized directly onto biocompatible metal supports that can be used as electrodes. This system is known as solid supported bilayer lipid membrane (sBLM). With this system, denaturation of the proteins caused by the interaction with the metal surface has to be considered.

Some years ago, a new concept of solid-supported tethered bilayer lipid membranes (tBLM) for the reconstitution of membrane proteins was introduced by our group [88]. This is the so-called protein-tethered bilayer lipid membrane (ptBLM). The solid support which is an ultraflat gold surface (template stripped gold, TSG) has then been functionalized with a mixture of NTA-Ni<sup>2+</sup> (Nitrilotriacetic-Nickel) molecules and DTP (Dithiopropionate). It is commonly known that histidine-tags (His-tags) are highly affine to Ni<sup>2+</sup>-complexes [161]. Thus a his-tag has been genetically engineered to the C-terminus of SU II of CcO. Ni<sup>2+</sup>-ions are bound to the NTA-residue including two water molecules to form an octahedral complex. In the course of protein binding, two His-residues replace the water molecules generating a stable chelate-complex (see Figure 4.1). Exemplary for other membrane proteins, the detergent-solubilized CcO from *Rhodobacter sphaeroides* is in-situ tethered to the metal chelating surface in a strict orientation. Subsequently, the solution containing excessive proteins is flushed away and replaced by a detergent-solubilized lipid micelle solution. The in-situ dialysis is then initiated by the addition of biobeads. After  $\sim 48$  h, the reconstitution of the membrane was complete. In this configuration, the protein is surrounded by a versatile lipid bilayer phase and at the same time it is attached to a metal surface. The protein itself defines the volume of the submembraneous space. The distance between the protein and the surface plays an important role in order to preserve the original protein structure from denaturation. Furthermore, a volume serving as ion reservoir is achieved. One criterion for the artificial ptBLM is to achieve the electrical properties that are found for phospholipid bilayer membranes. Typically, the capacitance and resistance of a pure lipid bilayer are  $\sim 0.5 \mu\text{F} \cdot \text{cm}^{-2}$  and  $\geq 1 \text{ M}\Omega \cdot \text{cm}^2$ , respectively [42][89]. Resistances in the same order of magnitude can be found in ptBLMs. However, dependent on the protein concentration, the capacitance and

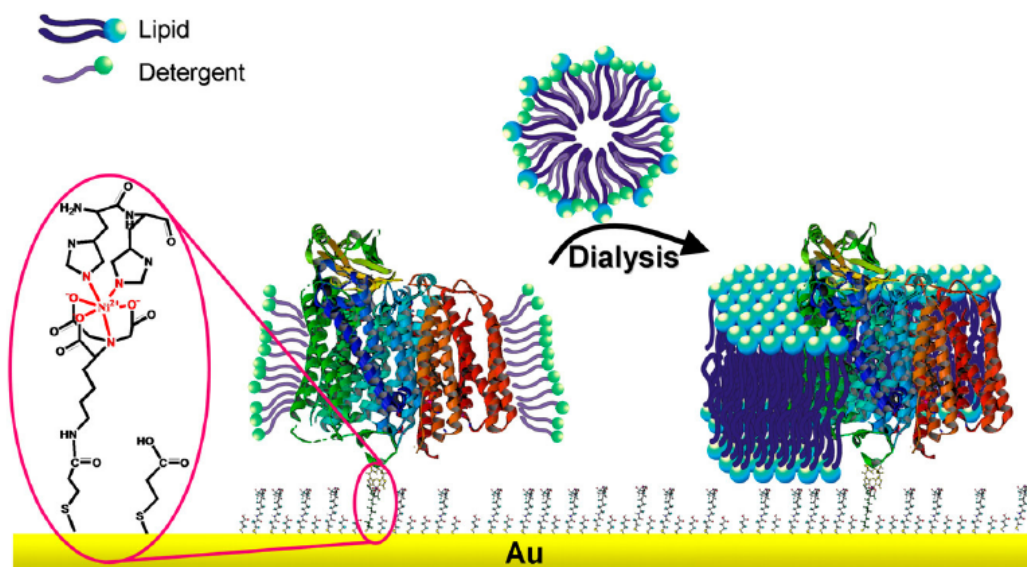


Figure 4.1: Scheme of the in-situ dialysis of CcO. In the first preparation step (left) the detergent solubilized CcO is attached via His-tag to the functionalized surface in a strict orientation. The ultraflat gold surface (TSG) has been functionalized with NTA-Ni<sup>2+</sup> ex-situ, before. With the help of biobeads, the in-situ dialysis takes place and the lipid micelles made from detergent-solubilized lipids assemble into a bilayer phase around the proteins during ~ 48 h (right).[134]

resistance differ. The properties of the system can be characterized by surface plasmon resonance (SPR), electrochemical impedance spectroscopy (EIS) (see subsection 6.1.3 and 6.1.1, respectively) and quartz crystal microbalance (QCM). Successful applications utilizing the ptBLMs have recently been reported [66][179]. ptBLMs allow the application of electrochemistry in combination with surface-enhanced spectroscopy which is a considerable advantage.

## 5 Methods

### 5.1 Surface Plasmon Resonance

An interface consisting of two media with different refractive indices  $n_1$  and  $n_2$  will split the incident light into a transmitted and a reflected beam (see Figure 5.1). The angles between perpendicular and incident or reflected beam are given by the equation  $\Theta_{\text{incid.}} = \Theta_{\text{refl.}}$ . For the transmitted beam, Snellius' law of refraction is valid:

$$\sin \Theta_{\text{incid.}} / \sin \Theta_{\text{transm.}} = n_2 / n_1 = \text{const.} \quad (5.1)$$

If the incident beam is transmitted from a medium with a lower refractive index  $n_1$  into a medium with a higher refractive index  $n_2$  ( $n_1 < n_2$ ), it follows  $\Theta_{\text{incid.}} < \Theta_{\text{transm.}}$ . The

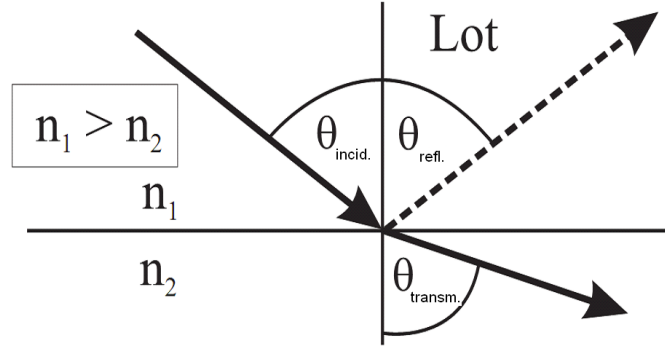


Figure 5.1: Optical path of incident, transmitted and reflected light beam at the interface of two media with different refractive indices  $n_1$  and  $n_2$ .

case of total reflection can be obtained for  $\Theta_{\text{transm.}} = 90^\circ$ . The angle of incidence can then be calculated by means of the equation 5.1 with  $\sin \Theta_{\text{incid.}} = n_2 / n_1$ . This angle is the critical angle for the total reflection  $\Theta_{\text{crit.}}$ . For  $\Theta_{\text{incid.}} > \Theta_{\text{crit.}}$ , the transmitted beam has the form of a surface wave propagating along the interface. The wave generates an evanescent field at the interface, whereby the intensity of the reflected beam can change within a specific wave length. Selectivity can be improved by the excitation of surface plasmons enhancing the evanescent field.

Surface plasmons are longitudinal charge density waves of the nearly free electron gas in a metal. The evanescent field decreases exponentially in the direction perpendicular to the direction of propagation (z-direction) (see Figure 5.2). The resonant excitation of surface plasmons with monochromatic light requires the maintenance of energy and impulse.

The relation between wave vector in propagation direction  $k_x$  and angular frequency  $\omega$  of the light results from the energy-impulse relation  $p = h/\lambda = hk/2\pi$  and the energy  $E = h\nu = h\omega/2\pi$  of the photon. The dispersion relation is given by

$$k = \omega \sqrt{\epsilon_i} / c \quad , \quad k_x = \omega \sqrt{\epsilon_i} / c \cdot \sin \Theta_{\text{incid.}} \quad (5.2)$$

where  $\epsilon_i$  is the dielectric constant of the medium  $i$  and  $c$  is the velocity of light. Due to the continuity condition of the electromagnetic field, the surface plasmons can only be excited through parallel polarized light. The following dispersion relation arises for the propagation of surface plasmons along the interface of the metal and the dielectric [151]

$$k_x = \omega/c \sqrt{\epsilon_M \epsilon_D / (\epsilon_M + \epsilon_D)} \quad (5.3)$$

where  $\epsilon_M$  is the dielectric constant of the metal and  $\epsilon_D$  is the dielectric constant of the dielectric. The components of the wave vector of the incident photons, that are taking

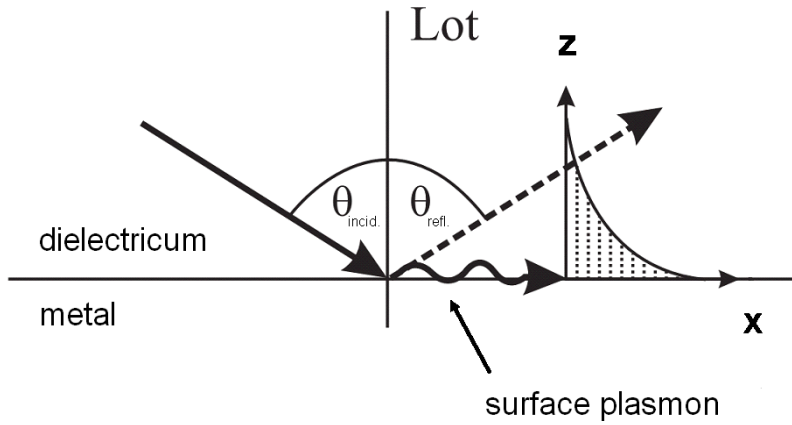


*Figure 5.2: Optical path of incident and reflected light beam at the interface of a metal and a dielectricum. The excited surface plasmon decreases exponentially within the  $z$ -direction.*

course parallel to the surface ( $k_x$ ), have to match the wave vector of the plasmons, thus achieving the impulse in the case of resonant excitation. Furthermore, the frequency  $\omega$  of the photon has to match the frequency of the plasmon. If the dielectric consists of air, the dispersion curve corresponding to the photon will not have a point of intersection with the dispersion curve of the surface plasmon (see figure 5.3). Excitation of plasmons cannot be achieved by the direct coupling of light from air into the metal surface. In this case, the impulse of the photon is not high enough to excite a plasmon. For this reason, it is necessary to increase the impulse of the incident photons at constant laser frequency  $\omega_L$ . An increase of the impulse can be achieved by the use of dielectrics with higher refractive indices, thus having higher dielectric constants  $\epsilon_i$ . A common method in this context is the coupling by prisms. Two different configurations can be utilized, the Kretschmann- and the Otto-configuration (see Figure 5.4). In the configuration according to Kretschmann, the laser light couples into the metal, where the thickness of the metal layer is very low and the incident photons can easily reach the interface of dielectricum and metal exciting a surface plasmon there [93]. In the Otto-configuration an evanescent field existing at the interface of the prism and the air will excite a surface plasmon in the

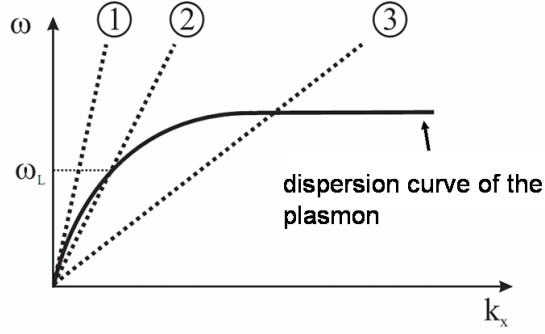


Figure 5.3: Dispersion relation of the surface plasmon and of the photon in air (1). There is no point of intersection for both curves. An arbitrary increase of the refractive index of the medium produces a point of intersection with only the both curves, but not the laser frequency (3). The choice of a distinct angle of incidence  $\Theta_{incid.}$  will evoke a common point of intersection (2). This condition is required for the resonant excitation of the surface plasmon.[96]

metal surface. The prism and the metal are separated by a small air gap [145]. However, the control over the thickness of the air gap is hardly possible .

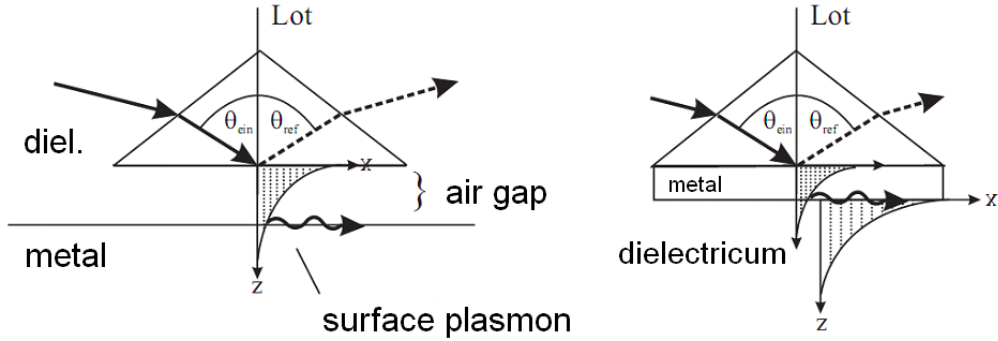


Figure 5.4: Schematic coupling of prisms for excitation of surface plasmons in two possible configurations: Otto- (left) and Kretschmann-configuration (right).[159]

### Principle of measurement

The reflectivity  $R$ , which is the ratio of the intensities of the reflected and the incident beam,  $R = I_{refl}/I_{incid.}$ , is plotted against the incident angle  $\Theta_{incid}$  in order to characterize the dielectric layers (see Figure 5.5, left scheme). The critical angle  $\Theta_c$  is followed by a plateau according to the total reflection. Further increasing the angle causes a decrease in reflectivity. Resonance is achieved at  $\Theta_0$ , where the reflectivity has its minimum. Adsorption of thin dielectric molecule layers on the metal surface gives rise to a change in the dispersion relation, thus shifting the minimum from  $\Theta_0$  to  $\Theta_1$ . The shift of the angle results from

$$\Delta\Theta = \Theta_1 - \Theta_0 \propto (n_{molec.layer} - n_{metal})d \quad (5.4)$$

where  $d$  is the layer thickness and  $n_i$  is the corresponding refractive index. If the refrac-

tive indices of the layers are known, their thickness can be determined. Time-dependent recording of the reflectivity at a fixed angle  $\Theta^*$  provides information about the kinetics of the adsorption process (see Figure 5.5, right scheme). In this context it is important to choose an angle within the linear slope of the SPR-scan. Alternatively, the position of the reflection minimum can be traced. The main source for this section was another PhD thesis [159].

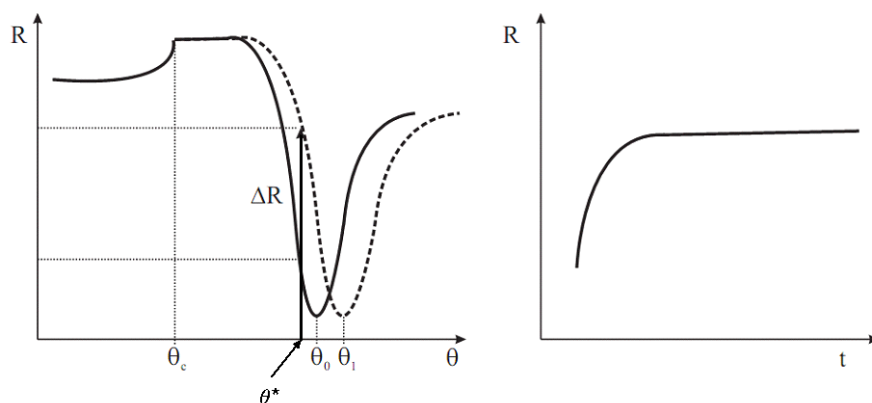


Figure 5.5: Angle scan of the reflectivity (left) before (solid line) and after (dashed line) the adsorption of a dielectric molecule layer on the surface. Kinetic trace (right), following the reflectivity at a fixed angle  $\Theta^*$  in the course of time.[159]

## 5.2 Electrochemistry

### 5.2.1 The Electrical Double Layer

The solution side of the double layer is thought to be made up of several "layers". That closest to the electrode, the inner layer contains solvent molecules and sometimes other species (ions or molecules) that are said to be specifically adsorbed (see figure 5.6). This inner layer is also called compact or Helmholtz layer. The locus of the electrical centers of the specifically adsorbed ions, with a distance  $d_i$  from the electrode, is called the inner Helmholtz plane. The total charge density resulting from specifically adsorbed ions in this inner layer is  $\sigma^i$  ( $\mu\text{C}/\text{cm}^2$ ). Solvated ions can approach the metal only to a distance  $d_a$ . The locus of the centers of these nearest solvated ions is called the outer Helmholtz plane. The interaction of the solvated ions with the charged metal involves

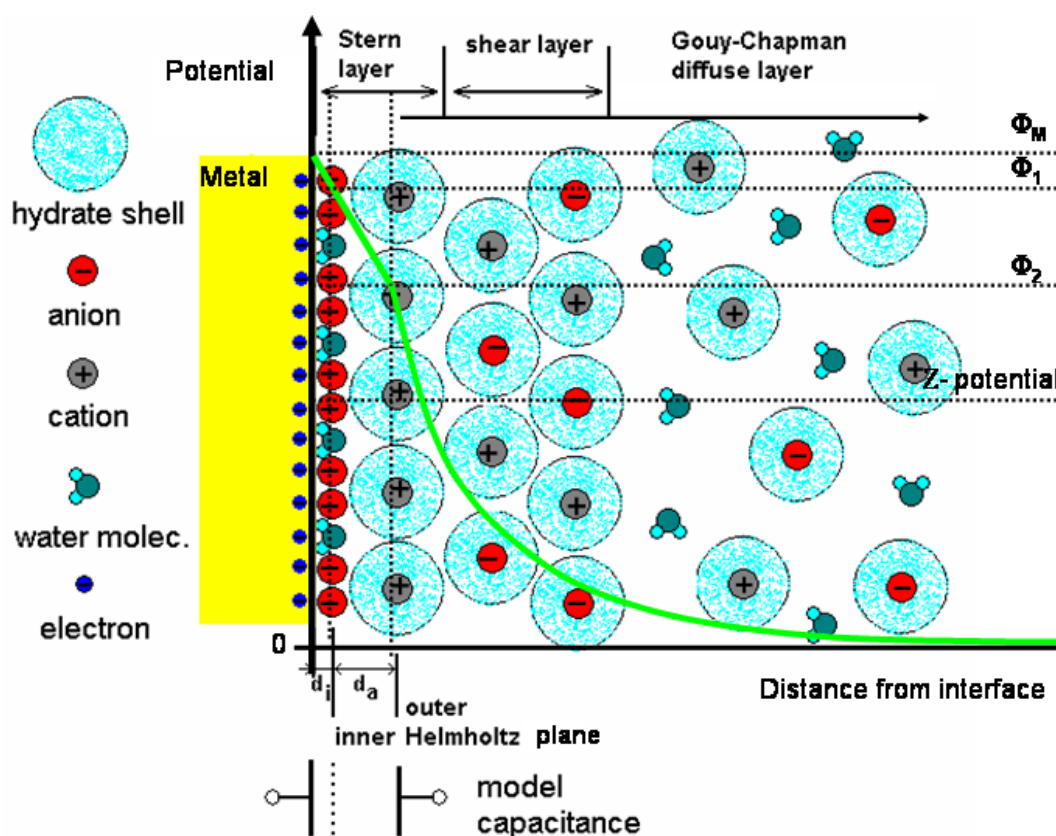


Figure 5.6: Proposed model of double-layer region under conditions where anions are specifically adsorbed.

only long-range electrostatic forces, so that their interaction is essentially independent of the chemical properties of the ions. These ions are said to be nonspecifically adsorbed. Because of thermal agitation in the solution, the nonspecifically adsorbed ions are distributed in a three-dimensional region called the diffuse layer, which extends from the outer Helmholtz plane into the bulk of the solution. The excess charge density in the diffuse layer is  $\sigma^d$ , the total charge density in the double layer is



$$\sigma^i + \sigma^d = -\sigma^M \quad (5.5)$$

where  $\sigma^M$  is the surface charge density of the metal.

The thickness of the diffuse layer depends on the total ionic concentration in the solution. For concentrations greater than  $10^{-2}$  M, the thickness is less than  $\sim 100\text{\AA}$ . The potential profile across the double-layer region is shown as a green line in figure 5.6.

The structure of the double layer can affect the rates of the electrode processes. Consider an electroactive species that is not specifically adsorbed. This species can approach the electrode only to the outer Helmholtz plane, and the total potential it experiences is less than the potential between the electrode and the solution by an amount  $\Phi_2 - \Phi^S$  which is the potential drop across the diffuse layer. Sometimes one can neglect double-layer effects in considering electrode reaction kinetics. At other cases they must be taken into account.

One usually cannot neglect the existence of the double-layer capacitance or the presence of a charging current in electrochemical experiments. Indeed, during electrode reactions involving very low concentrations of electroactive species, the charging current can be much larger than the faradaic current for the reduction or oxidation reaction.[34] For an extended description of this matter the reader is referred to literature [34].<sup>1</sup>

### 5.2.2 Electrochemical Impedance Spectroscopy

In general, the electrochemical impedance spectroscopy (EIS) is applied for investigations on electrochemical properties of diverse materials. By means of EIS one can gain information about the quality of film coatings, electrode or corrosion processes. Meanwhile, this technology increasingly finds application in biotechnology.

The EIS consists of the measurement of phase and current which is the response of the system to an applied alternating voltage. The impedance of a system is in fact the AC resistance. The properties of the electrochemical systems can mainly be described by ohmic resistors and capacitors. Exciting a system by means of an alternating potential, the capacitive elements cause a phase shifted current. Ohmic resistors do not show a frequency dependence. The impedance can be split into a real and imaginary part. The absolute value of the vector corresponds to the impedance and the angle between the current and voltage vectors. The system of interest can be excited by means of a sinusoidal alternating voltage in the range between 1 mHz and 1 MHz. The current response can then be recorded and displayed in different plots. In most cases a three-electrode arrangement consisting of a working electrode (WE), a counter electrode (CE), and a reference electrode (RE) is used. A very low current must flow between the WE and the RE in order to avoid an ohmic potential drop. Since non-linear behavior is cannot be excluded a priori, very small amplitudes of about 5-10 mV are applied for the excitation. The excitation

$$E(t) = E_0 \cdot \sin(\omega t) \quad (5.6)$$

---

<sup>1</sup>Subsection has been transferred from a textbook [34].

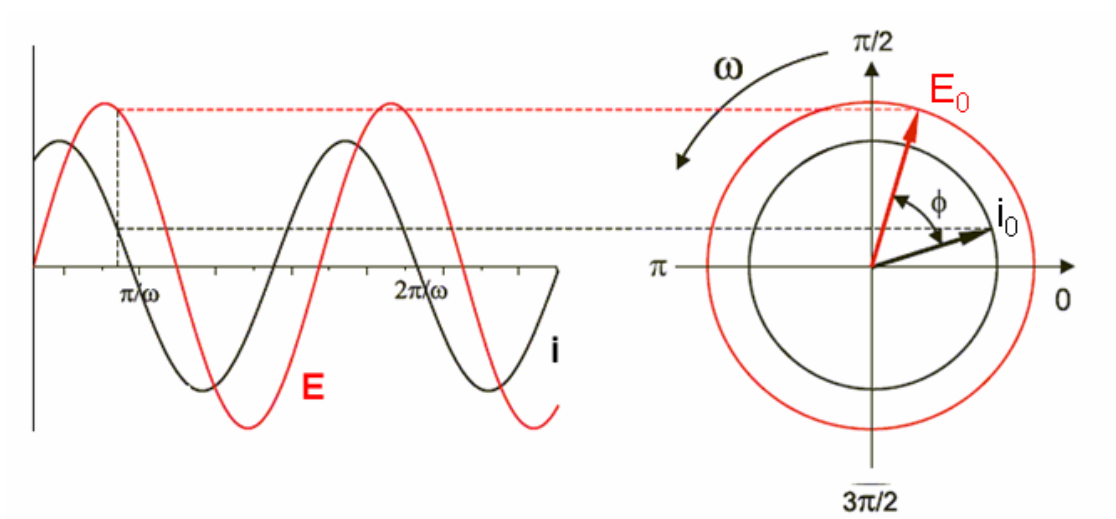


Figure 5.7: Time-dependence of potential  $E(t)$  (red) and current response  $i(t)$  (black).  $\omega = 2\pi f$  where  $f$  denotes the frequency, and  $\phi$  is the phase shift.

elicits a  $\phi$ -shifted current, where  $\omega = 2\pi f$  and  $f$  denotes frequency

$$i(t) = i_0 \cdot \sin(\omega t + \phi) \quad (5.7)$$

The impedance  $Z(t)$  is described by

$$Z(t) = E(t)/i(t) = [E_0 \cdot \sin(\omega t)]/[i_0 \cdot \sin(\omega t + \phi)] = Z_0 \cdot \sin(\omega t)/\sin(\omega t + \phi) \quad (5.8)$$

With the help of Euler's identity,  $\exp\{i\phi\} = \cos\phi + i\sin\phi$ , the alternating potential and current can be expressed in complex forms

$$E(t) = E_0 \cdot \exp\{i\omega t\} \quad (5.9)$$

$$i(t) = i_0 \cdot \exp\{i\omega t - \phi\} \quad (5.10)$$

With these equations, the impedance can be written as

$$Z(t) = E(t)/i(t) = E_0 \cdot e^{i\omega t}/i_0 \cdot e^{i\omega t - \phi} = E_0/i_0 \cdot e^{i\phi} = |Z| \cdot e^{i\phi} = Z' + Z'' \quad (5.11)$$

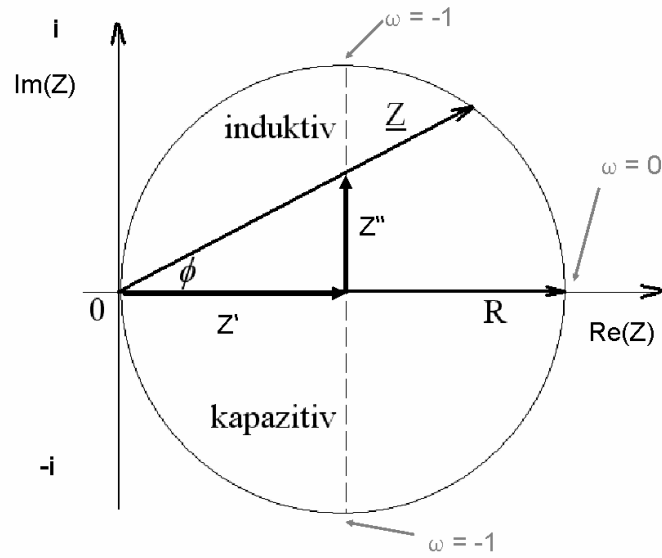


Figure 5.8: Scheme of complex impedance.

With this expression it becomes evident that the impedance is not time- but frequency-dependent. The real part which is the resistance and the imaginary part which is the reactance of the complex impedance are given by:

$$\operatorname{Re}(Z) =: Z' = |Z| \cdot \cos \phi \quad (5.12)$$

$$\operatorname{Im}(Z) =: Z'' = |Z| \cdot \sin \phi \quad (5.13)$$

The complex impedance is illustrated in figure 5.8. Furthermore, the following equations are valid in this context:

$$|Z| = \sqrt{(Z')^2 + (Z'')^2} \quad (5.14)$$

$$\phi = \arctan (Z''/Z') \quad (5.15)$$

The complex conductivity called admittance is the inverse value of  $Z$ :

$$\begin{aligned} Y &= Y' + iY'' = 1/Z \\ &= 1/(Z' + iZ'') = Z'/[(Z')^2 + (Z'')^2] - iZ''/[(Z')^2 + (Z'')^2] \end{aligned} \quad (5.16)$$

with

$$Y' = Z' / [(Z')^2 + (Z'')^2] \quad (5.17)$$

and

$$Y'' = -iZ'' / [(Z')^2 + (Z'')^2] \quad (5.18)$$

Frequency scans can be presented in three different ways:

- **The Bode plot:** The absolute value of the impedance  $|Z|$  and the phase shift  $\phi$  are plotted vs. frequency, usually in a double logarithmic plot.
- **The Nyquist plot:** The imaginary part ( $Z''$ ) is plotted vs. the real part ( $Z'$ ) of the impedance. Notice that in this plot information about the phase shift is hidden. ( $Z' \rightarrow Z''$ )
- **The admittance plot:** The imaginary part of the admittance ( $Y''$ ) divided by  $\omega$  is plotted vs. the real part of the admittance ( $Y'$ ) divided by  $\omega$ .

The data can be analyzed by means of equivalent circuits, describing the electric properties of the electrochemical system. Possible circuit elements that can be used for modeling characterizing the system are listed below:

- **The ohmic resistor (R):** Since the ohmic resistance is not frequency-dependent, the impedance of this element does not contain a phase shift.
- **The capacitor (C):** The capacitance is described by

$$Z(C) = -i/(\omega C) \quad (5.19)$$

so that  $Z' = 0$  and  $Z'' < 0$ , hence according to equation 5.15  $\phi = -\pi/2$ . Thus, in a system containing only a capacitive element the current is  $-90^\circ$  degree phase shifted over the entire frequency range.

- **The constant phase element (CPE):** Capacitive elements of electrochemical systems often differ from ideal capacitors dependent on the quality and the homogeneity. The more inhomogeneous a system is on the microscopic scale the more it differs from ideal capacitor. The constant phase element consists of a combination of a capacitor and can be used for a model to fit the data in this case. Since it can be understood as an approximation, it is important for the physical evaluation to apply this element only if the difference from an ideal capacitance is not too high. The impedance is

$$Z(\text{CPE}) = A/(i\omega)^\alpha \quad (5.20)$$

where  $A$  is a frequency-dependent real constant, and  $0 < \alpha < 1$ . The CPE capacitance is characterized on the one hand by the CPE-T value which is a pure capacitance and on the other hand by the CPE-P value which is  $\alpha$  in equation 5.20 indicating the difference between the CPE-T and an ideal capacitor.

The use of EIS for studying bilayer lipid membranes is very well-described in a book chapter which was written by Vallejo and Gervasi [54]. The main sources for this section have been two other PhD theses [81][46].

### 5.2.3 Cyclic Voltammetry

Cyclic voltammetry (CV) provides access to electrode processes. This method can be applied in order to gain information about thermodynamics of redox processes, kinetics of heterogenous electron transfer reactions, adsorption processes as well as coupled chemical reactions. In general, CV is a powerful tool to determine redox potentials, kinetic constants and surface concentrations of redox active molecules being adsorbed onto the electrode. CVs are characterized by their distinct form and their defined peak position

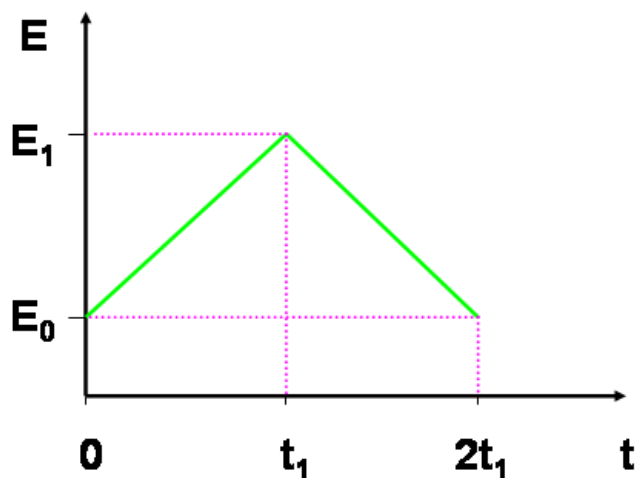


Figure 5.9: Linear potential sweep with two reversal potentials  $E_1$  and  $E_0$  of a cyclic voltammogram.

and intensities. A working electrode (WE) is placed into an electrolyte solution. A time-dependent linearly changing potential  $E(t)$  is applied between the WE and the reference electrode (RE). The scan is started at an initial potential, for example at  $E_0$  (see figure 5.9). When the reversal potential  $E_1$  is reached, a linear potential sweep in the opposite direction is performed to reach the initial potential  $E_0$  again,

$$E(t) = \begin{cases} E_0 + \nu t & \text{for } 0 \leq t \leq t_1 \\ E_1 + \nu(t - t_1) & \text{for } t_1 \leq t \leq 2t_1 \end{cases} \quad (5.21)$$

where  $\nu$  denotes the scan rate,

$$\nu = dE/dt \quad (5.22)$$

The potential sweep for  $0 \leq t \leq t_1$  and  $t_1 \leq t \leq 2t_1$  is called the anodic and the cathodic branch, respectively. Usually, the cycles are repeated several times, and the resulting current through a counter electrode (CE) is recorded. An example for a characteristic current trace is illustrated in figure 5.10. The scan rates can be varied in order to gain information about the kinetics.

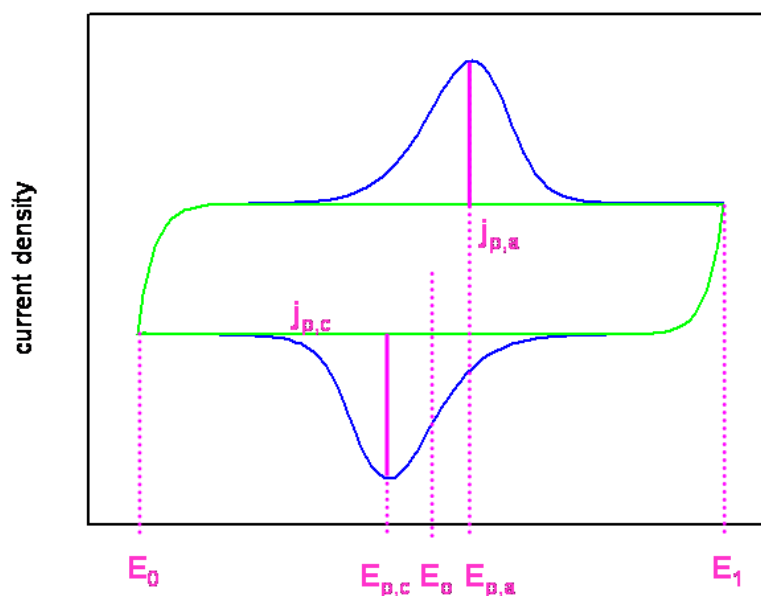


Figure 5.10: Cyclic voltammogram with distinct shape. A reversible charge transfer takes place.  $E_{p,a}$ : anodic peak,  $E_{p,c}$ : cathodic peak,  $E_0$ : redox potential,  $E_1$  and  $E_2$ : reversal potentials.  $j_{p,a}$ : anodic peak current density,  $j_{p,c}$ : cathodic peak current density. The non-faradaic (or capacitive) current and the faradaic current are shown in green and blue, respectively.

Two different sorts of currents occur with electrode processes, the non-faradaic current and the faradaic current.

**Non-faradaic current**, also denoted capacitive currents, is due to the reorganisation of ions near the electrode interface (see figure 5.6). This current density for the  $k^{\text{th}}$  branch is

$$\begin{aligned} j_{c,k} = i_{c,k}/A &= \nu C/A (1 - \exp \{-t/(R_s C)\}) && \text{for } k = 1 \\ &= \nu C/A (1 - 2 \exp \{-t/(R_s C)\}) && \text{for } k = 2, \dots \end{aligned} \quad (5.23)$$

where  $C$  represents the capacitance of the double layer,  $R_s$  is the resistance of the bulk electrolyte solution, and  $A$  denotes the active surface area of the electrode. Note that the algebraic value of  $\nu$  has to be used in this equation.

**Faradaic current** originates from heterogeneous charge transfer processes between electrode and a redox couple being dissolved in the electrolyte,



where  $n$  is the number of transferred electrons in the redox process.  $k_f$  and  $k_b$  denote the rate constants for the forward reaction which is the reduction and the backward reaction which is the oxidation, respectively,

$$k_f = k_o \exp[-n\alpha(E - E_o)/\phi_n] \quad (5.25)$$

$$k_b = k_o \exp[n(1 - \alpha)(E - E_o)/\phi_n] \quad (5.26)$$

where

$$\phi_n = RT/F \quad (5.27)$$

$R$  is the molar gas constant,  $F$  is the Faraday constant and  $T$  is the absolute temperature.  $k_o$  is known as the electrochemical rate constant and  $E_o$  denotes the redox potential of the couple. The parameter  $\alpha$  ( $0 < \alpha < 1$ ) indicates the position of the activation barrier of the electron transfer (ET) (see figure 5.11). In most cases  $\alpha = 0.5$ .

In what follows, only a redox couple confined to the electrode surface is considered. The heterogeneous charge transfer causes a change in the surface concentrations  $\Gamma_O$  and  $\Gamma_R$  of the oxidized and reduced species, respectively:

$$-d\Gamma_O/dt = d\Gamma_R/dt = k_f\Gamma_O - k_b(\Gamma - \Gamma_O) \quad (5.28)$$

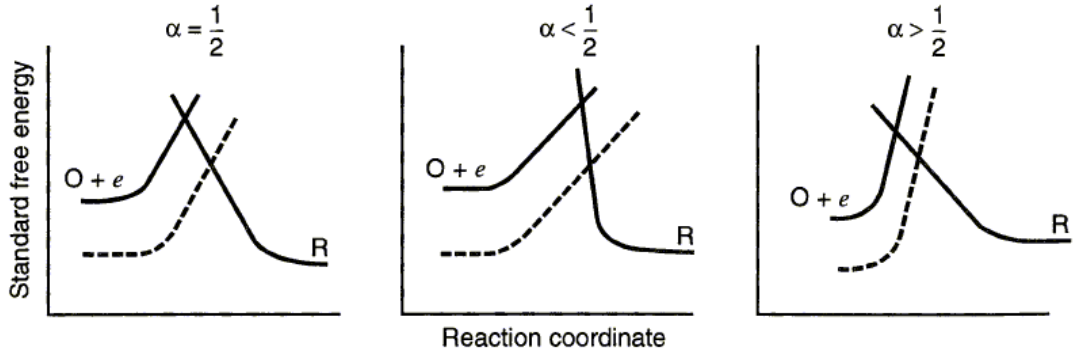


Figure 5.11: Scheme of the activation barrier at different transfer coefficients being an indicator for the symmetry of the barrier to reaction. The dashed line represents the shift in the curve for the reduction of the oxidized species as the potential is made more positive. [34]

where  $\Gamma = \Gamma_{\text{O}} + \Gamma_{\text{R}}$  is the total surface concentration of the redox couple, which is constant for adsorbed species. The faradaic current density  $j_{\text{f}} = i/A$  is related to the change in  $\Gamma_{\text{R}}$  as follows

$$\begin{aligned} j_{\text{f}} &= -nF d\Gamma_{\text{R}}/dt \\ &= -nFk_{\text{o}} \{ \Gamma_{\text{O}} \exp[-n\alpha(E - E_{\text{o}})/\phi_{\text{n}}] - \Gamma_{\text{R}} \exp[n(1 - \alpha)(E - E_{\text{o}})/\phi_{\text{n}}] \} \end{aligned} \quad (5.29)$$

The second form in this equation is obtained by inserting equations 5.28, 5.25, 5.26. Equation 5.29 is commonly known as the Butler-Volmer equation [34]. A typical cyclic voltammogram as described by equations 5.21, 5.23, 5.29 is shown in figure 5.10. The CVs can be characterized by distinct quantities, such as the peak potentials  $E_{\text{p,a}}$  and  $E_{\text{p,c}}$ , the peak currents  $j_{\text{p,a}}$  and  $j_{\text{p,c}}$ , and the average peak potential  $E_{\text{p}} = (E_{\text{p,a}} + E_{\text{p,c}})/2$ . In the ideal case  $E_{\text{p}}$  equals the redox potential  $E_{\text{o}}$  where  $\Gamma_{\text{O}} = \Gamma_{\text{R}}$ . For the peak currents the following relations hold [34]

$$j_{\text{p,a}} = n^2 F^2 \nu \Gamma_{\text{a}} / (4RT) \quad (5.30)$$

$$j_{\text{p,c}} = n^2 F^2 \nu \Gamma_{\text{c}} / (4RT) \quad (5.31)$$

In the ideal case  $\Gamma_{\text{a}} = \Gamma_{\text{c}} = \Gamma$ . Note that  $j_{\text{p}}$  is proportional to  $\nu$ , in contrast to the case of not-adsorbed redox couples, where diffusion processes of redox species occur which causes  $j_{\text{p}}$  to be proportional to  $\sqrt{\nu}$  [34].  $\Gamma$  can be obtained by integrating the faradaic current density of the CV:

$$\Gamma = \int (j_{\text{f}}/\nu) dE / (nF) \quad (5.32)$$



## 5.2.4 ET Model for the Analysis of CcO CVs

### 5.2.4.1 General Concept

The redox protein is considered to be adsorbed to the electrode as shown in figure 5.12.  $\Gamma$  denotes the protein surface concentration. The four redox centers of CcO are num-

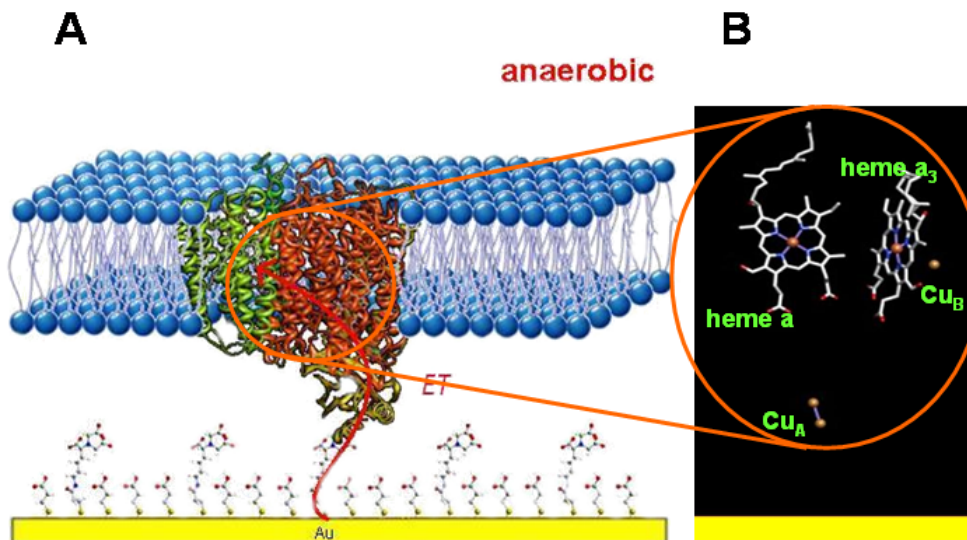


Figure 5.12: Scheme of ptBLM with CcO being tethered via his-tag to a chelat complex at the linker molecule (DTNTA). The enzyme is embedded into a lipid bilayer membrane in a strict orientation (A). The approximate position of the prosthetic groups is shown in (B).  $Cu_A$  is directed towards the electrode.

bered sequentially and are one electron redox couples. ET between the electrode and the complex is denoted as "uptake". The ET within the complex, which is an exchange of electrons between two centers, is denoted as "exchange". A variety of redox states (oxidized or reduced) arising upon ET can be considered as different conformational states of the enzyme, being numbered sequentially. For the  $k^{\text{th}}$  conformation the probability is  $p_k$  and hence

$$\sum_k p_k = 1 \quad (5.33)$$

which is the sum over all conformational states. The transition between the states  $k$  and  $l$  is described by the flow:

$$J_{k,l} = k_{k,l}p_k - k_{l,k}p_l \quad (5.34)$$

where  $k_{k,l}$  and  $k_{l,k}$  are the rate coefficients which depend on the type of ET and the centers which are involved. In the case of electron exchange between the electrode and the redox center  $k_{k,l}$  and  $k_{l,k}$  are given by equations 5.25 and 5.26 with  $n=1$ , hence

$$k_{k,l} = k_{e,i} \exp[-0.5(E - E_{o,i})/\phi_n] \quad (5.35)$$

$$k_{l,k} = k_{e,i} \exp[0.5(E - E_{o,i})/\phi_n] \quad (5.36)$$

$E_{o,i}$  and  $k_{e,i}$  denote the redox potential and the electrochemical rate constant of the  $i^{\text{th}}$  center, respectively. A symmetrical energy barrier is assumed here i.e.  $\alpha=1/2$ . We will refer to this transition as uptake or E-type. However, the exchange of electrons between centers  $i$  and  $j$  is a chemical reaction which we will refer to exchange or C-type. This is described by a forward and a backward rate constant,  $k_{i,j}$  and  $k_{j,i}$ , respectively and follows from detailed balancing [69]:

$$k_{k,l} = k_{i,j} \quad , \quad k_{l,k} = k_{i,j} \exp[(E_{o,i} - E_{o,j})/\phi_n] \quad (5.37)$$

We do not consider redox interactions, so that rate constants of a given ET are not dependent on the redox states of other centers which are not involved in the particular transfer.

The overall probabilities for the  $i^{\text{th}}$  center in the reduced and oxidized state are, respectively,

$$P_{i,\text{red}} = \sum_k P_{k|i,\text{red}} \quad \text{and} \quad P_{i,\text{ox}} = 1 - P_{i,\text{red}} \quad (5.38)$$

$P_{k|i,\text{red}}$  denotes the probability of the  $k^{\text{th}}$  conformation with the  $i^{\text{th}}$  center reduced. The second relation results from equation 5.33. The current density  $j_i$  which is the flow of electrons associated with the  $i^{\text{th}}$  center results is given by

$$j_i = -\Gamma F \sum_k \left[ J_{k,l|i \rightarrow} - \sum J_{k,l|i \leftarrow} \right] \quad (5.39)$$

where  $J_{k,l|i \rightarrow}$  and  $J_{k,l|i \leftarrow}$  describe the flows into the  $i^{\text{th}}$  center and out of it. The current density  $j_{\text{el}}$  which is passing the electrode is

$$j_{\text{el}} = \sum_i j_i = -n_e F \sum J_{k,l|\text{up}} \quad (5.40)$$

and  $J_{k,l|up}$  denotes flows pertaining to electron uptake.

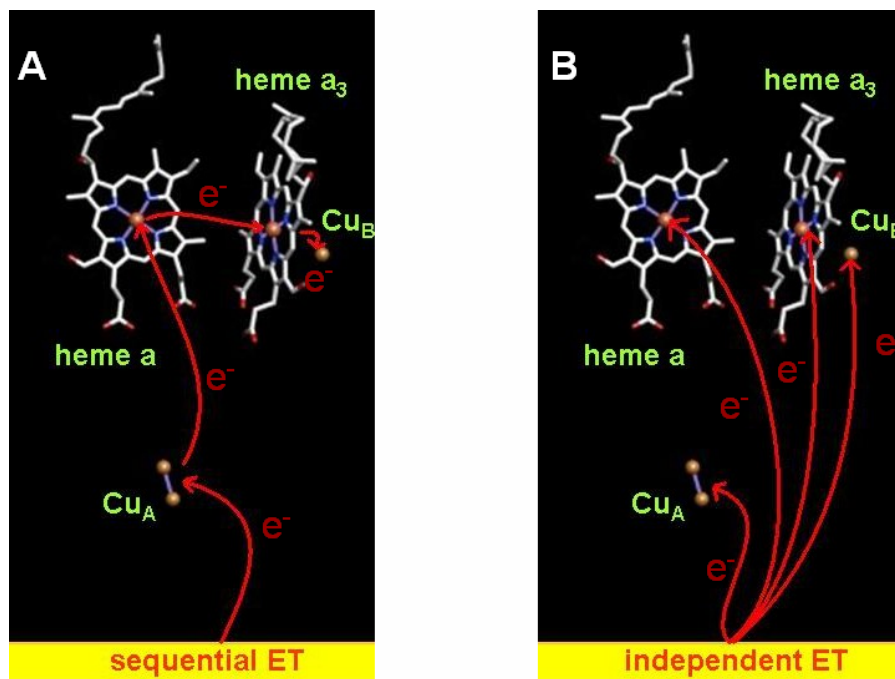


Figure 5.13: Scheme of two ET mechanisms towards the redox centers of CcO. (A) The sequential reduction follows the ECCC mechanism, where  $Cu_A$  is electrochemically reduced by the electrode. A chemical reduction of the following redox centers by this particular electron takes place subsequently. Further three more electrons can be taken up in this way. (B) The independent ET to the protein, another possible mechanism, bases on the EEEE mechanism, in which each of the redox centers is reduced by the electrode separately.

#### 5.2.4.2 Electron Transfer at Pseudo-Equilibrium

In the case of a very low change in potential with time  $t$  (at sufficiently low scan rates), the redox centers are close to equilibrium with respect to  $E$ . This is called the pseudo-equilibrium and the corresponding ET is denoted "equilibrated electron transfer". The Nernst equation

$$E = E_{o,i} + \phi_n \ln(p_{i,ox}/p_{i,red}) \quad (5.41)$$

then applies to the overall probabilities  $p_{i,red}$  and  $p_{i,ox}$  hence (see equation 5.38)

$$p_{i,red} = \{1 + \exp[(E - E_{o,i})/\phi_n]\}^{-1} \quad (5.42)$$

The current density  $j_i$  of the  $i^{\text{th}}$  center is given by (see equation 5.29)

$$\begin{aligned} j_i &= -\Gamma F \, dp_{i,\text{red}}/dt = -(\Gamma F \nu) dp_{i,\text{red}}/dE \\ &= (\Gamma F \nu / \phi_n) \exp[(E - E_{o,i})/\phi_n] \{1 + \exp[(E - E_{o,i})/\phi_n]\}^{-2} \end{aligned} \quad (5.43)$$

#### 5.2.4.3 Sequential Electron Transfer (ECCC Mechanism)

A cartoon of sequential ET is shown in figure 5.13 (A) and the corresponding scheme describing the ECCC mechanism is presented in figure 5.14 (A). The center 1, which is  $\text{Cu}_A$ , can take up electrons from the electrode. The other centers 2, 3, and 4, which are heme a, heme  $a_3$  and  $\text{Cu}_B$ , respectively, can only exchange electrons with their direct neighbors i.e., center  $i$  exchanges electrons with centers  $i+1$  and/or  $i-1$ .

#### 5.2.4.4 Independent Electron Transfer (EEEE Mechanism)

Each center can take up electrons from the electrode independently, and electron exchange between neighbors is excluded (see figure 5.13 (B)). The pertinent scheme is presented in figure 5.14 (B). An unambiguous assignment of centers 1–4 to the redox centers in CcO is not possible here.

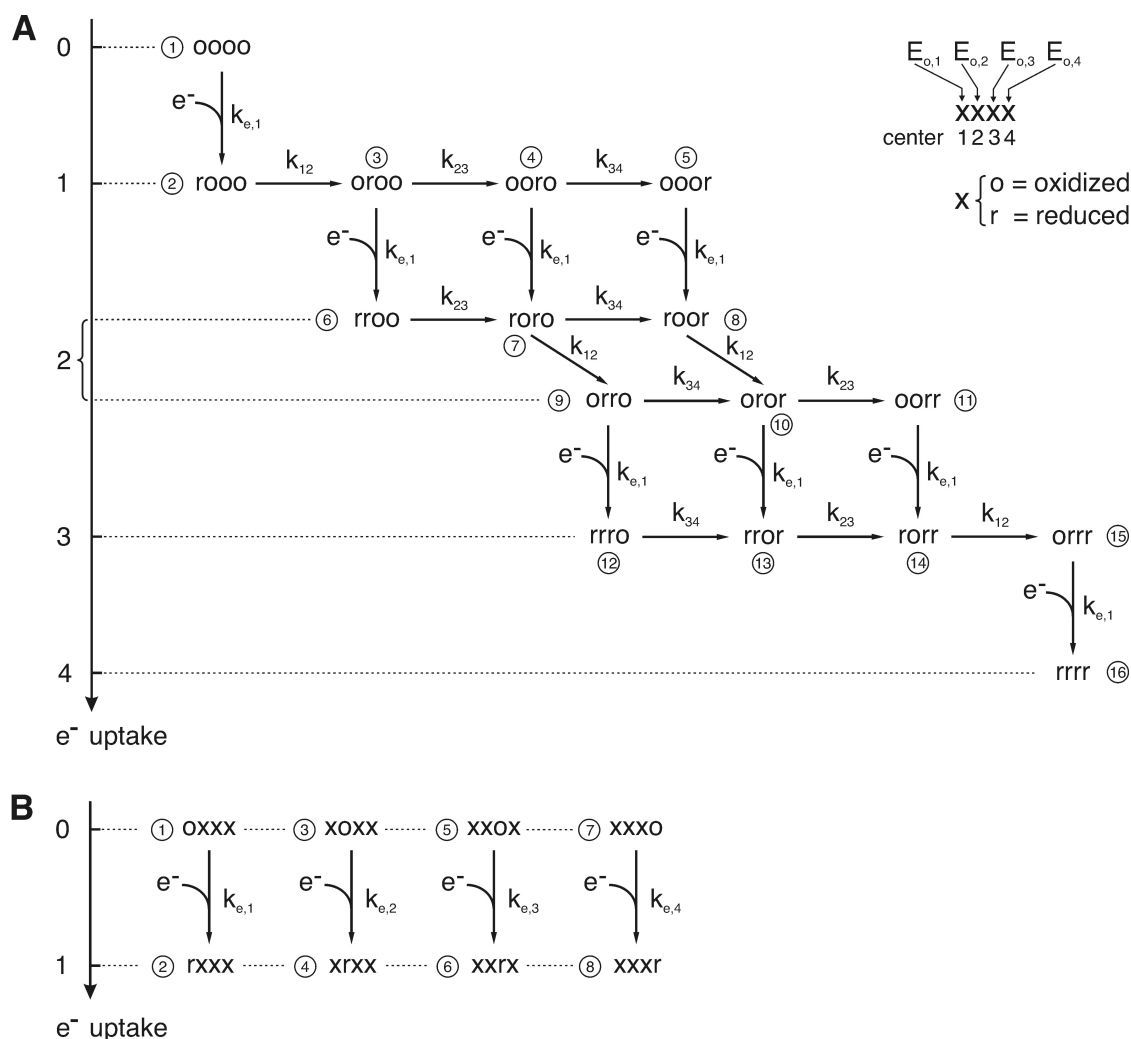


Figure 5.14: Detailed description of sequential and independent ET.

## 5.3 Infrared Spectroscopy

### 5.3.1 Absorption of Light

The possible energy states of a molecule are discrete (quantized). If the transition between two energy states  $E_1$  and  $E_2$  takes place, the system can only absorb or emit  $\Delta E = E_1 - E_2 = h\nu$ . Selection rules therefore confine the possible transitions. With IR spectroscopy a broad spectrum of IR radiation is coupled into the sample. The sample absorbs particular frequencies which appear attenuated in the emitted spectrum. In this context the intensity is proportional to the square of the electrical field of the incident radiation:  $I \propto E^2$ . The frequency-dependent incident radiation intensity is denoted  $I_0(\nu)$  and the emitted radiation intensity is  $I(\nu)$ . The transmission  $T(\nu)$  can then be calculated by means of:

$$T(\nu) = I(\nu)/I_0(\nu) \quad (5.44)$$

In 1760, Lambert found out that the decrease of radiation intensity is proportional to the intensity when passing a medium:

$$dI' = -\alpha I' dx \quad (5.45)$$

The following equation is valid for a sample with a thickness  $d$ :

$$\int_{I'=I_0}^I dI'/I' = - \int_0^d \alpha dx \quad (5.46)$$

$$\ln I/I_0 = -\alpha d \quad (5.47)$$

In 1852, Beer realized the influence of the concentration  $c$  on the intensity attenuation.

$$\ln I/I_0 = -\alpha' c d \quad (5.48)$$

$\alpha'$  is Napier's absorption coefficient (natural logarithm). Applying the decade logarithm the Lambert-Beer's equation can be obtained:

$$T(\nu) = I(\nu)/I_0(\nu) = \exp[-\alpha' cd] = 10^{\epsilon(\nu)cd} \quad (5.49)$$

with the decade absorption coefficient  $\epsilon(\nu) = \alpha'(\nu) \cdot \log(e)$ . The exponent is also known as the absorbance,  $A(\nu) = \epsilon(\nu)cd$ , where  $\epsilon(\nu)$  denotes the extinction coefficient,  $c$  denotes the concentration in mol/l and  $d$  is the thickness of the sample.

This relation which has been described by Bouguer, Lambert and Beer is valid for diluted solvents [12].

#### 5.3.2 General Concept

The electromagnetic spectrum can be subdivided into domains which are characterized by the type of interaction being apparent at a particular radiation energy. In general, electromagnetic radiation is determined by its Energy  $E$ , the corresponding wavelength  $\lambda$ , the frequency  $\nu$  and the wavenumber  $\tilde{\nu}$ . The energy which is achieved by a molecule is the sum of translation, rotation, vibration and electronic energy. In an approximation each type of energy can be regarded separately. For example the electronic transition generates absorption or emission in the UV-vis window of the electromagnetic spectrum. Rotation

transitions occur in the microwave and far infrared region. This excitation results in a warming effect of the material. Molecular vibrations effect absorption in the entire infrared region. The infrared electromagnetic radiation is located between the visible and the microwave region (see figure 5.15 and table 1). This region is distinguished by changes in the molecule configuration.

Type of change	Region	$\nu$ / Hz	$\lambda$ / cm	$\tilde{\nu}$ / $\text{cm}^{-1}$
electron distribution	ultraviolet	$3 \cdot 10^{16}$ - $7.9 \cdot 10^{14}$	$1 \cdot 10^{-6}$ - $3.8 \cdot 10^{-5}$	$1 \cdot 10^6$ - $2.63 \cdot 10^4$
	visible	$7.9 \cdot 10^{14}$ - $3.8 \cdot 10^{14}$	$3.8 \cdot 10^{-5}$ - $7.8 \cdot 10^{-5}$	$2.63 \cdot 10^4$ - $1.28 \cdot 10^4$
molecular configuration	near infrared	$3.8 \cdot 10^{14}$ - $1.2 \cdot 10^{14}$	$7.8 \cdot 10^{-5}$ - $2.5 \cdot 10^{-4}$	$1.28 \cdot 10^4$ - $4 \cdot 10^3$
	mid infrared	$1.2 \cdot 10^{14}$ - $6 \cdot 10^{12}$	$2.5 \cdot 10^{-4}$ - $5 \cdot 10^{-3}$	$4 \cdot 10^3$ - $2 \cdot 10^2$
	far infrared	$6 \cdot 10^{12}$ - $3 \cdot 10^{11}$	$5 \cdot 10^{-3}$ - $1 \cdot 10^{-1}$	$2 \cdot 10^2$ - $10^1$
molecular orientation	microwave	$1 \cdot 10^{12}$ - $3 \cdot 10^8$	$1 \cdot 10^{-1}$ - $1 \cdot 10^2$	$1 \cdot 10^1$ - $1 \cdot 10^{-2}$

Table 1: Regions of the electromagnetic spectrum.

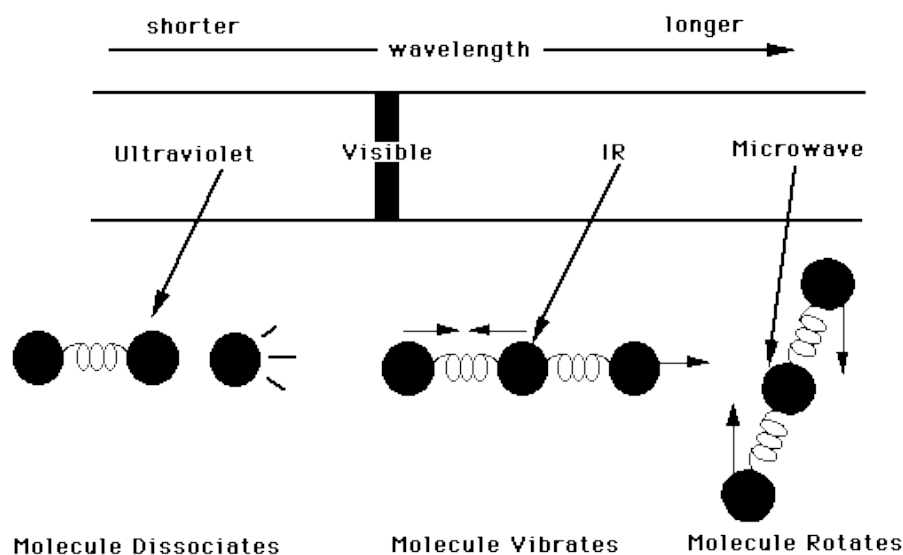


Figure 5.15: Types of molecule excitations. [73]

The infrared window can be subdivided into three regions, the near, the mid and the far infrared. The mid infrared region is of greatest practical use to the organic chemist and for this reason it has been applied in this work. Wavelength  $\lambda$  and frequency  $\nu$  are related by the following equation:

### 5.3 Infrared Spectroscopy

$$\lambda = c/\nu \quad (5.50)$$

and the wavenumber is related to the frequency and the wavelength as follows:

$$\tilde{\nu} = \nu/c \quad , \quad \tilde{\nu} = 1/\lambda \quad (5.51)$$

The corresponding energy can be calculated by:

$$E = h\nu = hc_0/\lambda \quad (5.52)$$

where  $h$  is Planck's constant and  $\nu$  is equivalent to the classical frequency.

Infrared light is absorbed by organic molecules being converted into vibrational energy. Absorption occurs in the case if the energy of the radiation matches exactly the energy of the vibration. In figure 5.16 the chemical bonds and the type of vibrations are displayed for different wavenumbers.

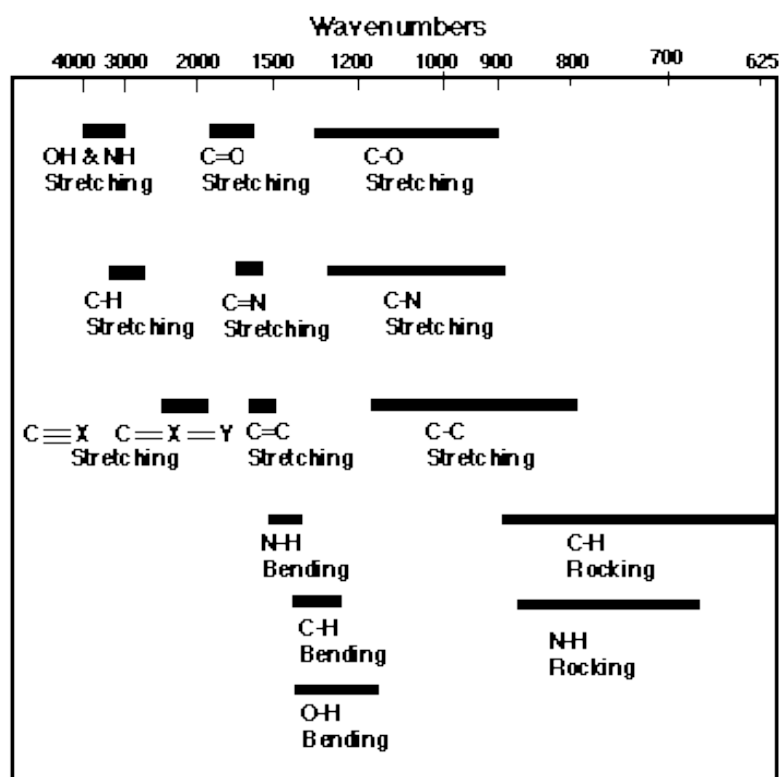


Figure 5.16: Chemical bonds and their vibration types for different wavenumbers.[73]



### 5.3.2.1 Molecular Vibrational Modes

In an approximative model referring to the classical case a molecule can be imagined consisting of masses which correspond to the atoms and of springs which correspond to the electromagnetic forces between the atoms. The massless springs are considered to have restoring forces. A molecule consisting of  $n$  atoms has a total of  $3n$  degrees of freedom, corresponding to the three Cartesian coordinates for each of the  $n$  molecules. If the molecule is nonlinear, three of these degrees of freedom can be related to the rotation and another three can be related to translation. For a linear molecule only two degrees of freedom are existent resulting from rotation and again three degrees of freedom result from translation. The net number of fundamental vibrations is related to the molecule type in table 2. A simple molecule such as propane for example ( $C_3H_8$ ) thus has 27 fun-

molecule	degree of freedom
nonlinear	$3n - 6$
linear	$3n - 5$

Table 2: Net number of fundamental vibrations for two different molecule types.

damental vibrations. For this reason the spectrum of propane is supposed to contain 27 bands. In figure 5.17 the three fundamental vibrations of water which is nonlinear are demonstrated. Carbon dioxide ( $CO_2$ ) on the contrary has a linear structure thus coming

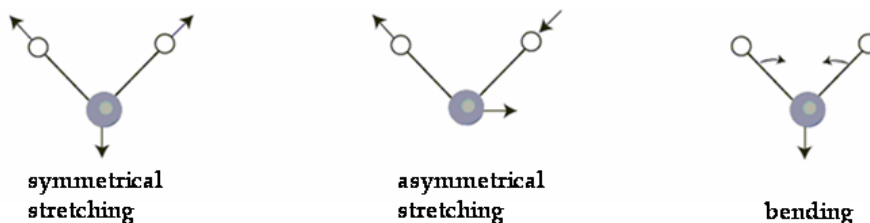


Figure 5.17: Stretching and bending vibrational modes for  $H_2O$ . [71]

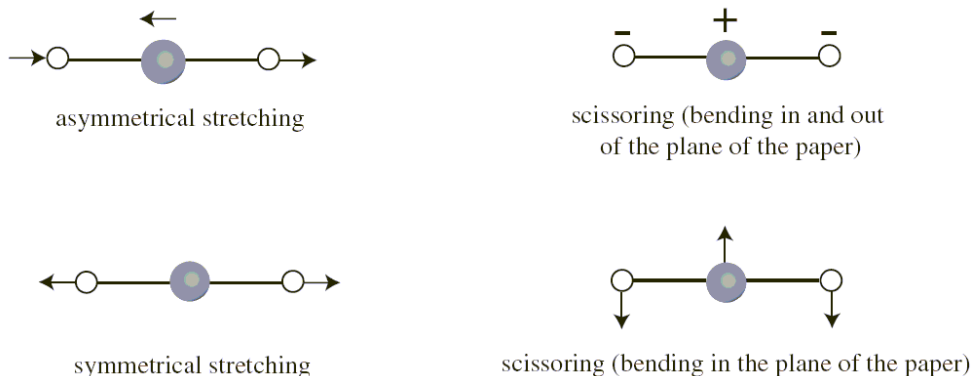


Figure 5.18: Stretching and bending vibrational modes for  $CO_2$ . [71]

with four fundamental vibrations as shown in figure 5.18. The two scissoring or bending vibrations are equivalent thus having the same frequency and being degenerate. This particular vibration absorbs the infrared radiation at  $666\text{ cm}^{-1}$ . Not every vibration is infrared active. In the case of  $\text{CO}_2$ , the symmetrical stretch is not IR active because the stretch does not generate a change in the dipole moment. This is also a reason for the discrepancy between the number of fundamental vibrations and occurring bands in the spectrum. Some linear molecules such as hydrogen, nitrogen or chlorine do not absorb IR radiation at all. The stronger a dipole moment changes the more distinct the accordant band appears.

### 5.3.2.2 Classical Model for Stretching Vibrations

The stretching of a molecule with two atoms can be described in an approximation by means of Hooke's law. Therefore two atoms and the connecting bond are treated as a simple harmonic oscillator being composed of two masses  $m_1$  and  $m_2$  connected by a spring. The maximum deflection from the position of rest is  $X_1$  for  $m_1$  and  $X_2$  for  $m_2$ .

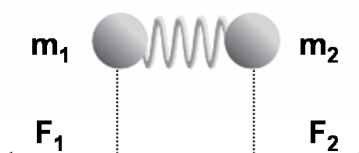


Figure 5.19: Classical model for molecule stretching. The molecule consists of two atoms being connected by a backdriving spring force. [71]

The total distance is then  $(X_2 - X_1)$ . The spring has a backdriving force according to Hooke's law, which is proportional to the deflection and characterized by a proportionality constant  $F$ . The corresponding equation is given by:

$$F(X_2 - X_1) = m_1 \cdot d^2X_1/dt^2 \quad , \quad -F(X_2 - X_1) = m_2 \cdot d^2X_2/dt^2 \quad (5.53)$$

the solutions for the differential equations, describing the simple harmonic oscillations, are:

$$X_1 = A_1 \cos(2\pi\nu t + \alpha) \quad , \quad X_2 = A_2 \cos(2\pi\nu t + \alpha) \quad (5.54)$$

where  $A_1$  and  $A_2$  are the amplitudes of the deflections. Deriving the equations 5.54 twice and inserting the  $X_1$  and  $X_2$  values as well as inserting their second derivatives into equation 5.53 results in:

$$F(A_2 - A_1) = -m_1 A_1 4\pi^2 \nu^2 \quad , \quad F(A_2 - A_1) = m_2 A_2 4\pi^2 \nu^2 \quad (5.55)$$

the frequency is then given by:

$$\nu = 1/(2\pi) \sqrt{F (1/m_1 + 1/m_2)} \quad (5.56)$$

With the help of the reduced mass  $u$

$$u = m_1 m_2 / (m_1 + m_2) \quad (5.57)$$

the equation can then be expressed as follows:

$$\nu = 1/(2\pi) \sqrt{F/u} \quad (5.58)$$

It is obvious that the frequency is independent from the amplitudes. The proportionality constant,  $F$ , can be calculated by the following expression:

$$F = 4\pi^2 \nu^2 u \quad (5.59)$$

and the energy is then:

$$E = 1/2 F \hat{X}^2 \quad (5.60)$$

with the maximum deflection  $\hat{X} = X_2 - X_1$ .

### 5.3.2.3 Quantum Mechanical Model for Stretching Vibrations

The classical model for the oscillator allows that the deflection can achieve any value. If this would be the case in reality, the vibrations would absorb a continuum of the spectrum. In the quantum mechanical model the vibrational motion is expected to be quantized (see figure 5.20). This means that the vibrations follow the quantum mechanical rules which implies the existence of selection rules for transitions:

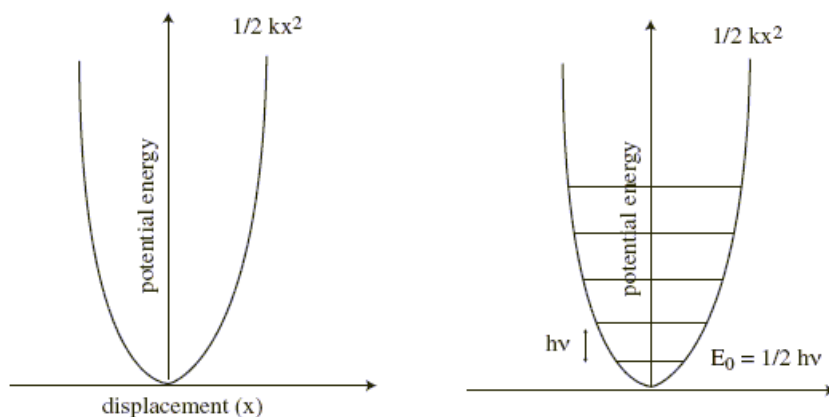


Figure 5.20: Energy curve for a vibrating spring in the classical model (left) and the quantum mechanical model (right). [71]

$$E = (n + 1/2) h\nu \quad (5.61)$$

where  $\nu$  is the frequency of the vibration and  $n$  is the quantum number ( $n=0,1,2,3,4..$ ). For  $n=0$  the lowest energy level is achieved  $E = 1/2h\nu$ . According to the selection rule, only transitions to the next higher or lower energy level are allowed:  $\Delta n = \pm 1$ . Most infrared excitations occur between the ground and the first excitation state ( $n = 0 \rightarrow n = 1$ ). The classical model is a rough approximation and in reality a molecule is not just a composition of two masses connected by a spring. The bond cannot be compressed beyond a certain point. In reality the molecule is an anharmonic oscillator (see figure 5.21). As the interatomic distance increases the energy reaches a maximum. The vibrational frequency  $\bar{\nu}$  for a diatomic molecule can be calculated by applying the equation derived from Hooke's law:

$$\bar{\nu} = 1/(2\pi c)\sqrt{F/u} \quad (5.62)$$

where  $c$  is the velocity of light.

For rotational transitions the following relation is valid:

$$E_{\text{rot}} = l(l + 1) \hbar^2/(2uX^2) \quad (5.63)$$

$l$  is the quantum number of the orbital angular momentum and  $\hbar = h/2\pi$ . The energy of a vibrational transition is usually 100-times higher than the energy referring to a rotational transition. The rotational transitions that can occur take place between the

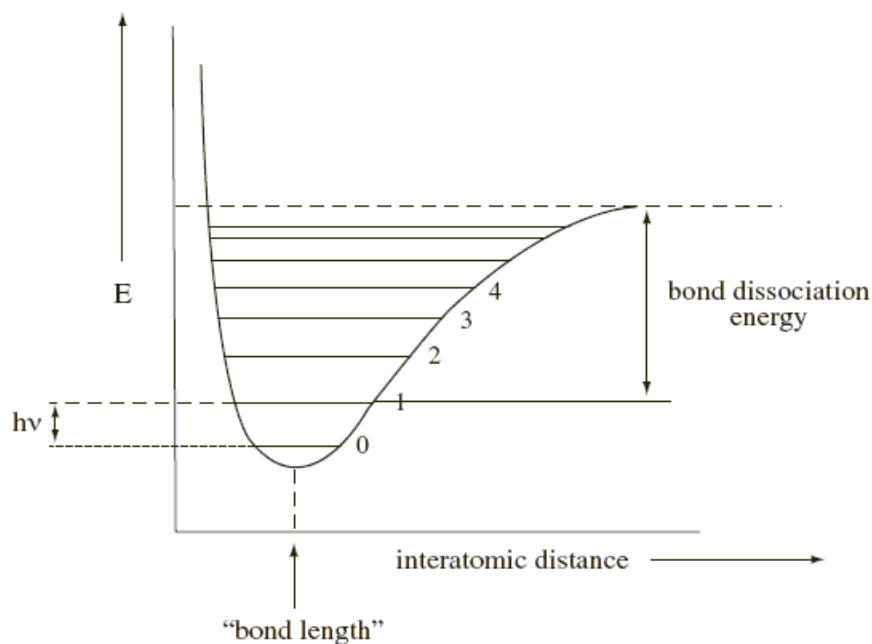


Figure 5.21: Energy curve of an anharmonic oscillator. [71]

quantum numbers such as  $l = 0 \rightarrow l = 1$  or  $l = 1 \rightarrow l = 2$  and  $l = 2 \rightarrow l = 3$  and so on. Again the selection rule:

$$\Delta l = \pm 1 \quad (5.64)$$

is valid. The molecule's dipole momentum changes with the absorption of IR radiation and therefore

$$I_{\text{IR}} \propto |\partial\mu/\partial Q| \cos^2 \Theta \quad (5.65)$$

is valid. The intensity  $I_{\text{IR}}$  is thus proportional to the square of the change of the dipole momentum. In this context the dipole momentum can be static and ever existent like in the case of  $\text{H}_2\text{O}$  or the dipole momentum occurs just temporarily during the interaction of molecule and radiation like in the case of  $\text{CO}_2$ .

This model has been described only for a linear molecule consisting of two atoms. In this case only  $3N - 5 = 1$  fundamental vibration is existent. For a nonlinear molecule with three atoms like the  $\text{H}_2\text{O}$  three fundamental vibrations can occur (see figure 5.17) and taking them all into account the calculations become more complicated with an increasing number of atoms and bonds. However, particular groups of atoms behave the

same in different molecules. Those are called group vibrations with distinct group frequencies. They can be identified in the infrared spectrum because their bonds generate characteristic bands (see figure 5.16). For this reason, characteristic amide bands occur in the spectra of proteins resulting from the peptide chains. Furthermore, regions which are called "fingerprint"-regions occur indicating the existence of particular molecules in the sample. Additionally, the interactions between different groups also appear as absorption bands in the spectra which makes it more complex to analyze. [81]

### 5.3.3 Infrared Spectroscopy with Proteins

Proteins consist of a large number of peptide and the inter- and intramolecular forces are complex. IR spectra of proteins yield information about vibrational modes of amino acids and peptide groups. The shape of bands is determined by the quantity of involved groups and the influence of the environment. The shape of the bands can be Gaussian (see equation 5.66) which occurs for gas under low pressure for example. Lorentzian shapes (see equation 5.67) often occur in conjunction with chemicals that are dissolved in a non-interacting solution under high pressure. Polar solutions like water or solids often produce bands in the spectra which can be described by the Voigt shape (see equation 5.68). This is a convolution of the Gaussian and the Lorentzian band shape. The following equations describe the possible band shapes:

$$G(x) = \exp(-x^2/2\sigma^2) / \sigma\sqrt{2\pi} \quad (5.66)$$

$$L(x) = \gamma/\pi(x^2 + \gamma^2) \quad (5.67)$$

$$V(x) = (G * L)(x) = \int G(\tau)L(x - \tau)d\tau \quad (5.68)$$

A very important interaction in biological material results from the hydrogen bridge linkages. These types of bonds help stabilizing the structure of biological molecules, such as  $\alpha$ -helices or  $\beta$ -sheets. Since the spring constant of a bondage changes with the intermolecular interaction, the group frequency shifts. For this reason every protein has a unique spectrum. See literature [81].

#### 5.3.3.1 Amide Bands

IR spectra of proteins or polypeptides typically contain strong absorption bands resulting from peptide bonds (CONH-groups). In figure 5.22 an example for a polypeptide chain is demonstrated. Nine bands occurring in conjunction with proteins are assigned to the CONH-groups. For further details see [10][11]. Based on a reconstruction of the dynamics of peptide force fields [10] the frequencies of the different amide bands have been calculated [175]. The most important amide bands when dealing with proteins are the amide I and amide II bands occurring at approximately  $1650 \text{ cm}^{-1}$  and  $1550 \text{ cm}^{-1}$ , respectively. Assuming an infinite polypeptide chain the vibration frequencies can be derived from:

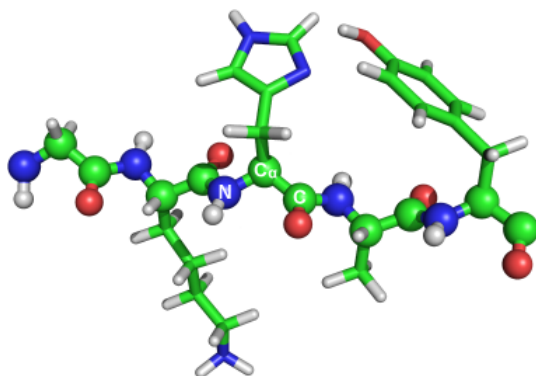


Figure 5.22: Example of a polypeptide chain.

$$\nu(\delta, \delta') = \nu_0 + \sum_j D_j \cos(j\delta) + \sum_j D'_j \cos(j\delta') \quad (5.69)$$

which is the perturbation theory of first order. It can be applied in order to calculate the IR-modes of the peptide bonds [10].  $\nu_0$  denotes the undisturbed frequency of the isolated group generating the amide band.  $D_j$  is the coupling constant between the amide-group and the element of the molecular chain with index  $j$ .  $\delta$  is the phase difference between the atomic frequencies of the molecule groups. These parameters describe the interaction in one single molecule chain, whereas  $D'_j$  and  $\delta'$  describe the according interactions between different molecule chains. The definite position of the amide bands is also determined by the secondary structure of the protein.[81]

### 5.3.4 Fourier-transform Infrared Spectrometers

In figure 5.23 the principle of the FTIR spectrometer is demonstrated. The IR beam is split into two beams with the same intensity. One of them passes the sample ( $I(\nu)$ ) and the other one serves as a reference ( $I_0(\nu)$ ). The spectrometer contains a source of radiation which can be a spiral coil of silicon carbide emitting constantly the same spectrum of infrared light at approximately 1500 K. In the classical IR spectrometer the beam of IR radiation is focussed on the sample and after transmission it passes a monochromator and reaches the detector. Since the recording of single signals for different frequencies is inappropriate, the FTIR-spectrometer in which the beam passes an interferometer instead of a monochromator has been introduced (see figure 5.23). The detector records the transmitted light intensity and transforms it into electrical signals driving the chart recorder to generate a spectrum. Alternatively, the data can be recorded and evaluated by a computer making use of data processing. In detail, the detector of the FTIR spectrometer records an interferogram which is converted subsequently into a conventional IR spectrum. The interferogram is a complex superposition resulting from interfering frequencies being emitted from the sample. It is generated by the two light beams which

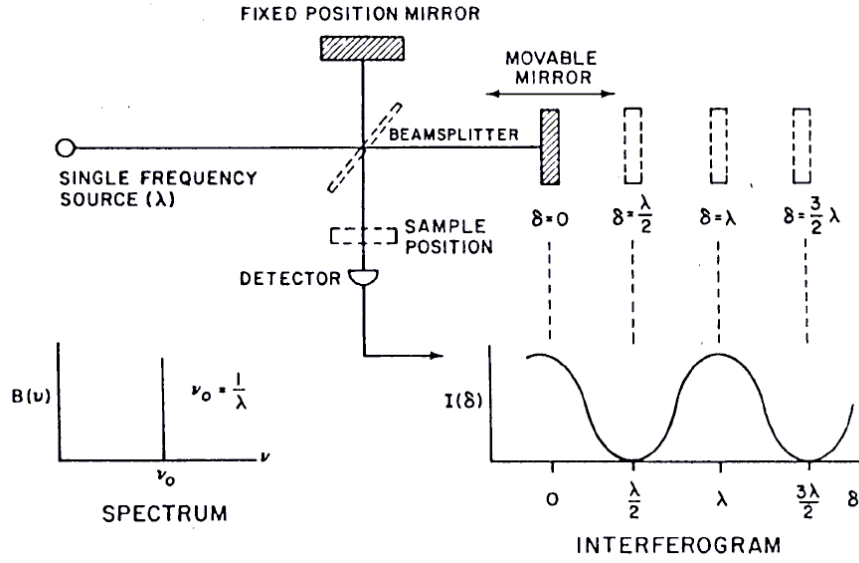


Figure 5.23: Principle of a FTIR spectrometer. With the help of the Michelson interferometer the interferogram/spectrum can be recorded. Both are displayed for a monochromatic radiation source in this scheme.  $\delta$  is the optical pathway between fixed and movable mirror. [12]

are reflected at the movable and the fixed mirror and interfering at the detector. The interferogram contains all the information about the frequencies which have been absorbed by the sample. The Fourier-transformation converts the interferogram which is characterized by the position of the mirror into an intensity vs. frequency or wavenumber plot. The transformation can be calculated according to:

$$I^{AC}(\delta) = \int_0^{\infty} B(\tilde{\nu}) \cos(2\pi\tilde{\nu}\delta) \cdot d\tilde{\nu} \quad (5.70)$$

where  $\delta$  is the difference between the distance of the movable mirror towards the beamsplitter and the distance of the fixed mirror towards the beamsplitter.  $B(\tilde{\nu})$  is defined by:

$$B(\tilde{\nu}) = H(\tilde{\nu})I(\tilde{\nu})/2 \quad (5.71)$$

$I(\tilde{\nu})$  denotes the wavenumber-dependent intensity and the factor  $H(\tilde{\nu})$  contains information about the properties of the optical instruments being passed by the beam. Equation 5.70 acts as a Fourier series with  $B(\tilde{\nu})$  as Fourier coefficients.  $B(\nu)$  results from the transformation:

$$B(\nu) = \int_{-\infty}^{\infty} I^{AC}(\delta) \cos(2\pi\tilde{\nu}\delta) \cdot d\delta \quad (5.72)$$



The absorption of the sample then results from:

$$A(\tilde{\nu}, t) = -\log[I_S(\tilde{\nu}, t)/I_R(\tilde{\nu})] \quad (5.73)$$

where  $I_S(\tilde{\nu}, t)$  denotes the intensity of the beam after the passage of the sample and  $I_R(\tilde{\nu})$  denotes the intensity of the reference beam. Alternatively,  $I_R(\tilde{\nu})$  can also be the intensity of the reference beam being emitted by a sample at the beginning of a process and  $I_S(\tilde{\nu}, t)$  would then be the respective intensity of the same sample after the process is finished. The resulting spectra are also known as difference spectra.

Two different configurations can be used to measure FTIR spectra, the transmission and the attenuated total reflection. Both are shown in figure 5.24. In the ATR configu-

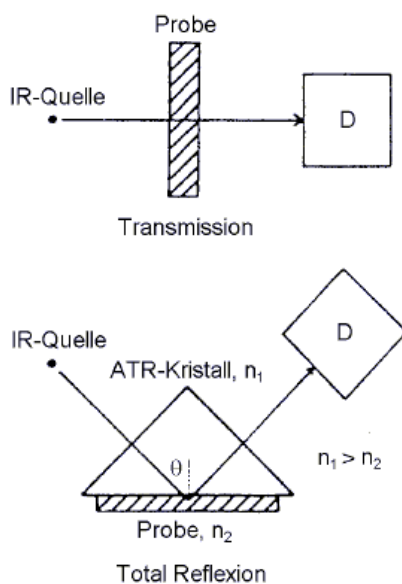


Figure 5.24: Transmission and ATR configuration.  $n_1$  and  $n_2$  are the refraction indices for the crystal and the sample, respectively.  $D$  denotes the detector. [12]

ration the sample is attached in a close distance to the ATR crystal which is diaphanous in the IR range. The incident angle of the IR beam  $\Theta$  has to be smaller than the critical angle for the total reflection in the ATR crystal. Thus the beam is totally reflected at the interface of the crystal and the sample. The IR radiation penetrates the sample material within a short distance at the interface and the sample material can absorb intensities at distinct frequencies. Thereby, the electrical field is attenuated exponentially with the penetration depth. The value  $d_p$  denotes the distance at which the intensity has declined to  $1/e$ -times of the field in the ATR crystal. This value is determined by:

$$d_p = \lambda_1 / \left( 2\pi \cdot \sqrt{(\sin^2 \Theta) - n_{2,1}^2} \right) = \lambda_{\text{vak}} / \left( 2\pi \cdot \sqrt{(n_1^2 \cdot \sin^2 \Theta) - n_2^2} \right) \quad (5.74)$$

where  $\lambda_1 = \lambda_{\text{vak}}/n_1$  denotes the wave length of the radiation inside the crystal,  $\Theta$  is the angle of incidence of the IR beam into the crystal,  $n_{2,1}$  is the ratio of refractive indices of the crystal  $n_1$  and of the sample  $n_2$ . Due to the fact that neither the wave length  $\lambda_1$  nor the refractive index of the sample can be adjusted the penetration depth can only be controlled by the refractive index of the crystal  $n_1$  or the angle of incidence  $\Theta$ . The angle of incidence is also determined by the geometry of the setup.  $n_1$  has to have a high value for the investigations of thin films with small penetration depths avoiding to measure the material beyond the film. The actual setup in the ATR configuration is shown in

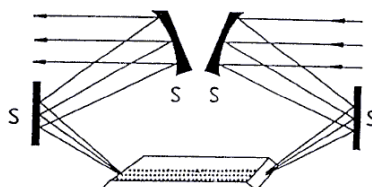


Figure 5.25: ATR crystal with multiple reflections.[12]

figure 5.25. Being reflected multiple times the sample will be penetrated at each reflection. For this reason even a very thin sample can provide a sufficient total absorption. If it is possible, the sample can be placed on both surfaces to increase the total absorption.

### 5.3.5 Surface Enhancement Effect

In some IR experiments only very small amounts of substances are provided. In these cases a modified technique based on the enhancement effect of infrared absorption by rough metallic surface (SEIRA) can be applied. The enhancement of optical processes by a factor  $10^2 - 10^{12}$  near rough surface of a metal (Au, Ag, Fe, etc.) is already known for twenty years, for both optical transitions in adsorbed molecules and the processes which do not depend on the presence of molecules on the metal surface. For example, these processes are SEIRA, surface-enhanced Raman scattering (SERS) or metal-enhanced fluorescence. In [20] the SEIRAS effect has been described as follows. The effect consists in an essential increase of the intensity of transition (for example, the effective cross-section increases by factor  $10^5 - 10^{12}$  for Raman scattering (RS) and  $10 - 10^4$  for IR absorption) or efficiency of the process near metal surface. The explanation of the effect is not simple and includes several mechanisms, namely: i) the increase of the electromagnetic field near a rough metal surface or island metal films, ii) the increase of the dipole transition moment of adsorbed molecules, etc. According to [90], the coefficient of the electric field enhancement is a function of the dielectric permeability of the metal.

The interpretation of the effect of enhancement is presented in [92] in a general form. It includes two possible ways: enhancement of the electromagnetic field due to interaction with local (surface) plasmon oscillations which emerge on the imperfections of the metal

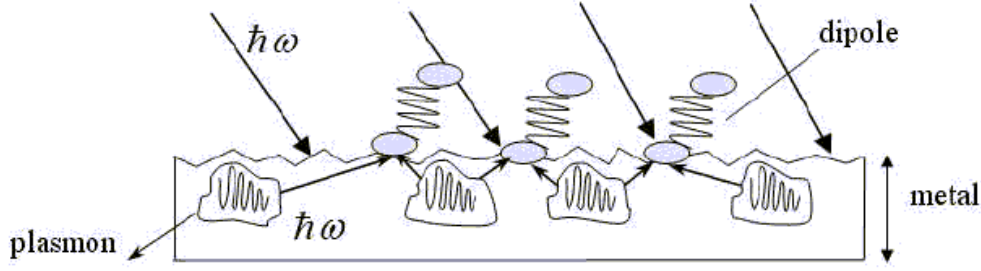


Figure 5.26: Scheme of the mechanism for the infrared absorption enhancement at the metal surface (SEIRA).[20]

surface, and specific increase of the dipole transition moments of the molecules adsorbed on the metal surface (see figure 5.26).

The theoretical interpretation of the effect is connected with the enhancement of the external electric field due to excitation of local (surface) plasmon vibrations at essential curvature of rough surface or on metal particles. In such systems, according to [91], the electric field in the point of spacer could be written as follows:

$$E(\mathbf{r}, t) = \exp(-i\omega t)[E_0(\omega) + E_1(\mathbf{r}, \omega)] \quad (5.75)$$

where  $\omega$  is the frequency and  $t$  is the time. The additional term  $E_1(\mathbf{r}, \omega)$  is connected with the excitation of local (surface) plasmon vibrations. The enhancement of the external field can be presented as:

$$E_\alpha(\mathbf{r}, \omega) = g_{\alpha\beta}(\mathbf{r}, \omega)E_{0\beta}(\omega) \quad (5.76)$$

where  $g_{\alpha\beta}(\mathbf{r}, \omega)$  is the enhancement coefficient. For matrix elements of the dipole transition moment for the transition between the states  $i$  (with energy  $\epsilon_i$ ) and  $f$  for the adsorbed molecule of nucleic acid, we have:

$$\langle f | d_\alpha(\mathbf{r}) | i \rangle = h_{\alpha\beta}^{(fi)} \langle f | d_{0,\beta} | i \rangle \quad (5.77)$$

where  $\langle f | d_0 | i \rangle$  is the matrix element of the dipole transition moment for an isolated molecule. According to the classical approximation, the matrix elements of the Hamiltonian describing the interaction of the adsorbed molecule with field are:

$$\langle f | H(\mathbf{r}, \omega) | i \rangle = - \langle f | d_\alpha(\mathbf{r}) | i \rangle E_\alpha(\mathbf{r}, \omega) = -h_{\alpha\beta}^{(fi)}(\mathbf{r})g_{\alpha,\gamma}(\mathbf{r}, \omega) \langle f | d_{0,\beta} | i \rangle E_{0,\gamma}(\omega) \quad (5.78)$$

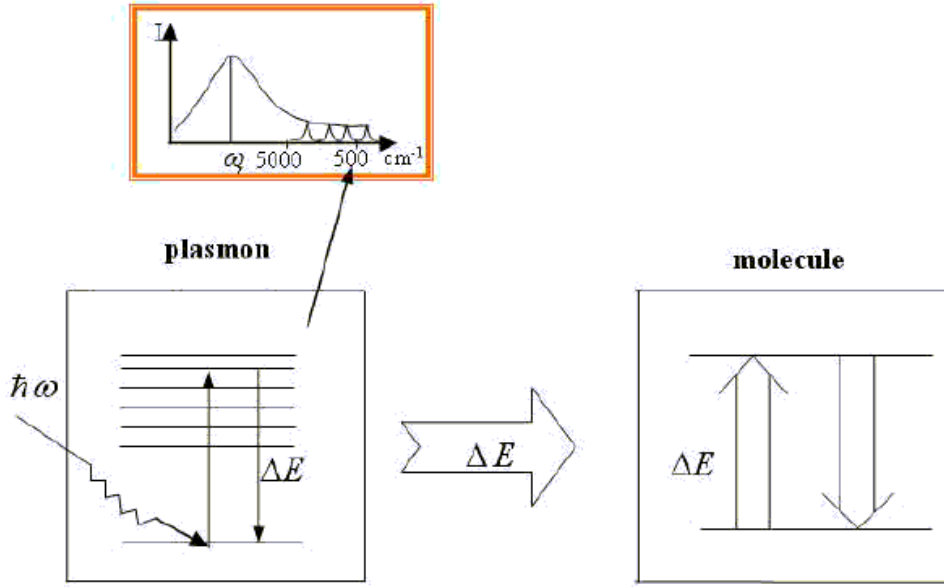


Figure 5.27: Energy scheme of the mechanism of the enhancement effect.[20]

Having performed substitution from equation 5.78 into the expression:

$$\omega_{fi}(r, \omega) = (2\pi/\hbar) |\langle f | H(r, \omega) | i \rangle|^2 \delta(\hbar\omega - \epsilon_f + \epsilon_i) \quad (5.79)$$

for the rate of the  $i \rightarrow f$  transition, multiplied the result by the energy  $\hbar\omega$  of absorbed quantum, and divided by the density of the incident energy flow  $cE_0^2/8\pi$  we obtain the expression for the effective cross-section of light absorbance by the adsorbed molecule:

$$\sigma_\alpha(r\omega) = 16\pi^2 \omega_{fi} / (cE_0^2) |\langle f | H(r, \omega) | i \rangle|^2 \delta[\hbar(\omega - \omega_{fi})] \sim \sigma_\alpha^{(0)} |g(r, \omega)|^2 |h(r)|^2 \quad (5.80)$$

where  $\sigma_\alpha^{(0)}$  is the cross-section for the case when metal is absent ( $d = d_0$ ,  $E = E_0$ ). The right hand part of equation 5.80 is the estimation of the cross-section by its order of magnitude.

The energy scheme of the mechanism of the enhancement effect is presented in figure 5.27. Under the conditions of IR experiments in [20], frequencies at the wing of the plasmon resonance for the golden substrate have been chosen, as it is shown in the insertion of figure 5.27. The energy is transferred from the photon to local plasmon oscillations. The plasmon oscillations have resonant character, and their frequency is determined by the form of the boundary. The surface charge that emerges on the roughnesses causes the

Coulomb returning force. The energy is transferred from plasmon vibrations to the adsorbed molecules, which causes the increased molecular absorbance [20]. For an extended explanation of this issue see literature [20][7].

### 5.3.6 Time-Resolved Surface Enhanced Infrared Absorption Spectroscopy (tr-SEIRAS)

**Rapid-Scan mode:** The rapid-scan mode is the general mode which is applied in order to record a FTIR spectrum. The movable mirror scans the interferogram positions successively. For this purpose scans are repeated and the signals of each scan are coadded. With this technique, time resolution can be applied to one single sample without repeating the experiment. Thereby, the time-resolving determinant is the time that is needed for one scan cycle. Usually, this time is in the range of some 50 ms. The scanning time can be varied by changing the spectral resolution.

**Step-Scan mode:** In general, the step-scan mode can be applied for time resolved or phase resolved spectroscopy. In the time resolved spectroscopy the response of the system to an external excitation is investigated as a function of time. However, in the phase resolved spectroscopy the phase of the system is compared with the phase of the periodic excitation as a function of time [150]. Here, we focus on the step-scan mode which is used to resolve the time domain.

With the step-scan mode a higher resolution in the time domain can be achieved than for the rapid-scan mode (see figure 5.28). In this case, the time which is needed for one single scan due to limitations of the mirror velocity e.g. does not determine the resolution. Only the electronic properties of the detector and the analog-to-digital-converter (ADC) determine the time resolution (ms-ns) [209].

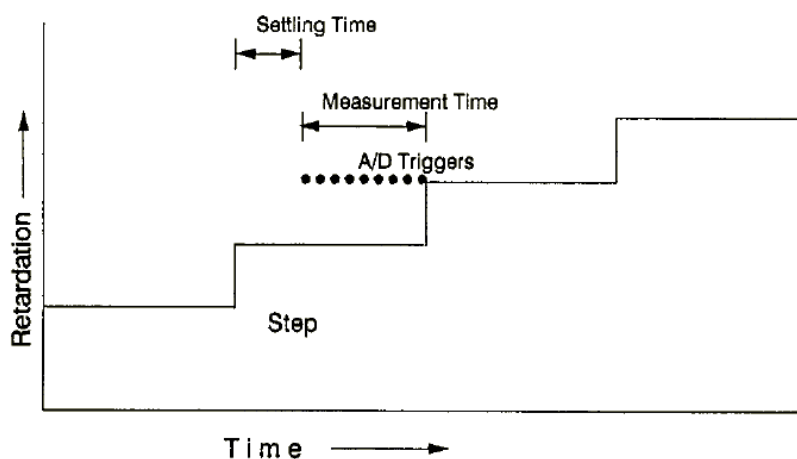


Figure 5.28: Scheme of the step-scanning mirror. [180]

The method bases on the periodicity of the experiment. It needs to be repeated multiple times and for this reason it is essential to achieve constant conditions. The

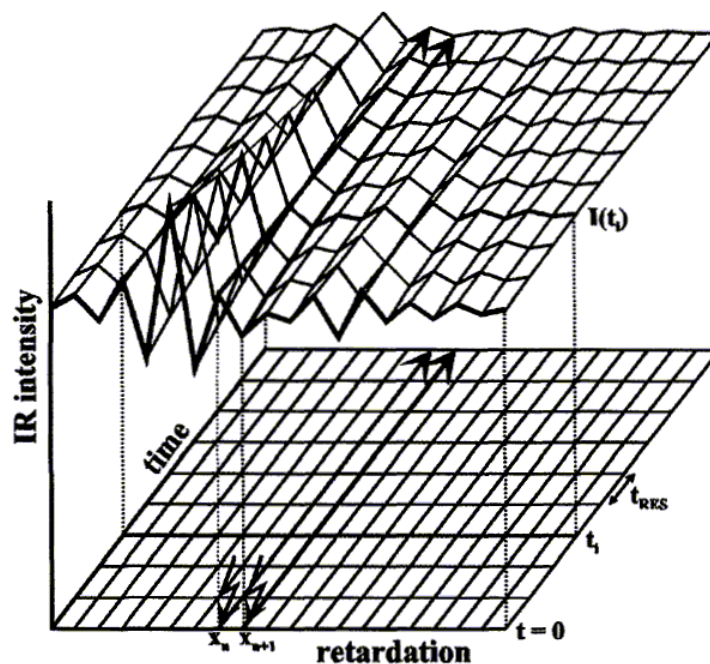


Figure 5.29: Step scan technique: the scanning mirror is kept at a sampling position  $x_n$  and the whole sequence of pulses is performed. The IR intensity is recorded for each time slide and predetermined number of pulses. Then the scanner steps to the next position  $x_{n+1}$  and procedure is repeated. After having measured the entire range of retardation (i.e. wavenumbers), the time-dependent spectra are reconstructed by the computer software in order to achieve the interferograms corresponding to each time slide  $I(t_i)$ . With the help of Fourier transformation the respective spectra can be obtained. The time resolution (i.e.  $t_{RES}$ ) is limited by the response time of the detector. [55]

spectrometer is therefore connected to the "exciting force" which is an applied potential to the sample in this work.

The movable mirror which scans the distance in the x-direction is kept constant at the interferogram position  $x_n$ . The experiment is then initiated by a trigger signal. The absorbance intensity at this particular interferogram position,  $x_n$ , is then recorded for each time slide. The scanner steps to the next interferogram position,  $x_{n+1}$  and the intensity response is again measured as a function of time (see figure 5.29). The step width is therefore determined by the choice of wave number resolution. In this way, the moving mirror of the interferometer stops at equidistant positions (optical retardations) and scans the interferogram positions. After having measured the entire range of retardation, the time-dependent spectra are reconstructed by the computer software in order to achieve the interferograms corresponding to each time slide  $I(t_i)$ . With the help of Fourier transformation the according spectra which characterize the time-dependent process can be obtained.

Due to the short detection times only low signals can be recorded. In this context, the experimenter can choose a number of coadditions determining the number of recorded scans. These scans are coadded and averaged in order to improve the SNR. With  $N$  coadditions the SRN improves by a factor of  $\sqrt{N}$ .

The resting time of the mirror also contains a delay time which is needed to bring the mirror into the position and to stabilize it. These values as well as the response time of the detector (some few nanoseconds) are essential for the quality of the time resolution. A deviation  $\Delta x$  of the position of the mirror from the specified value affects SNR [87]:

$$SNR \sim \Delta x^{-1} \quad (5.81)$$

The method is very sensitive to external perturbations, such as noise for example. For this reason the setup needs to be positioned on a stable, vibration-cushioned table. Furthermore, it is favourable to choose short measure times in order to avoid instability of the system. For further details the reader is referred to literature [180][55][87][81].

### 5.3.7 Combination of tr-SEIRAS and Electrochemical Excitation of CcO by means of Square Wave Potential Pulses

Periodically alternating potential pulses in the form of a square wave function are applied to CcO which is adsorbed on an electrode (see top part in figure 5.30). The time-resolved recording of FTIR spectra in step scan mode is triggered by the fast potential change at the start of each period and a set of spectra, one for each time slide is thus obtained (see left side of the middle part of figure 5.30). The spectrum of the first time slide is used as a reference, hence it is subtracted from the spectra of all other time slides thus yielding the difference spectra shown on the right side of the middle part of figure 5.30. Plotting the absorbance vs. time reflects the kinetics of the redox centers.

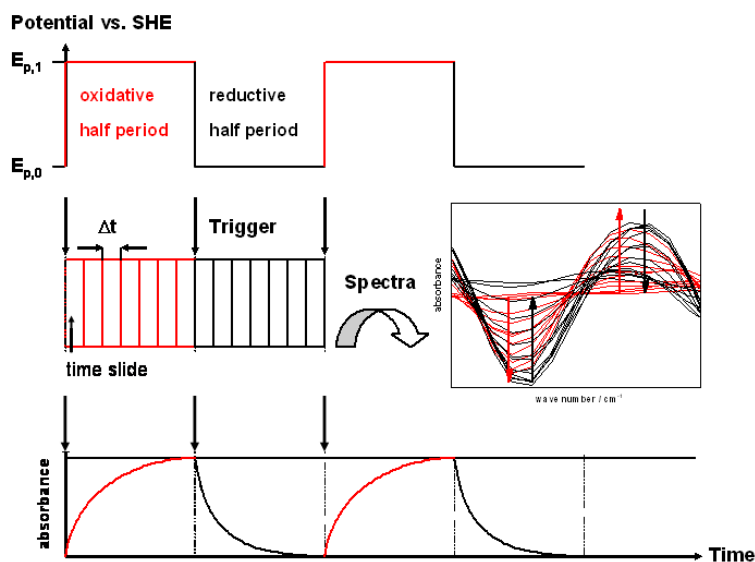


Figure 5.30: Principle of tr-SEIRAS: Periodically alternating potential pulses in the form of square wave functions (top part) . The time-resolved record of FTIR spectra is triggered with the fast potential change at the start of each period (middle part). The band intensities indicating the kinetics of the redox transition as a function of time, are then plotted vs. time (bottom part).

### 5.3.7.1 Analysis of the Redox Kinetics

As explained in the context of CVs, each change in applied potential  $E_p$  gives rise to a capacitive current which causes the effective potential relevant to the redox centers to deviate from  $E_p$ . This phenomenon can be described by the following equations:

$$dE/dt = [E_p(t) - E(t)]/\tau \quad (5.82)$$

where  $\tau = R_s C$  is the relaxation time and

$$E_p(t) = \begin{cases} E_{p,1} & (i_p - 1)/f_p < t \leq (i_p - 1/2)/f_p \\ E_{p,0} & (i_p - 1/2)/f_p < t \leq i_p/f_p \end{cases} \quad i_p = 1, 2, \dots \quad (5.83)$$

where  $E_{p,0}$  and  $E_{p,1}$  denote the reducing and the oxidizing potential, respectively (see figure 5.30), whereas  $f_p$  and  $i_p$  denote the frequency and the number of the pulses, respectively. In figure 5.31 an example of the deviation between the effective and applied potential is shown.

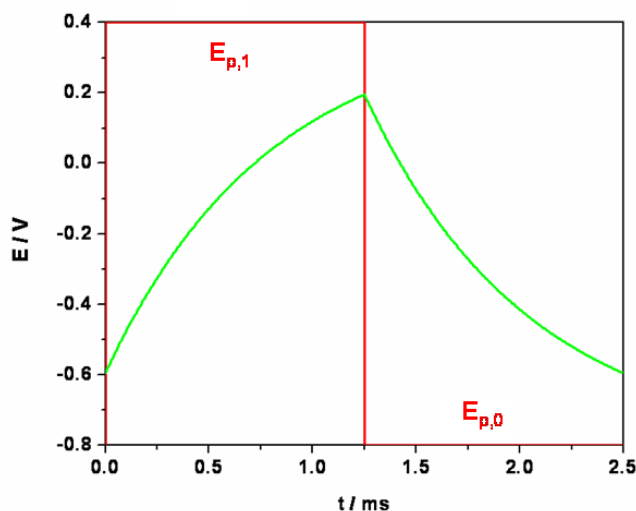


Figure 5.31: Externally applied (red) and effective potential (green) caused by the charging effect of the electrode at high frequencies (400 Hz in this case).

**Relation between absorbance and redox state of centers:** Considering Lambert-Beer's law the contributions of the redox states to the absorbance  $A_i$  at wavenumber  $\tilde{\nu}$  and time  $t$  for a band associated with the  $i^{\text{th}}$  center are proportional to the overall probabilities of the oxidized and the reduced state (see equation 5.38):



$$A_i(\tilde{\nu}, t) = A_{i,\text{ox}}(\tilde{\nu})p_{i,\text{ox}}(t) + A_{i,\text{red}}(\tilde{\nu})p_{i,\text{red}}(t) = A_{i,\text{ox}}(\tilde{\nu}) + \Delta A_i(\tilde{\nu})p_{i,\text{red}}(t), \quad (5.84)$$

$$\Delta A_{i,\text{red-ox}}(\tilde{\nu}) = A_{i,\text{red}}(\tilde{\nu}) - A_{i,\text{ox}}(\tilde{\nu}) \quad (5.85)$$

$A_{i,\text{ox}}(\tilde{\nu})$  and  $A_{i,\text{red}}(\tilde{\nu})$  refer to the oxidized and reduced state, respectively, and are products of the effective optical pathlength, the surface concentration, and the respective molar extinction coefficient. With  $A_i(\tilde{\nu}, 0)$  denoting the absorbance of the reference spectrum taken at  $t = 0$  the change of absorbance in time is given by (see bottom part of figure 5.30)

$$\Delta A_i(\tilde{\nu}, t) = \Delta A_{i,\text{red-ox}}(\tilde{\nu}) [p_{i,\text{red}}(t) - p_{i,\text{red}}(0)] + A_{i0}(\tilde{\nu}) \quad (5.86)$$

The term  $A_{i0}(\tilde{\nu})$  denotes a correction term which accounts for the experimental error of  $A_i(\tilde{\nu}, 0)$ .

### 5.3.8 Model Simulation and Parameter Fitting

The full mathematical description of the model presented in section 5.2.4 yields a set of non-linear differential equations for the probabilities  $p_k$ , which have to be integrated numerically. A very convenient alternative is to transform the model into an electrical network representation and to make use of the network simulation program Spice for integration [117]. Spice had been introduced earlier to model bioelectrochemical processes across membranes [187]. Its advantage is not only that no differential equations have to be formulated, but also that it reflects the topology of the kinetic scheme, and in particular its modular design. New elements can be defined (subcircuits in Spice terminology) which are programmed for a particular process, e.g. the flow of electron uptake or exchange. These elements can be repeatedly used and plugged in anywhere in the network. This is of particular benefit for complex systems such as multi-electron transfer systems (see figure 5.14). Spice is in the public domain and available for various computer systems. We routinely use MacSpice (version 3f5) on Mac computers with OS X (versions 10.4.x).

Parameter fitting was performed with the program MODFIT [113]. This code is based on the Marquardt-Levenberg algorithm and does not require analytical expressions for the partial derivatives with respect to the parameters but calculates them numerically. It is therefore well suited to cope with Spice simulations and was implemented in the control structure of the Spice input files. For further information on this routine and details of the MacSpice program contact D. Walz (dieter.walz@unibas.ch).

Simulation and parameter fitting was kindly done by D. Walz. <sup>2</sup>

---

<sup>2</sup>Text has been composed by D. Walz

---

## 6 Results and Discussion

### 6.1 Oriented Immobilization of Cytochrome c Oxidase

A new linker molecule, the Dithiobis (nitriloacetic acid butylamidyl propionate) (short: DTNTA) has recently been synthesized from DTSP and NTA to tether CcO to a metal surface. A self-assembled monolayer from a mixture of dissolved dithiopropionic acid (DTP) and DTNTA was formed on the metal electrode. Since the enzymes are only tethered to the chelator molecules (DTNTA), the concentration of DTNTA determines the surface concentration of proteins on the electrode. The first part of this thesis concerns an electrochemical investigation in which the optimum ratio of both molecule types shall be found. Electrochemical impedance spectroscopy (EIS) and cyclic voltammetry (CV) were used in combination with surface plasmon resonance (SPR). To characterize the layers the following sections present the results employing each method for the system at different mole fractions  $x$ , where

$$x = N_{DTNTA} / (N_{DTNTA} + N_{DTP}) \quad (6.1)$$

and  $N$  denotes the mole number. For a detailed description of the synthesis of chelator molecules which was published by our group the reader is referred to literature [131].

### 6.1.1 Electrochemical Impedance Spectroscopy at Different Surface Concentrations

The quality of membrane formation was controlled by electrochemical impedance spectroscopy (EIS). EIS data were recorded in the range of 0.1 Hz - 2 mHz with an excitation amplitude of 10 mV and a bias potential of 0 V against an  $\text{Ag}|\text{AgCl}, \text{KCl}_{\text{sat}}$  reference electrode. Exemplary for the different concentrations of chelator molecules we discuss the data set obtained from EIS for  $x = 0.2$  only. The absolute values obtained from EIS measured at different concentrations are discussed afterwards. The Bode and the Admittance Plot for  $x = 0.2$  are shown in figures 6.1 (A) and (B) for the system after the enzymes were adsorbed onto the surface (solid circles) and after membrane formation (solid triangles).

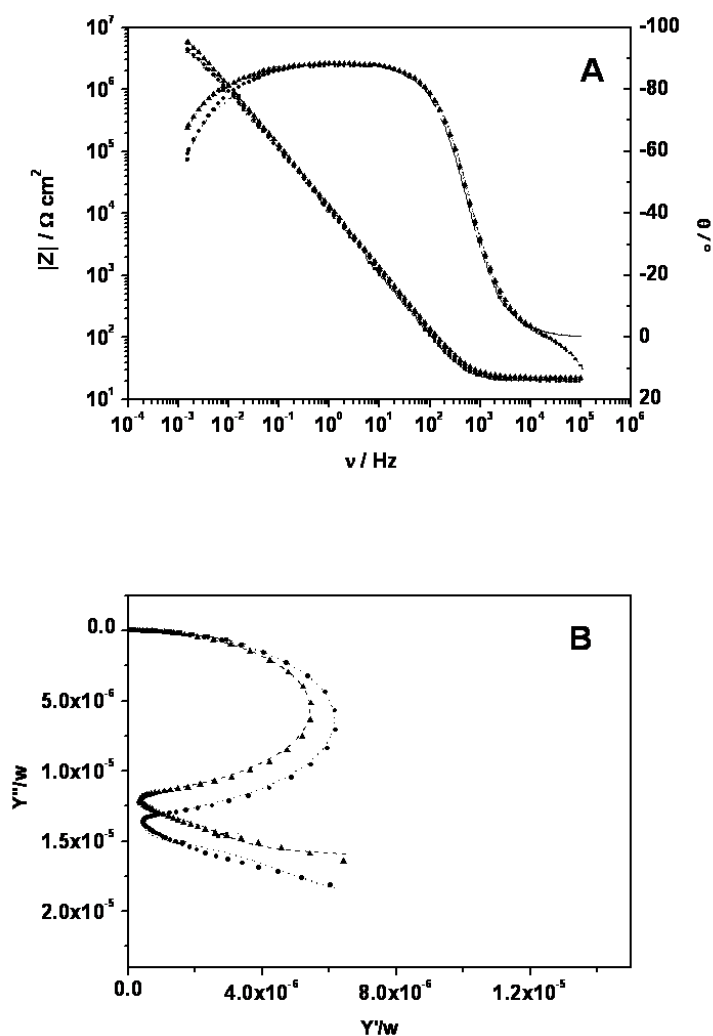


Figure 6.1: Bode (A) and Admittance plot (B) of the ptBLM at a mole fraction of 0.2 after (solid circles) protein adsorption and after membrane formation (solid triangles). The curves represent the result of fitting the equivalent circuit.

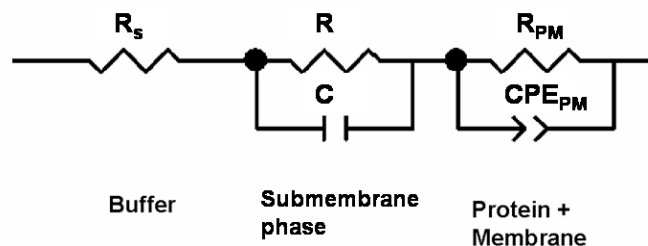


Figure 6.2: Equivalent circuit is fitted to the EIS data.

The data were analyzed by means of an equivalent circuit which is shown in figure 6.2. In this model it is assumed that the buffer solution is characterized by an ohmic resistor  $R_s$ , whereas the submembrane phase can be described by a RC element. The resistor  $R$  represents the resistor of the buffer and the linking molecules underneath the membrane phase. The capacitor  $C$  represents the diffuse double layer in the submembrane phase which occurs for a charged electrode surface. The properties of the protein/membrane phase are here characterized by a parallel circuit of a constant phase element  $CPE_{PM}$  and an ohmic resistor  $R_{PM}$ . As for every dielectric layer, the capacitor must be considered in parallel with the membrane resistor. However, in this case it is appropriate to apply a constant phase element instead of a pure capacitor because of inhomogeneity that seem to occur in the membrane/protein phase. In table 3 the corresponding fit parameters are presented. The capacitance decreases from  $22.4$  to  $14.9 \mu\text{F cm}^{-2}$  when the adsorption of the enzymes and the membrane formation takes place. The proteins with a dielectric constant  $\epsilon \approx 20$  and the lipid molecules with  $\epsilon \approx 2.2$  replace the water molecules with  $\epsilon \approx 80$  near the electrode surface [131]. Since  $C \propto \epsilon$ , the capacitance decreases during this process. At the same time the resistance increases from  $6.8$  to  $18.7 \text{ M}\Omega \text{ cm}^2$ . The increase and the high resistance indicate a good sealing property of the membrane. A pure lipid bilayer membrane would have a capacitance as low as  $0.5 \mu\text{F cm}^{-2}$  and a resistance of some  $\text{M}\Omega \text{ cm}^2$  [131]. However the pure lipid bilayer membrane is hardly comparable to the ptBLM. The membrane/protein phase of the ptBLM consists of a high amount of proteins which leads to much higher capacitances. However the decrease in capacitance and the increase in resistance values are a good indication of the formation of the membrane.

The values of capacitance and resistance for the systems at mole fractions 0.1, 0.2 and 0.3 before (shaded bars) and after membrane formation (empty bars) are illustrated in figures 6.3 (a) and (b). From the change in capacitance and resistance qualitative information about the surface concentration of proteins can be obtained (see figures

element	protein phase without membrane	protein phase with membrane
$CPE-T_{PM} / \mu\text{F cm}^{-2}$	$18.8 \pm 2.0\%$	$14.9 \pm 1.7\%$
$CPE-P_{PM}$	$0.97 \pm 1.4\%$	$0.98 \pm 0.1\%$
$R_{PM}/\text{M}\Omega \text{ cm}^2$	$10.0 \pm 3.7\%$	$18.7 \pm 5.1\%$

Table 3: Fit parameters: capacitance and resistance of the system at a mole fraction of 0.2 before and after membrane formation.

6.3 (c) and (d)). The change in capacitance and resistance at the mole fraction of 0.1 is high compared to the higher mole fractions. The reason for this is a relatively low surface concentration of proteins which allows many lipids to be inserted in between the protein molecules. At mole fractions 0.2 and 0.3 the changes in capacitance and

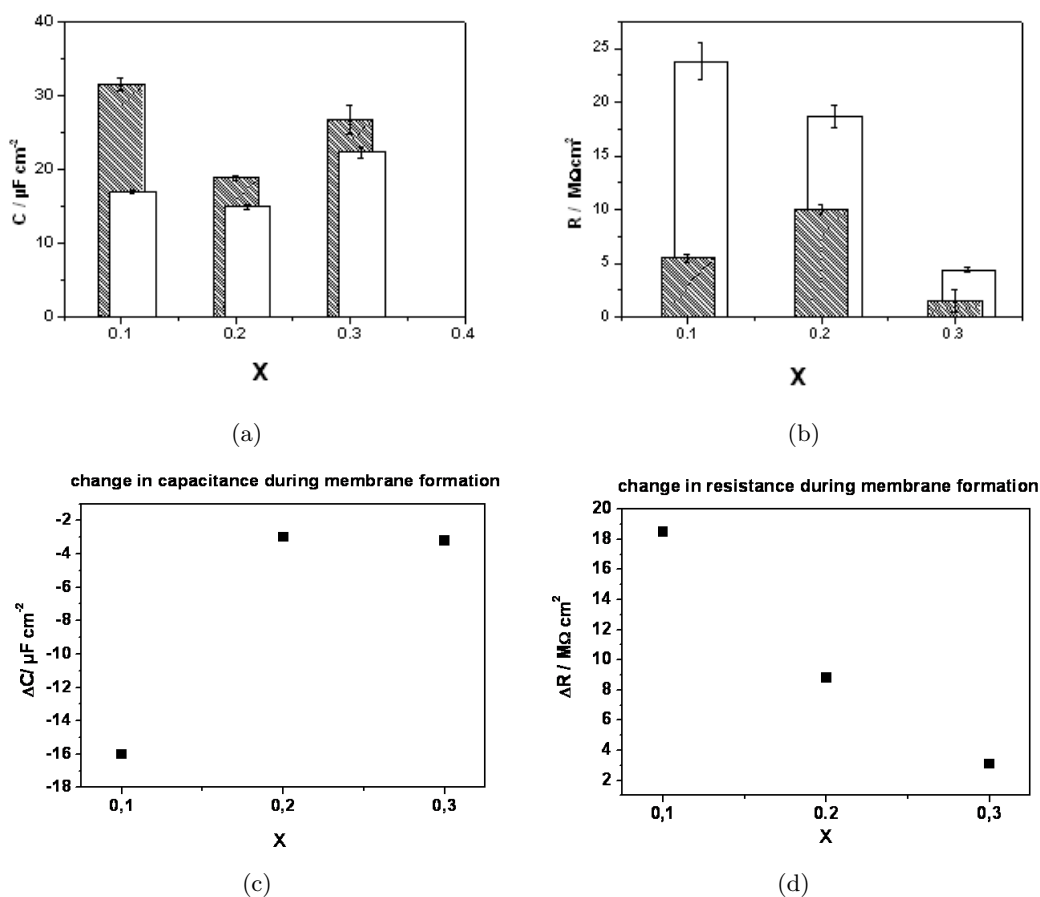


Figure 6.3: Capacitances (a) and resistances (b) of the system at mole fractions of 0.1, 0.2 and 0.3 before (shaded bar) and after membrane formation (empty bar). Corresponding change in capacitance (c) and resistance (d) at mole fractions of 0.1, 0.2 and 0.3 during the formation of the membrane.

resistance are less significant than for the lowest concentration. This is an evidence for a higher protein packing density. Particularly at  $x = 0.3$  the small changes indicate that the membrane/protein phase consists to a large part of proteins.

### 6.1.2 Cyclic Voltammetry of CcO at Different Surface Concentrations

CVs of CcO under aerobic conditions were first measured in order to evaluate the turnover efficiency at different surface concentrations (see figure 6.4). Electrons being transferred to the redox centers of the protein are consumed in the oxygen reduction (see section 3 and particularly 3.4 for details). In figure 6.4 CVs of CcO are illustrated at different mole fractions,  $x$ , ranging between 0.1 and 0.4. The CVs feature two peaks occurring at approximately -0.2 and -0.65 V. They were attributed to the repeated electron and proton transfer, respectively [133]. The current density which is plotted against the mole fraction in the inset of figure 6.4 shows a maximum value for  $x = 0.2$ . We conclude from this result that the optimum packing density might be achieved with a mole fraction of  $x = 0.2$ .

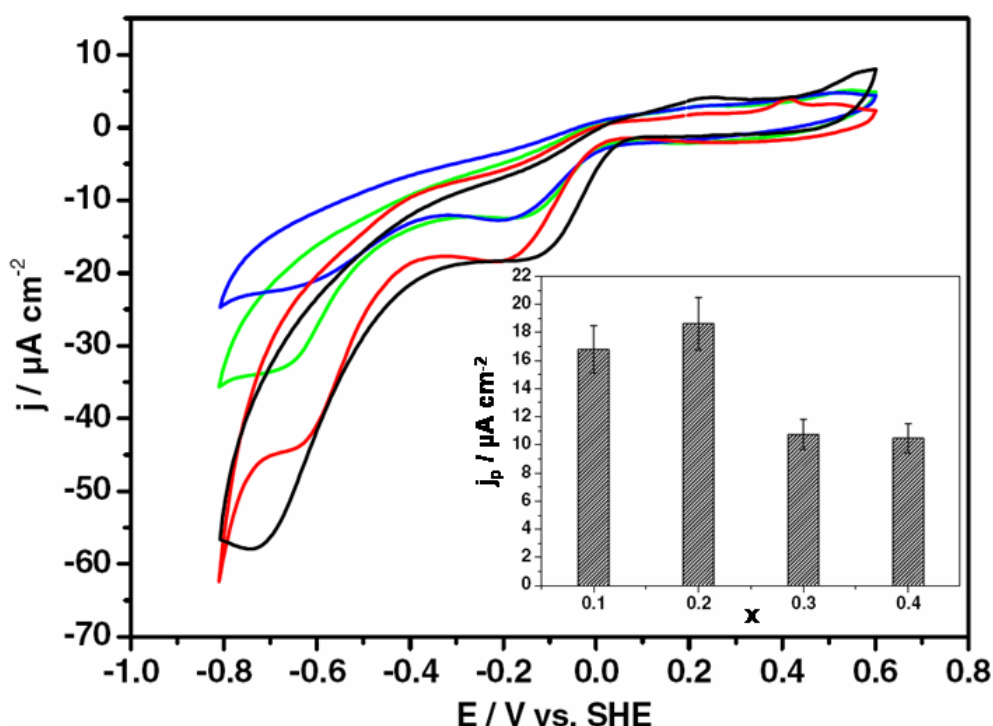


Figure 6.4: CVs of CcO immobilized on an ex-situ functionalized ultraflat gold electrode at different mole fractions,  $x$ , 0.1 (blue), 0.2 (black), 0.3 (red), 0.4 (green) under aerobic and otherwise equal conditions. The inset shows the peak current densities for  $x = 0.1, 0.2, 0.3, 0.4$ .

In order to verify this result, the same samples at mole fractions of 0.1, 0.2 and 0.3 have been measured by means of CV in the absence of oxygen, thus eliminating the proton transfer and the oxygen reduction and focussing on the ET (see figure 6.5). Scan rates between 0.05 and 0.8  $V s^{-1}$  have been employed. At a mole fraction of 0.2 (see figure 6.5 (B)) a single peak and its counterpeak appear at approximately -0.3 and -0.2 V vs. SHE in the reductive and oxidative branch of the CVs, respectively. This confirms the results obtained previously [133]. The CVs according to the mole fractions  $x = 0.1$  and  $x = 0.3$  (see figure 6.5 (A) and (C), respectively) contain only a distinct cathodic peak, whereas the anodic peak is very weak. These peaks have been assigned before to the ET to the

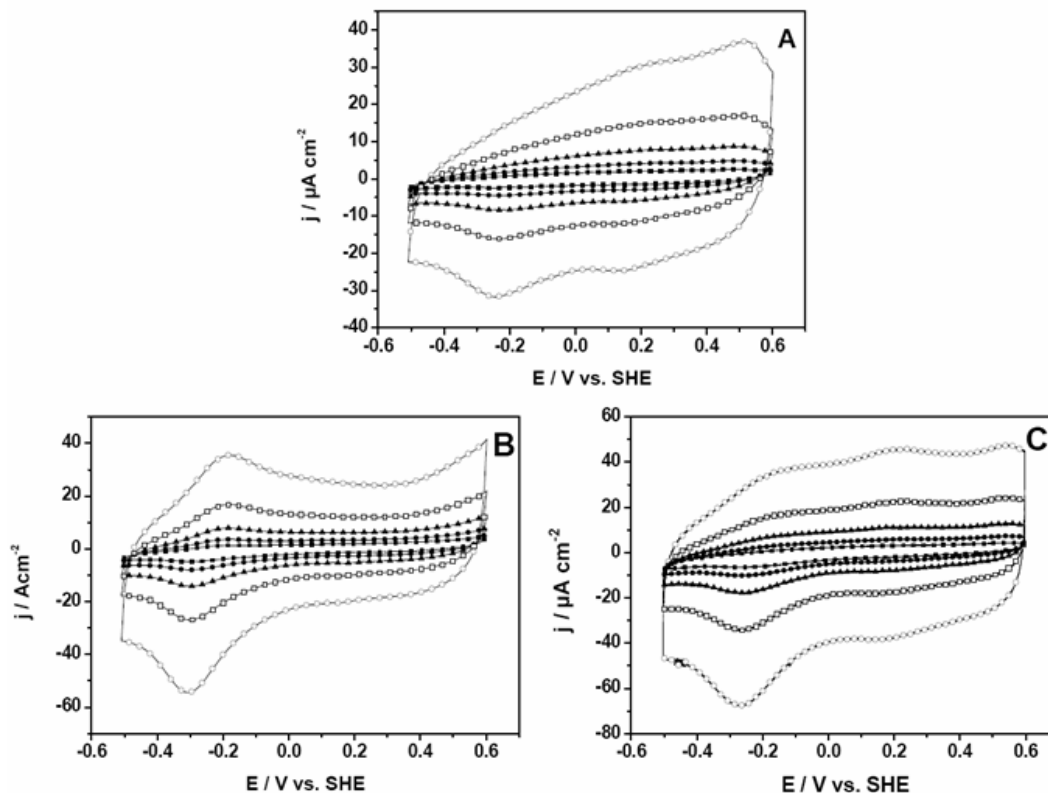


Figure 6.5: CVs measured in the absence of oxygen thus excluding the proton transfer and concomitant oxygen reduction at mole fractions 0.1 (A), 0.2 (B) and 0.3 (C). This study focusses on the ET to CcO. The scans have been measured at scan rates of 0.05 (solid squares), 0.1 (solid circles), 0.2 (solid triangles), 0.4 (open squares) and 0.8  $\text{Vs}^{-1}$  (open circles).

four redox centers,  $\text{Cu}_A$ , heme a, heme  $a_3$  and  $\text{Cu}_B$  applying spectroelectrochemistry, i.e. electrochemistry in combination with Raman and IR spectroscopy [133][132]. Analysis of CVs taken under anaerobic conditions (see figure 6.5 A,B and C) yields information about the surface concentrations, midpoint potentials and kinetic constants. The surface concentration  $\Gamma$  can be calculated using equation 5.32. The values found for  $\Gamma$  at mole fractions  $x = 0.1$  and particularly  $x = 0.2$  are comparable to the theoretical surface concentration  $6 \text{ pmol cm}^{-2}$  (see table 4) which was calculated from the dimensions of the CcO molecule for a monolayer of the closely packed proteins on the air/water interface of a Langmuir trough. However, the  $\Gamma$  value that was found for  $x = 0.3$  is much too high. This could be explained by an overpacking of protein molecules, e.g. a second adsorbed layer, which impairs the function of CcO (see figure 6.4).

Mole fraction $x$	0.1	0.2	0.3
$\bar{\Gamma} / \text{pmol cm}^{-2}$	$5.2 \pm 0.9$	$7.2 \pm 3.9$	$16.7 \pm 3.3$

Table 4: Averaged protein surface concentrations found for mole fractions  $x = 0.1, 0.2, 0.3$ . Values for  $x = 0.2$  were calculated with oxidative and reductive branch, whereas those for  $x = 0.1$  and  $0.3$  apply only to the reductive branch.

### 6.1.3 Surface Plasmon Resonance

The absorption kinetics of a sample with  $x = 0.2$  has been traced by surface plasmon resonance (SPR) (see figure 6.6). After the relevant preparation steps, SPR angle scans have been performed (see inset of figure 6.6). A first angle scan was recorded (see figure

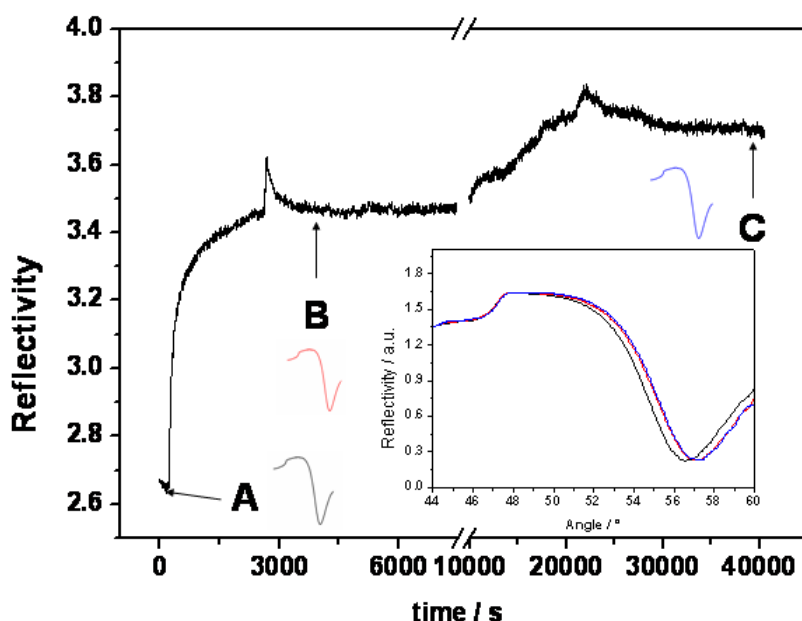


Figure 6.6: Kinetic SPR trace of the adsorption (A-B) of proteins and membrane formation (C) for  $x = 0.2$  and a fixed angle of  $54.7^\circ$ . The Inset shows the SPR angle scans that have been performed before (A, black) and after protein adsorption (B, red) and after membrane formation (C, blue).

6.6, position A and inset (black)) before starting the trace with the functionalized gold surface. The cell was filled with a detergent-containing buffer solution which was also used as a stabilizing medium for the proteins. For every measurement the same buffer solution has been used in order to avoid changes in the refractive index of the solution. For the reflectivity trace a fixed angle of  $54.7^\circ$  has been chosen. It is important to choose a fixed angle at which the change in reflectivity of the angle scan is linear, so that the change in reflectivity during the kinetic trace can indeed be considered as linear. After having started to trace the absorption kinetics, the proteins were injected into



the cell. A significant change in the reflectivity indicates the adsorption of the enzyme to the functionalized surface. After approximately 40 min, the adsorption is completed and the excess of enzymes can be purged out of the cell. A second SPR angle scan has been performed after the adsorption of protein molecules (see figure 6.6, position B and inset (red)). Lipid micelles in DDM were added to the system together with Biobeads. The reflectivity rises continuously until it reaches saturation. This process takes approximately 12 hours. The existence of a peak in reflectivity which arises during this event was observed before and can be described by the deposition of lipid vesicles onto the protein layer. As soon as the lipid membrane is formed, the reflectivity slightly declines again. The last SPR angle scan has been performed after the membrane formation (see figure 6.6, position C and inset (blue)). The thickness of each layer could be obtained by fitting the angle scans. In table 5 the fit parameters are presented. We obtain a thickness of 2.3 nm for the layer of linker molecules. This value is in good agreement with the theoretical length of such molecules. The thickness corresponding to the protein layer is found to be 9.7 nm. From structure analysis it is known that the height of CcO is 9.5 nm between cytoplasmic surface and C-terminus of the SU II [116] (see section 3.3). The layer thickness of the lipid bilayer was found to be 2.1 nm which is well in the range of earlier findings. Cell membranes for example were found to have a thickness of about 3.3 nm [45].

layer	thickness / nm
submembrane (DTNTA/DTP)	$2.3 \pm 0.5$
CcO	$9.7 \pm 0.5$
lipid bilayer	$2.1 \pm 0.5$

Table 5: Thickness of layers in the ptBLM determined by SPR.

#### 6.1.4 Summary and Conclusion

Data obtained from EIS could be used to characterize the electric properties of the ptBLM for  $x = 0.1$ ,  $x = 0.2$ , and  $x = 0.3$  (see equation 6.1). An equivalent circuit describing the layers was applied to fit the data. For each surface concentration of DTNTA the impedance spectra indicate the adsorption of proteins onto the gold surface and the formation of a membrane. However, the spectra for  $x = 0.1$  and  $x = 0.3$  indicate a low and a very high surface concentration of CcO, respectively. The mole fraction of  $x = 0.2$  was found to be the optimum value with respect to adsorption of a sufficient amount of enzymes and the formation of a stable membrane.

Cyclic voltammetry of CcO under aerobic conditions at different mole fractions yields information about the catalytic activity of the enzyme. CcO was found to be most active at  $x = 0.2$ . Furthermore, CVs obtained from CcO under anaerobic conditions indicate that the mole fraction  $x = 0.2$  is most suitable for the electron transfer. Only in this particular case the CVs show similar peaks in the reductive as well as oxidative branch which indicates a unimpaired functionality of the enzyme. Surface concentrations  $\Gamma$  for each mole fraction could be obtained from these data. The  $\Gamma$ -value for  $x = 0.2$  is compatible with the formation of a densely packed protein layer.

The adsorption kinetics, which was traced by surface plasmon resonance, could verify

the adsorption of enzymes and the membrane formation. The data obtained for  $x = 0.2$  yielded values which are in line with known values for the thicknesses for each layers in the ptBLM.

From these results we can conclude that the optimum concentration can be obtained using a mole fraction of  $x = 0.2$ . For each sample, which was used in the investigations presented in the following sections, we applied this mole fraction and a protein concentration of 10 nmolar in the solution used in the adsorption step.

## 6.2 Activation of CcO

CVs were obtained for CcO under anaerobic conditions (see figure 6.7). Peaks occur in the range 0.2 to 0.6 V according to known midpoint potentials of the redox centers. The same measurement was also done with CcO immobilized in the reverse orientation with the his-tag attached to SU I. This served as a control measurement. In this particular case the peaks were absent (figure 6.8). From this finding it can be concluded that ET from the electrode to the protein occurs only with CcO oriented as shown in figure 5.12 with the his-tag attached to SU II. When we changed from anaerobic to aerobic conditions, the enzyme started to work under turnover conditions (see figure 6.9 (a)). Two peaks

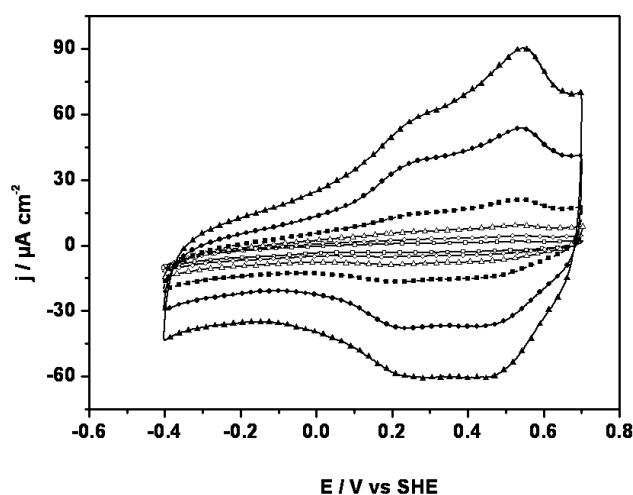


Figure 6.7: Cyclic voltammograms of CcO immobilized in a ptBLM via his-tag on subunit II under anaerobic conditions before activation, scan rates  $/(V s^{-1})$  0.05 (open squares), 0.1 (open circles), 0.2 (open triangles), 0.4 (solid squares), 0.8 (solid circles), 1 (solid triangles) taken at room temperature.

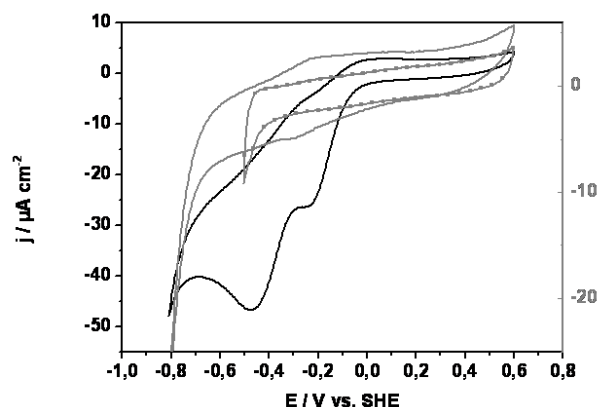
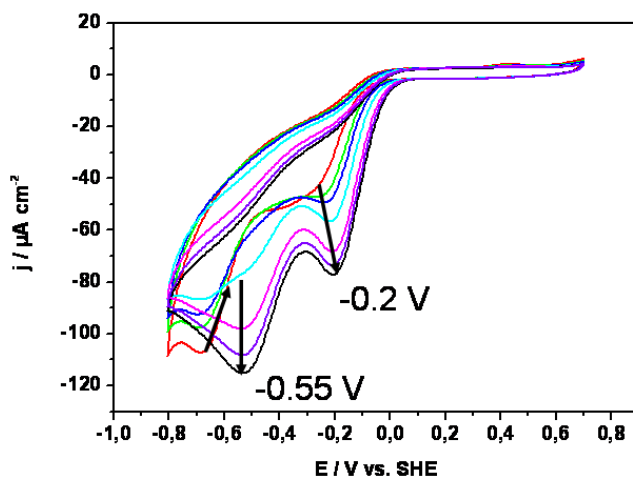
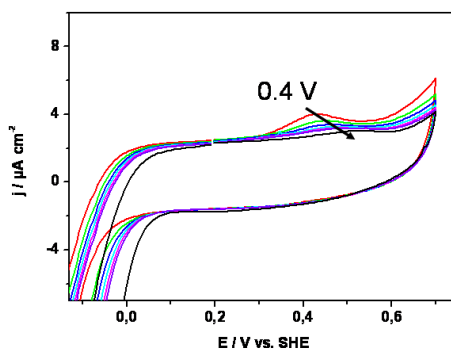


Figure 6.8: CVs of CcO on TSG immobilized with the His-tag attached to subunit II, under anaerobic (grey, right hand y-axis) and aerobic (black, left hand y-axis) conditions, both in the activated state measured at scan rate 50 mV/s. CV of CcO immobilized with the his-tag attached to subunit I (grey line and grey squares, right hand y-axis).

occurred in the negative potential range which were slightly shifted to more positive potentials in successive scans. Eventually, after a certain number of scans (approx. 20-40 scans), peak potentials under steady state conditions of -0.2 V and -0.55 V were reached. At the same time the peaks that existed before under anaerobic conditions in the range 0.2 to 0.6 V declined in successive scans (see figure 6.9 (b)). The peaks at -0.2 and -0.6 V



(a)



(b)

Figure 6.9: CVs of CcO taken under aerobic conditions at a scan rate of  $0.05 \text{ V s}^{-1}$  and at room temperature. The 1<sup>st</sup> (red), 5<sup>th</sup> (green), 10<sup>th</sup> (dark blue), 15<sup>th</sup> (light blue), 20<sup>th</sup> (pink), 25<sup>th</sup> (purple), 30<sup>th</sup> (black) scan is displayed demonstrating the shift of the electron and proton peaks from more negative values to -0.2 V and -0.55 V, respectively (a). The peaks at  $\approx 0.4 \text{ V}$  which occurred under anaerobic conditions for non-activated CcO vanish with successive scans (b).

were previously attributed to the repeated electron and proton transfer, characterized by the amplified current density [133]. If CVs were measured with buffer solutions at room temperature, one air saturated and the other saturated with pure oxygen, the peaks that were assigned to the electron and proton transfer are enhanced tremendously if the buffer solution is saturated with oxygen (see figure 6.10). The catalytic turnover of the enzyme is amplified when providing a high concentration of oxygen. Upon returning to anaerobic conditions, the peak attributed to the electron transfer persisted whereas the proton transfer peak vanished as expected [133] (see figure 6.11). Interestingly, the peak

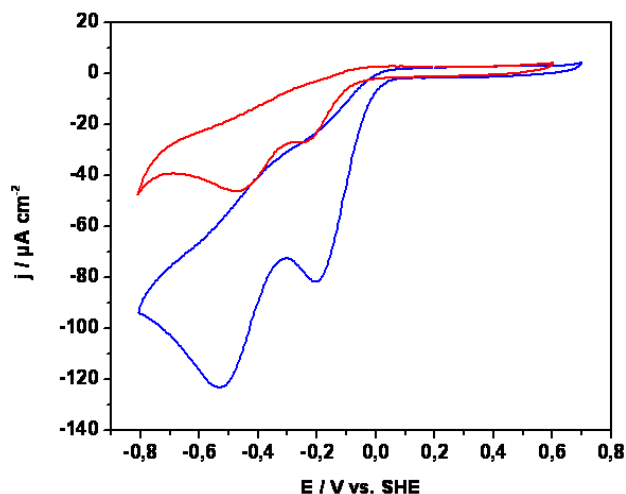


Figure 6.10: CVs of activated CcO under aerobic conditions at room temperature using a buffer solution which is not flushed (red) or flushed with oxygen (blue) taken at a scan rate of  $0.05 \text{ Vs}^{-1}$ . The peak currents that are attributed to the electron and the proton transfer are enhanced with an increase of substrate  $\text{O}_2$ .

for the electron transfer is shifted by more than 0.4 V into the negative direction vs. known midpoint potentials. In figure 6.12 the CVs of non-activated (light blue, brown) and activated (dark blue, red) CcO under aerobic (light blue, dark blue) and anaerobic (brown, red) at scan rates of  $0.05 \text{ Vs}^{-1}$  are displayed together for comparison.

### 6.2.1 Summary and Conclusion

We concluded from these results that the enzyme undergoes a successive transition from a non-activated (see figure 6.7) to an activated conformational state (see figure 6.11). This process is initiated while the enzyme passes a number of redox cycles under aerobic conditions (see figure 6.9 (a) and (b)). This is equivalent to the transition between the resting to the pulsed state which was found for CcO reconstituted in liposomes and subjected to oxygen pulses [47][104].

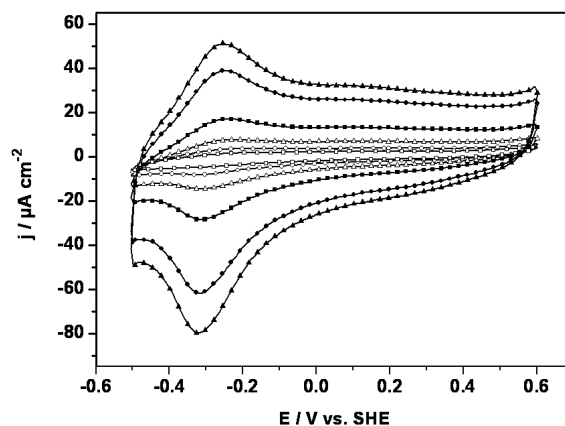


Figure 6.11: CVs taken under anaerobic conditions after activation, scan rates  $/(V s^{-1})$  0.05 (open squares), 0.1 (open circles), 0.2 (open triangles), 0.4 (solid squares), 0.8 (solid circles), and 1 (solid triangles) taken at room temperature.

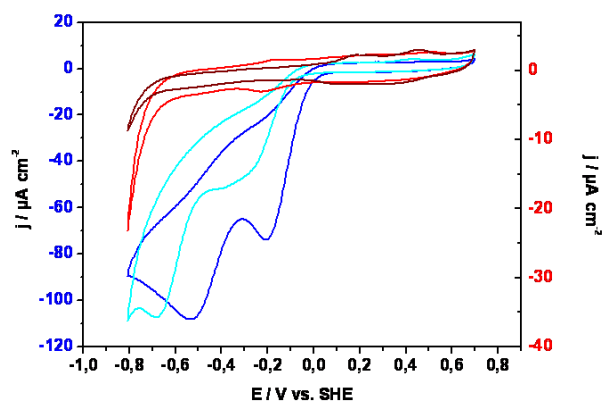


Figure 6.12: Comparison of CVs of activated (red, dark blue) and non-activated (brown, light blue) CcO under aerobic (light blue, dark blue) and anaerobic (brown, red) conditions taken at a scan rate of  $0.05 V s^{-1}$  and at room temperature. The scans taken under aerobic conditions refer to the left scale (blue) and the scans taken under anaerobic conditions refer to the right scale (red). The peak at approximately  $-0.2 V$  which was attributed to the ET in the case of activated CcO under aerobic conditions (blue) persists if changing to anaerobic conditions (red).

### 6.3 Analysis of Fast Scan Cyclic Voltammograms of CcO using multistep-ET models

Since the trumpet plot used by others for the analysis of ET to a single redox center is inappropriate for the analysis of a multi-center protein, the models described in section 5.2.4 were designed. Both, the sequential and the independent ET model were used to simulate CVs which were fitted to the baseline-corrected CVs by adjustment of parameters (see figures 6.7 and 6.11, where the original CVs without baseline-correction are shown). In the case of multi-redox centers the peak separation  $\Delta E_{ps}$  is defined as

$$\Delta E_{ps} = (E_{p,ox,i} - E_{p,red,i})/2 \quad (6.2)$$

where  $E_{p,ox,i}$  and  $E_{p,red,i}$  denote the peak potentials of the  $i^{\text{th}}$  center in the oxidative and reductive branch, respectively. Since current densities increase proportionally to  $\nu$   $\nu$ -normalized CVs were used when fitting parameter values which causes all CVs to be about equally weighted. The redox potentials  $E_{o,i}$  and the peak separation  $\Delta E_{ps}$  were first obtained by means of fitting these parameters to the reductive and the oxidative branches at the lowest scan rate,  $0.05 \text{ V s}^{-1}$ , making use of the equilibrated ET model. These parameter values were used as initial values for the fitting of the parameters at higher scan rates.

#### 6.3.1 Activated CcO

Since the simulations can only cope with one  $\Gamma$  for all scan rates it has to be checked whether this also holds for the experimental data. To this end  $\Gamma$ -values for both branches and all  $\nu$ 's were calculated according to equation 5.32. The results listed in table 6 show higher values for the reductive than for the oxidative branch and some variations with  $|\nu|$ . Hence the factor

$ \nu  / \text{V s}^{-1}$	$\Gamma_{\text{red}} / \text{pmol cm}^{-2}$	$\Gamma_{\text{ox}} / \text{pmol cm}^{-2}$	$f_{p,\text{red}}$	$f_{p,\text{ox}}$
0.05	8.468	4.849	1.411	0.808
0.1	7.616	5.438	1.269	0.906
0.2	8.698	5.337	1.450	0.890
0.4	7.544	5.719	1.257	0.953
0.8	6.694	5.243	1.116	0.874
1	8.366	5.210	1.394	0.868
2	10.42	6.808	1.737	1.135
4	10.37	5.222	1.728	0.870
8	9.780	4.210	1.630	0.702

Table 6: Surface coverages and scaling factors  $f_p$  for activated CcO at different scan rates with  $\Gamma_0 = 6 \text{ pmol cm}^{-2}$ .

Model $ \nu  / \text{V s}^{-1}$ branch	Equ. ET 0.05 red & ox	Sequ. ET 0.05-8 red & ox	Sequ. ET 0.05-8 red & ox	Ind. ET 0.05-8 red	Ind. ET 0.05-8 ox
$\Gamma_0 / \text{pmol cm}^{-2}$	$6.094 \pm 0.05$	$5.883 \pm 0.03$	$5.867 \pm 0.03$	$6.035 \pm 0.03$	$5.968 \pm 0.03$
$E_{o,1} / \text{mV}$	$-291.5 \pm 1.8$	$-238.5 \pm 0.7$	$-236.4 \pm 0.7$	-292	-292
$k_{e,1} / \text{s}^{-1}$	—	$368 \pm 14$	370	$40.9 \pm 2.1$	$124 \pm 15$
$E_{o,2} / \text{mV}$	$-252.1 \pm 3.0$	$-296.4 \pm 0.9$	$-292.5 \pm 0.8$	-252	-252
$k_{1,2} / \text{s}^{-1}$	—	10,000	10,000	—	—
$k_{e,2} / \text{s}^{-1}$	—	—	—	$69.7 \pm 5.4$	$17.2 \pm 0.9$
$E_{o,3} / \text{mV}$	$-233.2 \pm 2.8$	$-175.5 \pm 1.0$	$-173.3 \pm 1.0$	-233	-233
$k_{2,3} / \text{s}^{-1}$	—	10,000	10,000	—	—
$k_{e,3} / \text{s}^{-1}$	—	—	—	$93.5 \pm 8.5$	$103 \pm 11$
$E_{o,4} / \text{mV}$	$-169.5 \pm 1.4$	$-253.5 \pm 1.1$	$-252.1 \pm 1.1$	-170	-170
$k_{3,4} / \text{s}^{-1}$	—	10,000	10,000	—	—
$k_{e,4} / \text{s}^{-1}$	—	—	—	$85.0 \pm 6.0$	$19.6 \pm 1.0$
$\Delta E_{ps} / \text{mV}$	$39.2 \pm 0.6$	39.2	$44.2 \pm 0.4$	$48.1 \pm 0.5$	$39.8 \pm 0.6$

Table 7: Parameter values obtained by fitting different ET models to the CVs of activated CcO. Values that contain uncertainties indicated by  $\pm$  are fitted, whereas values without uncertainties are fixed in the fitting procedure. Note that in the 3<sup>rd</sup> column  $\Delta E_{ps}$  was fixed and  $k_{e,1}$  was fitted while in the 4<sup>th</sup> column  $\Delta E_{ps}$  was fitted and  $k_{e,1}$  was fixed. red and ox denote the reductive and the oxidative branch of the CV, respectively.

$$f_p = \Gamma/\Gamma_0 \quad (6.3)$$

was introduced which scales all j data to a common value  $\Gamma_0$ .  $\Gamma_0 = 6 \text{ pmol cm}^{-2}$  has been chosen, and this value was used as the initial value for  $\Gamma_0$  when fitting this parameter.

**Sequential ET model:** Fitting all the parameters at the same time proved to be impossible since the iterative procedure did not converge. In particular the rate constants of electron exchange increased with each iteration step. This is an indication for a fast electron exchange compared with the electron uptake and thus cannot be resolved. Hence a large and fixed value of  $10,000 \text{ s}^{-1}$  was assigned to these parameters. Yet, the procedure with the remaining parameters being fitted did not converge because of a too strong correlation between  $E_{o,1}$  and  $\Delta E_{ps}$ . Hence, a fixed value of 39.2 mV was assigned to  $\Delta E_{ps}$  which yielded the result shown in the 3<sup>rd</sup> column of table 7. Subsequently a fixed value of  $370 \text{ s}^{-1}$  was assigned to  $k_e$  and  $\Delta E_{ps}$  was fitted (see 4<sup>th</sup> column in table 7). The quality of fit between simulated and fitted data is shown, by way of example, for scan rates of 0.05, 0.4 and  $2 \text{ Vs}^{-1}$  in figure 6.13 (A), (B), and (C), respectively.

**Independent ET model:** Fitting both branches simultaneously using this model did not succeed since the iterative procedure did not converge. Reason for this becomes evident if the two branches were fitted separately. Convergence in this case could only



be achieved if fixed values for  $E_{o,i}$  taken from the equilibrated ET model were used. The values of all rate constants are significantly different for reductive and oxidative branch. This means that the model of independent ET has to be rejected because, according to basic physico-chemical principles, rate constants have to be independent of the direction in which  $E$  is changed. From this finding it can be concluded that ET in activated CcO is most likely described by the model of sequential ET.

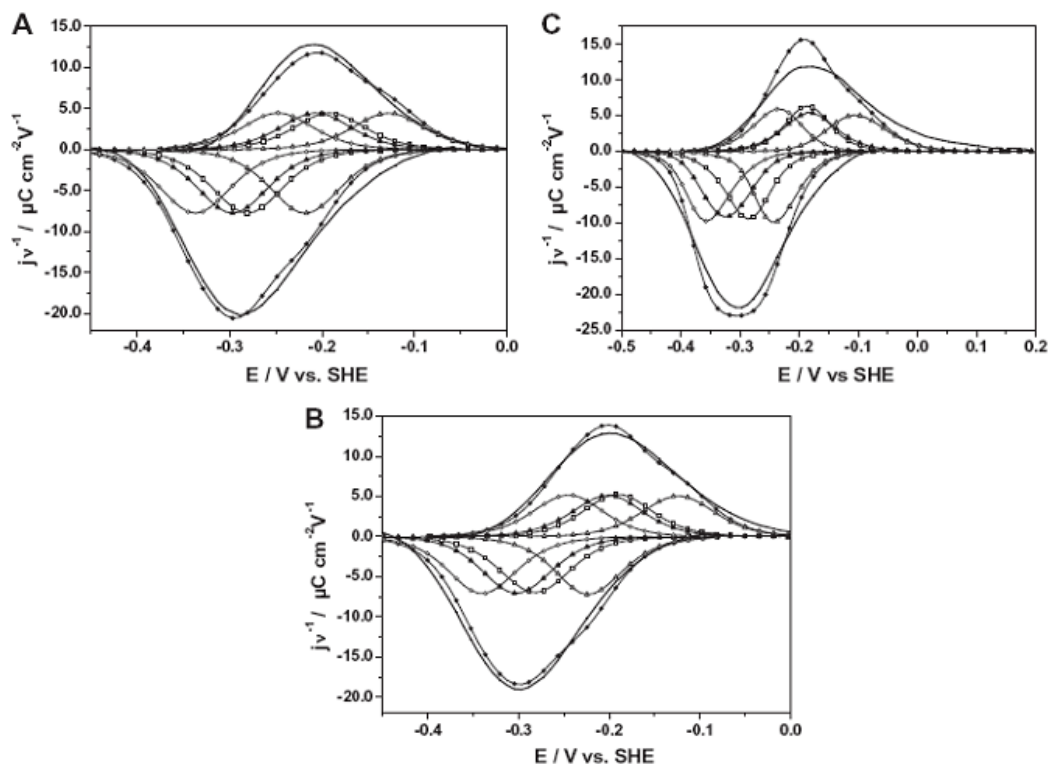


Figure 6.13: Experimental and simulated baseline-corrected and -normalized CVs of activated CcO. The CVs were taken under anaerobic conditions at  $\text{pH} = 8$  and at scan rates  $0.05$  (A),  $0.4$  (B) and  $2 \text{ V s}^{-1}$  (C). The experimental data (solid circles), the simulated total current density (solid line) and the components resulting from  $\text{Cu}_A$  (open squares), heme  $a$  (open circles), heme  $a_3$  (open triangles), and  $\text{Cu}_B$  (solid triangles) are plotted vs. the applied potential  $E$ . The CVs have been simulated by means of the model of sequential ET. The fit parameters are listed in table 7.

### 6.3.2 Non-Activated CcO

The baseline-correction for CVs of non-activated CcO (see figure 6.14) proved to be very difficult and yielded corrected CVs with at least two peaks and spread over a wider potential range as it is the case of activated CcO. This can be considered in terms of additional processes which have not yet been identified and hence cannot be separated from contributions attributable to the redox centers. Hence an analysis of non-activated CcO in a similar way as in the case of activated CcO was not possible. However a simplistic analysis could be achieved in the following way.

$ \nu  / \text{V s}^{-1}$	$\Gamma_{\text{red}} / \text{pmol cm}^{-2}$	$\Gamma_{\text{ox}} / \text{pmol cm}^{-2}$	$f_{\text{p,red}}$	$f_{\text{p,ox}}$
0.05	13.50	15.53	1.125	1.294
0.1	13.43	13.79	1.120	1.149
0.2	14.10	14.11	1.175	1.176
0.4	17.67	16.45	1.472	1.371
0.8	34.10	22.78	2.842	1.899
1.6	27.22	14.78	2.268	1.232
3.2	43.17	30.34	3.597	2.529
6.4	59.32	59.05	4.943	4.921
12.8	67.54	51.91	5.628	4.326

Table 8: Surface concentration  $\Gamma$  and scaling factor  $f_p$  for non-activated CcO with  $\Gamma_0 = 12 \text{ pmol cm}^{-2}$ . Red and ox refer to the reductive (cathodic) and oxidative (anodic) branch of CVs, respectively.

As in the case of activated CcO the  $\Gamma$ -values calculated for this E-range showed differences for the reductive and oxidative branch and a strong dependence on  $\nu$  for  $|\nu| > 0.4 \text{ V s}^{-1}$  (see table 8).

model	Equ. ET	Sequ. ET
$ \nu  / \text{V s}^{-1}$	0.05	0.05–0.4
potential limits / V	0.1–0.3	0.1–0.3
$\Gamma_0$ (pmol $\text{cm}^{-2}$ )	$6.39 \pm 0.16$	$5.788 \pm 0.037$
$E_{o,1}$ (mV)	$132.8 \pm 3.1$	$201.8 \pm 1.0$
$k_{e,1}$ ( $\text{s}^{-1}$ )	—	370
$E_{o,2}$ (mV)	$199.3 \pm 3.7$	$138.8 \pm 1.0$
$k_{1,2}$ ( $\text{s}^{-1}$ )	—	10,000
$E_{o,3}$ (mV)	$256.6 \pm 4.2$	$302.9 \pm 1.8$
$k_{2,3}$ ( $\text{s}^{-1}$ )	—	10,000
$E_{o,4}$ (mV)	$313.4 \pm 8.0$	$257.3 \pm 1.0$
$k_{3,4}$ ( $\text{s}^{-1}$ )	—	10,000
$\Delta E_{\text{ps}}$ (mV)	0	0

Table 9: Parameter values obtained by fitting the sequential ET model to the CVs of non-activated CcO. Values that contain uncertainties indicated by  $\pm$  are not fixed, whereas values without uncertainties are fixed in the fitting procedure. Only experimental data within the range of  $E$  indicated by limits were included.

However even the  $\Gamma$ -values for  $|\nu| \leq 0.4 \text{ V s}^{-1}$  are too high compared to the surface concentration of a densely packed layer of CcO. Hence the analysis was restricted to the potential range between 0.1 and 0.3 V and  $|\nu| \leq 0.4 \text{ V s}^{-1}$ . When using the equilibrated model  $\Delta E_{\text{ps}}$  was found to oscillate around a small value in successive iteration steps hence  $\Delta E_{\text{ps}}$  was set to 0 (see table 9). Since the independent ET could be excluded, the sequential ET was applied for the analysis at higher scan rates. As in the case of activated CcO the fixed values of  $10,000 \text{ s}^{-1}$  were assigned to the exchanged rate constants. When fitting  $k_{e,1}$  and  $E_{o,i}$  the procedure did not converge mainly due to large fluctuations of the

$k_{e,i}$  value in successive iterations. Therefore the fixed value  $k_{e,1} = 370 \text{ s}^{-1}$  as previously found for activated CcO was used which yielded the results shown in table 9. The quality of fit for two different scan rates which was obtained is displayed in figure 6.14. The fitted  $\Gamma_0$ -value is in good agreement with the theoretical value for a densely packed CcO layer. The values for  $E_{o,i}$  are well in the range of known potentials being reported in biochemical literature [185]. However, due to the restriction of the analysis to a limited E-range the fitted parameters are less reliable than in the case of activated CcO. In particular  $k_{e,1}$  should be regarded as one possible value, since varying the fixed  $k_{e,1}$ -value had little effect on the quality of fit and the fitted parameters. For this reason it is not possible to find a particular value for this rate constant. We can draw a conclusion from these findings that the model of sequential ET is not in contradiction with the experimental data for non-activated CcO.

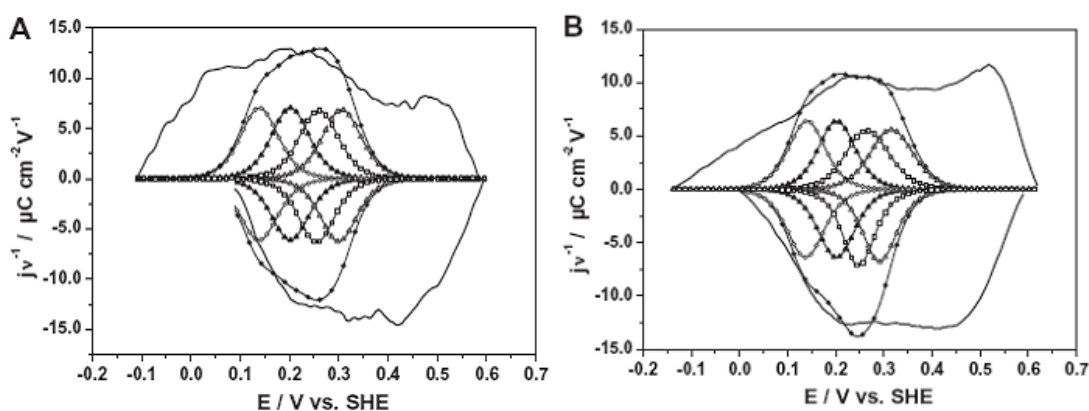


Figure 6.14: Experimental and simulated CVs for non-activated CcO at pH 8. Baseline-corrected and  $\nu$ -normalized CVs at scan rates  $0.05$  (A) and  $0.2 \text{ V s}^{-1}$  (B). The experimental data (solid line), the simulated total current density (solid circles) and the components resulting from  $\text{Cu}_A$  (solid triangles), heme  $a$  (open circles), heme  $a_3$  (open triangles), and  $\text{Cu}_B$  (open squares) are plotted vs. the applied potential  $E$ . CVs were simulated with the model of sequential ET and the fitted parameter values listed in table 9.

### 6.3.3 Summary and Conclusion

Two models describing the sequential and independent ET were designed. They were used to simulate CVs which were fitted to the baseline-corrected CVs by adjustment of parameters.

The analysis applying multistep-ET mechanisms indicates that direct ET to CcO in the activated state follows most likely the model of sequential ET (ECCC-mechanism). From this finding, it can be concluded that ET to CcO in the shown configuration (see figure 5.12) is an equivalent process to the ET from the genuine electron donor of CcO, i.e. cytochrome  $c$ . Since the simultaneous fit of reductive and oxidative branch did not succeed using the model of independent ET (EEEE-mechanism) this mechanism has to be rejected. The value for the electrochemical rate constant of ET to  $\text{Cu}_A$ ,  $k_{e,1}$ , which was obtained for the sequential ET model is found to be in good agreement with other proteins [5][4][6]. It is known that electron exchange processes inside the protein are much

faster than in the ET to  $Cu_A$ , which justifies the assignment of large fixed values to the rate constants of electron exchange.

The analysis of the CVs of non-activated CcO is hampered by the fact that processes which cannot be identified interfere with the signals from the redox centers. However by means of an E-range restricted analysis, it is found that the model of sequential ET is not in contradiction with the data. The redox potentials that were obtained for non-activated CcO are less reliable than those found for activated CcO since an E-range restricted analysis had to be used. Nevertheless, the obtained values are in good agreement with biochemical literature [184].

The shift in redox potentials when activating CcO most likely indicates different conformations of the two states of CcO. The effect of a change in conformation on the  $E_m$  values of hemes was calculated before by means of Multi-Conformation Continuum Electrostatics calculations [59] and experimentally shown for an enzyme with a similar catalytic cycle, the BM3 heme [56][67].

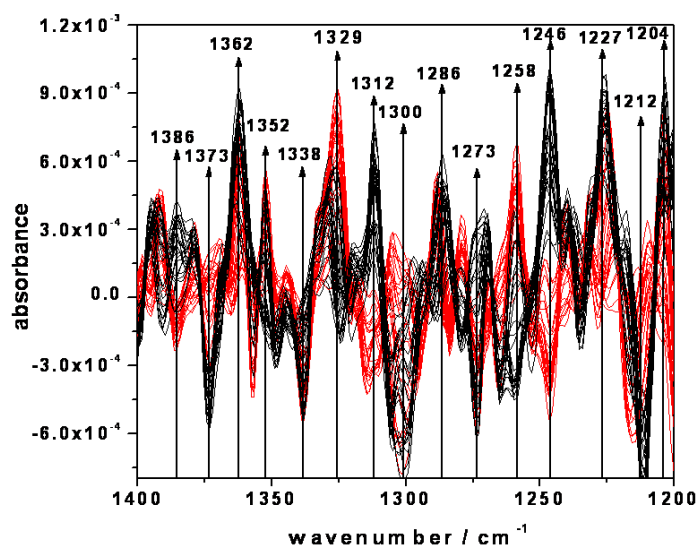
The averaged surface concentration which was found to be  $\bar{\Gamma} \approx 7 \text{ pmol cm}^{-2}$ , as well as the fitted values for  $\Gamma_0$  are compatible with the calculated surface concentration,  $\Gamma = 6 \text{ pmol cm}^{-2}$ , for a densely packed monolayer of CcO. In this calculation the enzyme was approximated as an ellipsoid disk with  $r_1 = 4.5 \text{ nm}$  and  $r_2 = 7.0 \text{ nm}$  which were estimated by means of crystallography data of CcO of *R. sphaeroides* [77]. From these findings it is concluded that the monolayer of CcO is densely packed in a ptBLM with the orientation of CcO as it is shown in figure 5.12. This confirms the results obtained in section 6.1.

## 6.4 Time-Resolved Surface-Enhanced Infrared Spectroscopy of CcO

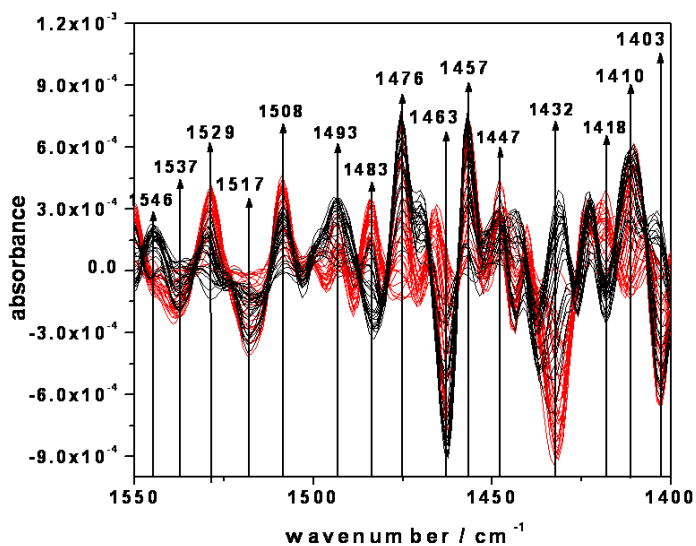
### 6.4.1 Anaerobic Conditions

#### 6.4.1.1 Activated CcO

According to the procedure described previously CcO was immobilized onto the two-layer gold surface on the ATR crystal and then reconstituted into the ptBLM. By means of performing repeated catalytic cycles, CcO was transformed into the activated state (see section 6.2). tr-SEIRA spectra were recorded under anaerobic conditions and difference



(a)

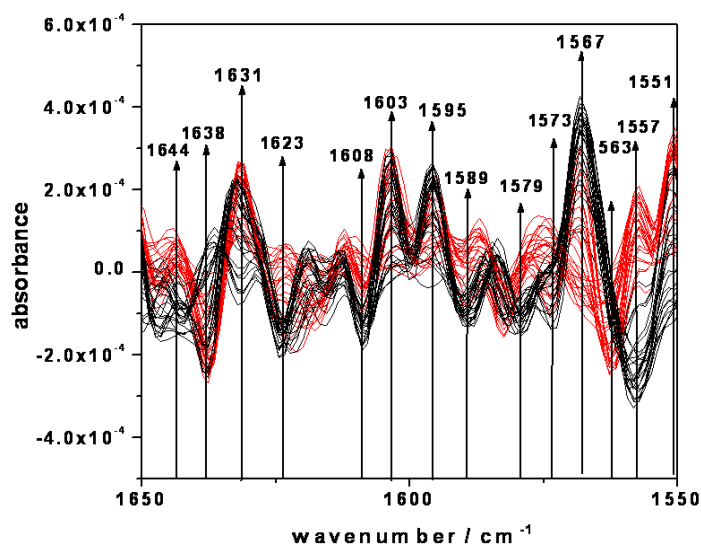


(b)

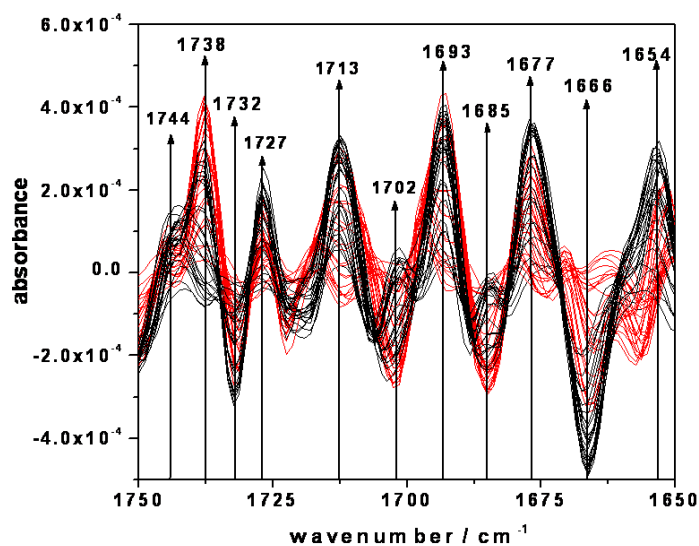
Figure 6.15: Tr-SEIRA spectra taken at 400 Hz under anaerobic conditions ( $pH = 8$ ) in the range between 1200 and 1400 (a) and 1400 and 1550 (b) which is the fingerprint region. Difference spectra refer to oxidative (red) and reductive half period (black).

## 6.4 Time-Resolved Surface-Enhanced Infrared Spectroscopy of CcO

spectra were calculated (oxidized minus reduced). A resolution of  $1 \mu\text{s}$  at a coaddition number of 500 was chosen in the step scan mode. The response of CcO depends on the



(a)



(b)

Figure 6.16: Tr-SEIRA spectra taken at 400 Hz under anaerobic conditions ( $\text{pH} = 8$ ) in the range between 1550 and 1650 (a) and 1650 and 1750 (b) which is the amide region. Difference spectra refer to oxidative (red) and reductive half period (black).

kinetic parameters of the redox transition, hence a frequency of the electrochemical excitation has to be adjusted to the response. By applying frequencies between 1 kHz to 10 Hz it was found that the appropriate frequency for activated CcO under anaerobic conditions is in the range between 400 and 800 Hz. Particularly the spectra taken at 400 Hz show well-resolved bands, hence these spectra were analyzed. Cyclic voltammetry has shown that the redox centers of activated CcO achieve the fully reduced and the fully oxidized state at potentials of  $-0.6 \text{ V}$  and  $0.2 \text{ V}$ , respectively (see figures 6.13). Due to

the electrode charging which is described in section 5.3.7.1, the potential effective for the redox centers differs from the externally applied potential pulses  $E_p$ . With the potentials  $E_{p,0}$  and  $E_{p,1}$  set to -0.8 and 0.4 V, respectively, the effective potential ranges between -0.6 and 0.2 V (see figure 5.31) as required by CcO to be fully reduced and fully oxidized. In figures 6.15 and 6.16 the series of SEIRA spectra taken at 400 Hz in the range between 1200 and 1750  $\text{cm}^{-1}$  are presented as an example. Since the spectra contain a large number of vibrational modes, they had to be subdivided into four parts.

**Assignment of bands:** Bands which were found in the spectra are collected in tables 10 and 11. The redox state ox denotes positive bands in the difference spectra when oxidizing CcO and using the spectrum of the fully reduced enzyme as the reference (ox-red). The redox state red denotes positive bands in the difference spectra when reducing CcO and using the spectrum of the fully oxidized enzyme as the reference (red-ox) (This refers to the commonly used expression found in literature). Redox states marked with n.d. could not be determined, since negative and positive signals occur in the spectra at the same wavenumber. Most of the bands were tentatively assigned to the environments of the redox centers on the basis of literature data obtained by potentiometric titrations followed simultaneously by FTIR and UV/VIS spectroscopy [185][123][102][105]. For the vibrational modes of involved amino acids and peptide bonds see literature. The pattern of the bands is consistent with data reported in literature. Comparing e.g. the difference spectra obtained by perfusion with dithionite of CcO from *R. sphaeroides* reconstituted in lipid vesicles the most prominent bands (1745, 1735, 1705, 1684, 1676, 1676, 1662, 1650, 1622, 1560, 1548, 1537, 1522 and 1498  $\text{cm}^{-1}$  [63]) are close to the bands found in the present spectra. The consistency of these bands is an important test since this indicates the stability of proteins immobilized in the membrane system. The spectra obtained from tr-SEIRAS also show bands similar to those measured under static conditions, however the number of bands found by means of tr-SEIRAS is higher [132]. The reason for this could be that the region around the CO stretching vibration of the amide I bands between 1640 and 1747  $\text{cm}^{-1}$  is better resolved into single bands. The presented spectra also show a large number of bands, particularly in the fingerprint region (1200 - 1500  $\text{cm}^{-1}$ ) and some of them were not yet mentioned in the literature. Conformational changes of  $\alpha$ -helices surrounding the hemes are indicated by bands at 1657 and 1666  $\text{cm}^{-1}$ , which have also been observed in tr-studies after CO dissociation [61]. In particular the amide I band at 1657  $\text{cm}^{-1}$  is attributed to the transition between the E and the R state, at which an electron is transferred from heme a to the catalytic center [62]. Bands at 1666, 1645, 1635  $\text{cm}^{-1}$  also characterize heme formyl stretching vibrations of heme  $a_3$ . A band pair occurring in the range 1732-1735  $\text{cm}^{-1}$  and 1745-1747  $\text{cm}^{-1}$  was detected often times in difference spectra (reduced-oxidized) of CcO from *R. sphaeroides* usually with a negative peak at 1745 and a positive peak at 1735  $\text{cm}^{-1}$  [63][110]. The presented spectra were measured starting with the fully reduced form of the enzyme and applying potential pulses with the positive edge, i.e. changing to the fully oxidized form. These peaks are considered to indicate the glutamic acid E286 (see figure 6.17) in its protonated and deprotonated form, respectively. In these spectra a relatively small positive signal at 1747  $\text{cm}^{-1}$  as well as a negative signal at 1732  $\text{cm}^{-1}$  are superimposed by a large positive band at 1738  $\text{cm}^{-1}$ . The bands at 1732 and 1747  $\text{cm}^{-1}$ , which are mostly found in bacterial CcO, are assumed to origin from the deprotonated and reprotonated E286. This amino acid is considered crucial for the proton pumping mechanism as part of the

D-channel [61]. Alternatively a change in the environment of the hydrogen-bonding of the protonated carboxylic acid moiety was also proposed [63]. E286 is located 2.5 nm afar from the protein surface near the proton-entry side and 1 nm afar from the binuclear center. This amino acid was shown to be involved in the photodissociation of the CO adduct of CcO [61]. The spectra also indicate a conformational change of E286, nevertheless, it is expected to be mainly in the protonated state, since the band at  $1747\text{ cm}^{-1}$  is relatively small. This finding is consistent with the absence of the proton pumping, since a deoxygenated solution was used. The strong band which occurs at  $1738\text{ cm}^{-1}$  can be attributed to protonated Asp D214 also found in [83]. However the absence of the proton pumping does not exclude the protonation related to the reduction of the hemes. A negative and a positive band at  $1403$  and  $1595\text{ cm}^{-1}$ , respectively, indicated the alternation between protonated and deprotonated state of the aspartic acid, D214 (see figure 6.17). Bands at  $1403$ ,  $1418$ ,  $1727$ , and  $1738\text{ cm}^{-1}$  are characteristic for Asp-COOH, whereas a band at  $1595\text{ cm}^{-1}$  results from vibrations of Asp-COO<sup>-</sup>. The D214 being located in the vicinity of heme  $a_3$  seems to be involved in the charge compensation of protons. Bands at  $1573$ ,  $1529$ ,  $1386\text{ cm}^{-1}$  are characteristic for the deprotonated pro-

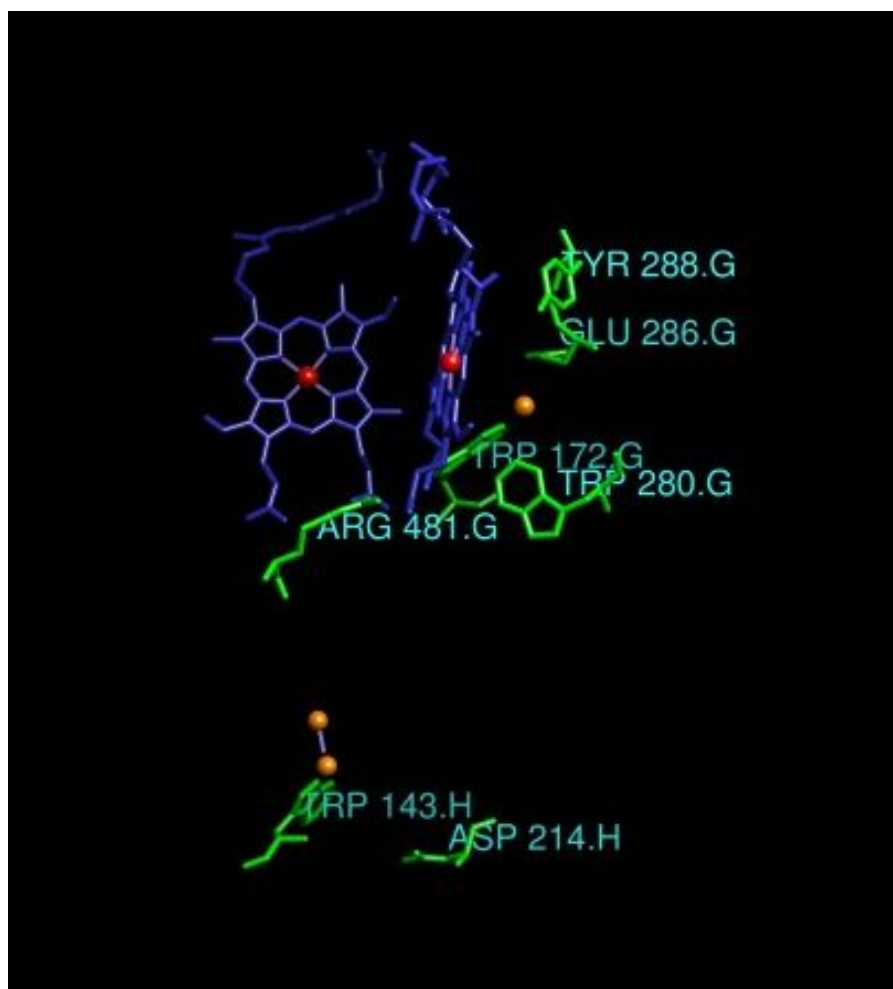


Figure 6.17: Several important residues (green, labeled light blue) near the redox centers ( $Cu_A$  (orange), the hemes (blue with red center) and  $Cu_B$  (orange)) which have been assigned to some of the vibrational modes occurring in our spectra.



pionate groups of both hemes. The band at  $1678\text{ cm}^{-1}$  on the contrary can be attributed to the protonated form of the ring A propionate of heme  $a_3$ , which is considered to be involved in the proton uptake as a function of heme reduction [64]. As expected, the amino acids of the D- and the K-channel do not have contributions in the spectra, since the measurements were performed in a deoxygenated solution. A band at  $1623\text{ cm}^{-1}$  originates from the protonated form of Y288 (see figure 6.17), still being consistent with the absence of the proton pumping. Y288 was proposed to be involved in the transition from the R to the  $P_m$  state, in which a radical is suggested to form being indicated by signals at  $1522$  and  $1479\text{ cm}^{-1}$  [61]. Signals in this region of the presented spectra were also found, however they have to be attributed to other groups, such as the propionate. Bands at  $1677$ ,  $1631$  and  $1595\text{ cm}^{-1}$  were attributed to amino acids, such as the Arg-H5<sup>+</sup> (R481) (see figure 6.17). Characteristic bands for Trp W143 (see figure 6.17), W172 (see figure 6.17), W280 occur at  $1623$ ,  $1483$ ,  $1403$ ,  $1329$  and  $1314\text{ cm}^{-1}$ . A further glutamic acid but this time in the deprotonated state seems to be the reason for the band at  $1403\text{ cm}^{-1}$ . Protonated arginines together with reverse ET from heme  $a_3$  to heme a in bovine CcO were supposed to generate a band feature of  $1638/1677\text{ cm}^{-1}$  [202]. Contributions which were assigned to several histidines, such as H411 ( $1630\text{ cm}^{-1}$ ), H260, H214, ( $1595\text{ cm}^{-1}$ ), H333, H334 ( $1312\text{ cm}^{-1}$ ), H284 ( $1457\text{ cm}^{-1}$ ), H217, H260 ( $1419\text{ cm}^{-1}$ ) could be found. Some histidines which were expected to coordinate  $\text{Cu}_B$ , the H276, H325, H326 were proposed to be a part of a cluster of residues, such as Glu (E286) (see figure 6.17) and Asp (D214) (see figure 6.17) which control the proton pathways above the binuclear center [102]. The amino acids which were found here are located in a close distance to the redox centers. On the basis of previous investigations, the signals in these spectra were tentatively assigned to bands (see column 3 of tables 10 and 11) resulting from redox changes (see column 4) of different redox centers (see column 5). Most important for the quantitative analysis of the spectra is the assignment of bands to certain redox centers, hence the tables contain only the assignment to the redox centers but not to the amino acids. Particular bands which could be assigned to  $\text{Cu}_A$  ( $1518$ ,  $1603$ ,  $1693\text{ cm}^{-1}$ ), heme a ( $1537$ ,  $1666\text{ cm}^{-1}$ ), heme  $a_3$  ( $1637$ ,  $1677\text{ cm}^{-1}$ ) and  $\text{Cu}_B$  ( $1476\text{ cm}^{-1}$ ) were further analyzed in order to investigate ET kinetics.

## 6.4 Time-Resolved Surface-Enhanced Infrared Spectroscopy of CcO

wavenumber of band / $\text{cm}^{-1}$ ( <b>exp.</b> )	redox state ( <b>exp.</b> )	wavenumber of band / $\text{cm}^{-1}$ ( <b>lit.</b> )	redox state ( <b>lit.</b> )	redox center ( <b>lit.</b> )
1204	ox	—	—	—
1212	red	—	—	—
1227	ox	—	—	—
1246	n.d.	—	—	—
1258	n.d.	—	—	—
1273	n.d.	—	—	—
1286	ox	—	—	—
1300	red	—	—	—
1312	n.d.	1308	ox	Cu <sub>B</sub>
1329	ox	1332	ox	Cu <sub>B</sub>
1338	red	—	—	—
1352	ox	—	—	—
1362	ox	—	—	—
1373	red	—	—	—
1386	n.d.	1389	ox	heme a
1403	red	1407	red	Cu <sub>A</sub>
1410	ox	—	—	—
1432	n.d.	1431	ox	Cu <sub>A</sub>
1447	ox	1455	ox	Cu <sub>B</sub>
1457	ox	1455	ox	Cu <sub>B</sub>
<b>1463</b>	red	1473	red	heme a <sub>3</sub>
<b>1476</b>	ox	1483	ox	Cu <sub>B</sub>
1483	n.d.	1483	ox	Cu <sub>B</sub>
1493	ox	1498	ox	hemes *
1508	ox	—	—	—
<b>1517</b>	red	1510	red	Cu <sub>A</sub>

*Table 10: Low wavenumber-band position (1<sup>st</sup> column) and redox state (2<sup>nd</sup> column) found experimentally. Tentative band assignments according to [184] and [123] (latter marked with \*). Redox states marked with n.d. were not defined. Wavenumber of bands (3<sup>rd</sup> column), redox state (4<sup>th</sup> column) and environments assigned to redox centers (5<sup>th</sup> column) found from literature. Wavenumbers given in bold denote bands which have been further analyzed. Bands in the spectra without assignment have not yet been reported in the literature.*

wavenumber of band / $\text{cm}^{-1}$ ( <b>exp.</b> )	redox state ( <b>exp.</b> )	wavenumber of band / $\text{cm}^{-1}$ ( <b>lit.</b> )	redox state ( <b>lit.</b> )	environment of redox center ( <b>lit.</b> )
<b>1529</b>	ox	1537	ox	heme a
1537	red	1546	red	heme a
1546	red	1546	red	heme a
1551	ox	—	—	—
1557	n.d.	1561	ox	heme a <sub>3</sub>
1567	ox	1561	ox	heme a <sub>3</sub>
1573	n.d.	1572	ox	heme a <sub>3</sub> *
1579	red	—	—	—
1595	ox	1592	ox	Cu <sub>A</sub>
<b>1603</b>	ox	1592	ox	Cu <sub>A</sub>
1608	red	1603	red	Cu <sub>A</sub>
1623	red	1618	red	heme a <sub>3</sub>
1631	ox	1641	ox	heme a <sub>3</sub>
<b>1638</b>	red	1630	red	heme a <sub>3</sub>
1644	ox	1641	ox	heme a <sub>3</sub>
1654	ox	1655	ox	heme a <sub>3</sub>
<b>1666</b>	ox	1661	ox	heme a
<b>1677</b>	ox	1674	ox	heme a <sub>3</sub>
1685	red	1684	red	Cu <sub>A</sub>
<b>1693</b>	ox	1689	ox	Cu <sub>A</sub>
1702	red	1694	red	heme a <sub>3</sub>
1713	ox	1708	ox	heme a <sub>3</sub> *
1727	ox	1720	ox	heme a <sub>3</sub> *
1732	red	1734	red	heme a <sub>3</sub> *
1738	ox	1746	ox	heme a
1744	ox	1746	ox	heme a

Table 11: High wavenumber-band positions (1<sup>st</sup> column) and redox state (2<sup>nd</sup> column) found experimentally. Tentative band assignments according to [184] and [123] (latter marked with \*). Redox states marked with n.d. were not defined. Wavenumber of bands (3<sup>rd</sup> column), redox state (4<sup>th</sup> column) and environments assigned to redox centers (5<sup>th</sup> column) found from literature. Wavenumbers given in bold denote bands which have been further analyzed. Bands in the spectra without assignment have not yet been reported in the literature.

**Simulation and parameter fitting:** The bands at positions indicated by bold numbers in tables 10 and 11 were quantified by deconvolution of the spectra with a Voigt-shape function (Lorentzian and Gaussian band shape 20 %: 80 %). These bands fulfill the criteria that they are not superimposed by other bands and their position remained at the same wavenumber during the entire measurement. The deconvolution yields the band area as a function of time. Due to different uncertainties in the fitting procedure, errors of 5% for the bands at 1529, 1463, 1476, 1693 and 1603  $\text{cm}^{-1}$  and 10% for the bands at 1677, 1637, 1666 and 1517  $\text{cm}^{-1}$  were estimated. In figures 6.18, 6.19, 6.20, and 6.21 plots of band areas vs. time for  $\text{Cu}_A$  (1517, 1603, 1693  $\text{cm}^{-1}$ ), heme a (1529, 1666  $\text{cm}^{-1}$ ), heme a<sub>3</sub> (1463, 1638, 1677  $\text{cm}^{-1}$ ) and  $\text{Cu}_B$  (1476  $\text{cm}^{-1}$ ) are illustrated, respectively (full circles).

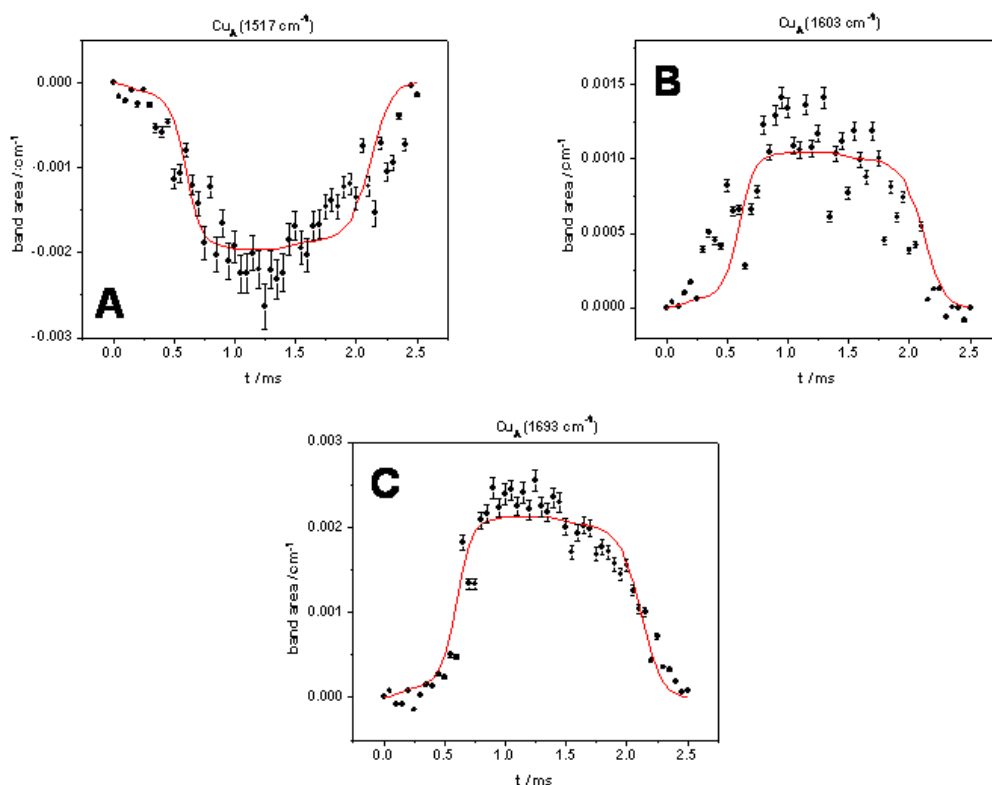


Figure 6.18: Plots of band area vs. time (full circles) for the bands at 1517 (A), 1603 (B) and 1693  $\text{cm}^{-1}$  (C) referring to the environment of  $\text{Cu}_A$ . The plots were fitted by means of the model of sequential ET to CcO (red line).

The data were analyzed by means of the model of sequential ET. Starting from the fully reduced protein, i.e.  $p_k = 0$  for  $k = 0, 1, \dots, 15$  and  $p_{16} = 1$  since  $E_{p,0} < E_{o,i}$  in the experiments, several pulses were simulated until the time courses  $p_{i,\text{red}}(t)$  in subsequent pulses coincide for each of the redox centers. The band area for different bands associated with a given center can then be calculated by means of equation 5.86 rewritten for band area using appropriate values for  $\Delta A_{i,\text{red-ox}}(\tilde{\nu})$  and  $A_{i,0}(\tilde{\nu})$ . The result of this analysis is shown in tables 12 and 13 and in figures 6.18, 6.19, 6.20, and 6.21 (red lines).

The charging of the electrode interface causes a delay which is visible in the plots for  $\text{Cu}_A$  as a slow rising phase up to about 0.5 ms. The rate constant for electron uptake ( $k_{e,1}$ ) is much smaller than the rate constants of electron exchange ( $k_{1,2}$ ,  $k_{2,3}$ , and  $k_{3,4}$ )

parameter	fitted value
$\tau$ / ms	$0.788 \pm 0.012$
$E_{o,1}$ / mV	$-259.3 \pm 4.2$
$k_{e,1}$ / $s^{-1}$	300
$E_{o,2}$ / mV	$-231.2 \pm 3.9$
$k_{1,2}$ / $s^{-1}$	20000
$E_{o,3}$ / mV	$-229.6 \pm 4.5$
$k_{2,3}$ / $s^{-1}$	$10^7$
$E_{o,4}$ / mV	$-244.1 \pm 5.8$
$k_{3,4}$ / $s^{-1}$	$10^7$

Table 12: Parameter values obtained by fitting the sequential ET model to the time-dependence of band areas (see figures 6.18, 6.19, 6.20 and 6.21) for activated CcO. Values that contain uncertainties indicated by  $\pm$  are fitted, whereas values without uncertainties are fixed in the fitting procedure.

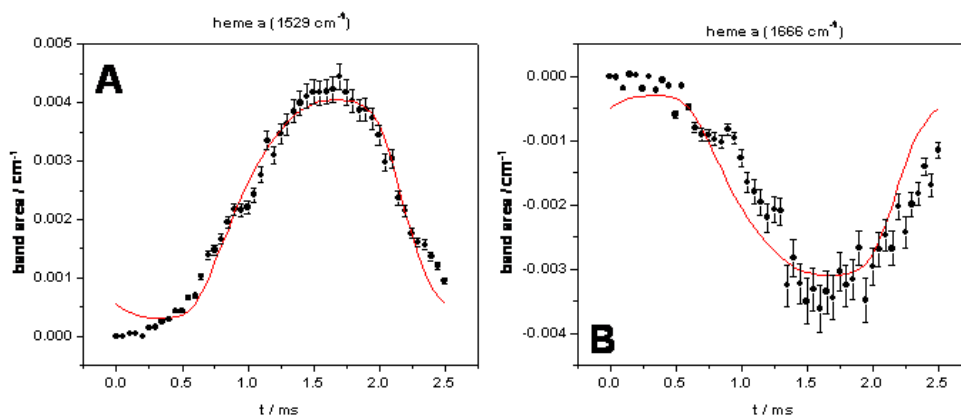


Figure 6.19: Plots of band area vs. time (full circles) for the bands at 1529 (A) and 1666  $cm^{-1}$  (B) referring to the environment of heme a. The plots were fitted by means of the model of sequential ET to CcO (red line).

which means that the chemical reactions are almost equilibrated.

From the values of  $E_{o,1}$  and  $E_{o,2}$  the equilibrium constant for the electron exchange between  $Cu_A$  and heme a can be calculated:

$$K_{1,2} = \exp \{F(E_{o,2} - E_{o,1})/RT\} \quad (6.4)$$

Inserting the values from table 12 yields  $K_{1,2} = 3.0 \pm 0.7$ , which compares well with  $K_{1,2} = 3.4 \pm 0.5$  reported in the literature for the reaction  $Cu_A(I)Fe_a(III) \rightleftharpoons Cu_A(II)Fe_a(II)$  at  $25^\circ C$  and  $pH = 7.4$  [147]. Moreover, the value for  $k_{1,2}$  found in the present analysis is somewhat larger than but still compatible with  $k_{1,2} = 13,000 \pm 1,200 s^{-1}$  reported in this paper.

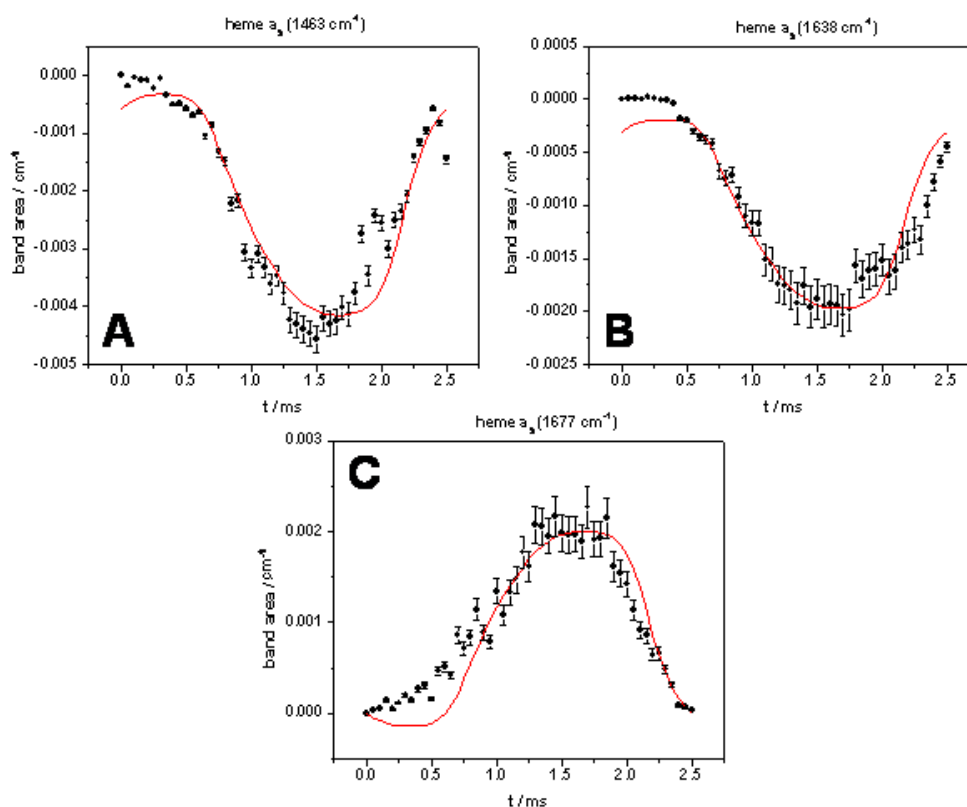


Figure 6.20: Plots of band area vs. time (full circles) for the bands at 1463 (A), 1638 (B) and 1677  $\text{cm}^{-1}$  (C) referring to the environment of heme  $a_3$ . The plots were fitted by means of the model of sequential ET to CcO (red line).

#### 6.4.1.2 Non-Activated CcO

Previously it was shown by CV that CcO in the non-activated state can be electrochemically reduced and oxidized [132][131][22]. However, tr-SEIRAS with CcO in the non-activated state did not yield any useful spectral response even using different potential windows and different frequencies down to 10 Hz. The spectra did not show a systematic but rather erratic change in absorbance with time. This could be due to an incoherent behavior of the CcO molecules.

#### 6.4.2 Aerobic Conditions

Tr-SEIRA spectra were also tentatively recorded for activated CcO under aerobic conditions. The principle of measurement was the same as discussed in the previous section. Different  $\text{O}_2$  concentrations were achieved by flushing PBS buffer at r.t. (pH = 8) with a gas containing different ratios of  $\text{O}_2$  and Ar. Periodically alternating potential pulses at frequencies between 100 Hz and 5 kHz were applied. Interestingly, the spectra of CcO under aerobic conditions taken at high frequencies (1-2 kHz) yield remarkably well-resolved bands as compared to CcO measured under anaerobic conditions. In figures 6.22 (a) and (b) spectra taken at 1 kHz referring to the oxidative (blue) and reductive half period (black) are illustrated as an example. Several bands in the spectra could be assigned to

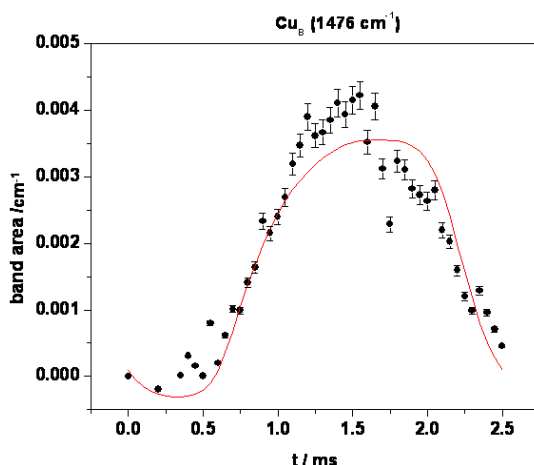


Figure 6.21: Plot of band area vs. time (full circles) for the bands at  $1476 \text{ cm}^{-1}$  referring to the environment of  $\text{Cu}_B$ . The plot was fitted by means of the model of sequential ET to CcO (red line).

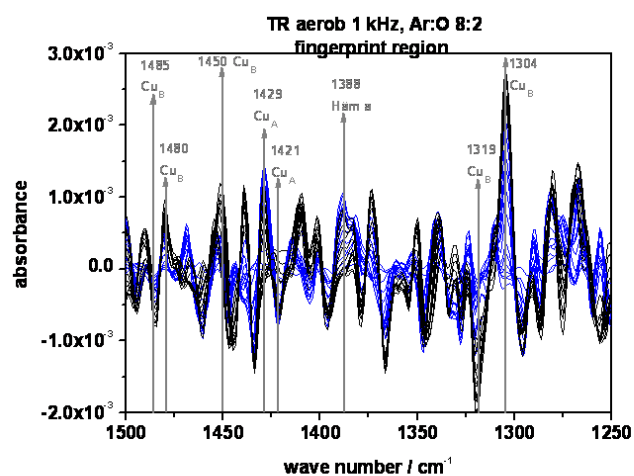
wavenumber of band / $\text{cm}^{-1}$	redox center	$\Delta A \cdot 10^3 / \text{cm}^{-1}$	$A_0 \cdot 10^3 / \text{cm}^{-1}$
1517	$\text{Cu}_A$	$1.980 \pm 0.071$	0
1603	$\text{Cu}_A$	$-1.058 \pm 0.071$	0
1693	$\text{Cu}_A$	$-2.149 \pm 0.071$	0
1537	heme a	$-4.515 \pm 0.156$	$0.559 \pm 0.076$
1666	heme a	$3.382 \pm 0.156$	$-0.490 \pm 0.076$
1463	heme $a_3$	$4.639 \pm 0.161$	$-0.574 \pm 0.075$
1638	heme $a_3$	$2.162 \pm 0.161$	$-0.305 \pm 0.075$
1677	heme $a_3$	$-2.606 \pm 0.108$	0
1476	$\text{Cu}_B$	$-4.480 \pm 0.150$	$0.088 \pm 0.076$

Table 13:  $\Delta A$  ( $3^{\text{rd}}$  column) and  $A_0$  ( $4^{\text{th}}$  column) (see equation 5.86) referring to the bands ( $1^{\text{st}}$  column) that have been analyzed to study the redox kinetics of the redox centers ( $2^{\text{nd}}$  column).

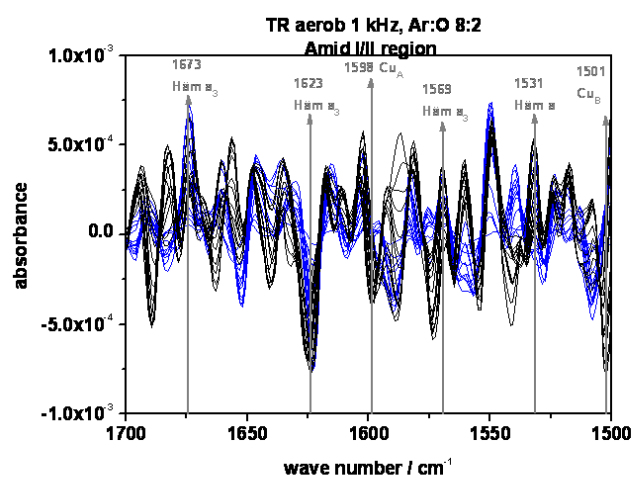
the environment of redox centers according to literature data [184]. However, the band area vs. time plots (figure 6.23 (a) and (b)) of some bands found in spectra taken at different  $\text{O}_2$  concentrations and frequencies do not show a periodic response. The band areas corresponding to the spectra measured at the lower  $\text{O}_2$  concentration decline after one half period to a certain value, however they do not reach the initial value again (see figure 6.23 (a)). These band areas seem to plateau at approximately half of the maximum value. The system which was measured at the same frequency in an  $\text{O}_2$ -saturated buffer yields spectra which are not reversible at all (see figure 6.23 (b)). The band areas constantly increase during the entire measurement and seem to plateau at a maximum value. Comparing both plots and those found under anaerobic conditions it can be deduced that the concentration of oxygen plays a role for the reversibility of the system.

This behavior could indicate that the system is not stable during the time of the measurement. Whatever the reason for the not yet stable state, these measurements are at least unreliable (or even meaningless) since the periodicity of the system is a

prerequisite for the tr-SEIRAS in the step-scan mode.



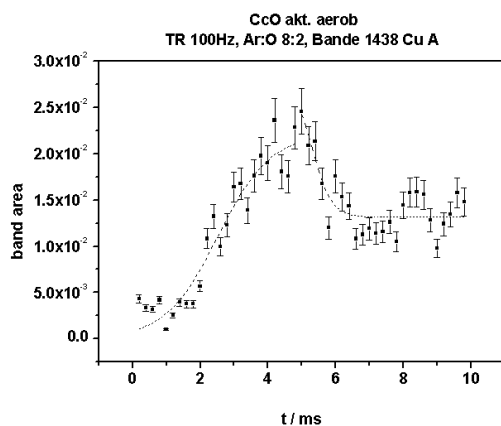
(a)



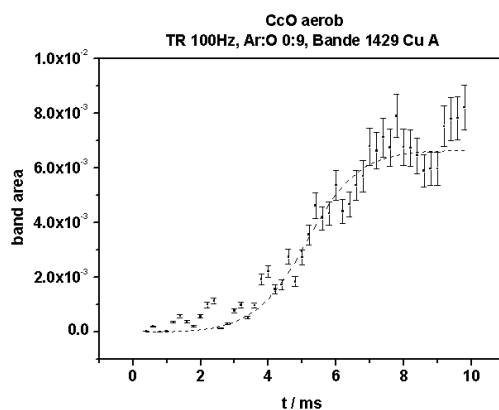
(b)

Figure 6.22: Tr-SEIRA spectra taken at 1 kHz under aerobic conditions ( $pH = 8$ ) in the range between 1250 and 1500 (a) and 1500 and 1700 (b) which is the fingerprint and the amide region, respectively. Spectra refer to oxidative (blue) and reductive half period (black).





(a)



(b)

Figure 6.23: Band area vs. time plots for activated CcO under aerobic conditions measured at an exciting pulse frequency of 100 Hz and a mixing ratio Ar:O<sub>2</sub> of 8:2 (a) and 0:9 (b). Both bands at 1438 (a) and 1429 cm<sup>-1</sup> (b) could be assigned to the same vibrational mode of the Cu<sub>A</sub> environment. The irreversibility of the band areas seems to be dependent on the O<sub>2</sub> concentration and could indicate a constant change of the system, thus *tr-SEIRAS* is not applicable in this particular case.

### 6.4.3 Summary and Conclusion

Electrochemically induced *tr-SEIRAS* at 400 Hz under anaerobic conditions was applied to investigate the kinetics of direct ET to activated CcO. From the recorded difference spectra redox-dependent conformational changes of amino acids in the environment of the redox centers could be detected as a response to the applied potentials. The pattern of the bands found is consistent with the data found in the literature. On the basis of a tentative band assignment according to literature [185][123][102][105] it could be shown that only residues near the redox centers and the electron pathway contribute to the

difference spectra, whereas amino acids being located near the D- and the K-channel do not show any redox-dependent signal. These findings are consistent with the expectations since the measurements were performed in a deoxygenated solution.

The time-dependence of some bands of the difference spectra which have been attributed to the environments of single redox centers indicating their redox state, were analyzed by means of the model of sequential ET. This corroborates the conclusion drawn in context of fast scan voltammetry.

All attempts to investigate ET to non-activated CcO by means of electrochemically induced tr-SEIRAS at different potential ranges and frequencies failed.

tr-SEIRAS of activated CcO under aerobic conditions yielded puzzling results which are not easily understood. These results are at least unreliable (or even meaningless) since they violate the principle of reversibility required for tr-SEIRAS.

## 7 Overall summary

At the beginning of this work the conditions for the binding of CcO to the electrode had to be optimized. To this end, several mole fractions of linker molecules were tested. By means of EIS it could be shown that the mole fraction  $x = 0.2$  is the optimum condition for the adsorption of a sufficient amount of enzyme and the formation of a membrane. The organization of the ptBLM at this mole fraction was verified by recording the SPR kinetic trace. The SPR measurement yields reliable values for the thickness of the layers in the ptBLM. Cyclic voltammetry was used under anaerobic and aerobic conditions to show that CcO forms a densely packed layer at this surface concentration. It was also found that the enzyme is most active with these conditions.

With the optimum surface concentration cyclic voltammograms were performed. Peaks measured under anaerobic conditions in the range between 0.2 and 0.6 V were assigned to ET to the redox centers. These peaks decline to zero when performing CVs in the range between 0.3 and -0.8 V under aerobic conditions. At the same time two peaks at -0.2 and -0.55 V which are sensitive to the oxygen concentration occur. Hence they are regarded as resulting from turnover of the enzyme, i.e. ET and proton transfer. Only the peak at -0.2 V remained if changing back to anaerobic conditions which is an indication for ET. This finding shows that the peak potential which is proposed to result from ET shifts from 0.2 to -0.2 V while doing CVs under aerobic conditions. It is suggested that CcO undergoes a conformational transition from a non-activated to an activated state of the enzyme. They are considered to correspond to the so-called resting and pulsed state, respectively [47][104].

Studies applying the proposed multistep-ET mechanisms indicate that direct ET to CcO in the activated state follows most likely the model of sequential ET (ECCC-mechanism). Hence it can be concluded that ET to CcO in the presented configuration (see figure 5.13) is equivalent to ET from the genuine electron donor of CcO, i.e. cytochrome c. However, the model of independent ET (EEEE-mechanism) must be rejected since a simultaneous fit of reductive and oxidative branch did not succeed in this case. The investigation using the sequential ET model yields an electrochemical rate constant of ET to  $\text{Cu}_A$ ,  $k_{e,1}$ , which is found to be in good agreement with other proteins [5][4][6]. Electron exchange processes inside the enzyme are known to be much faster than ET to  $\text{Cu}_A$  which justifies the assignment of large fixed values to the rate constants of electron exchange.

The analysis of the CVs of non-activated CcO is hampered by the fact that processes which cannot be identified interfere with the signals from the redox centers. However an E-range restricted analysis shows that the model of sequential ET is not in contradiction with the data. The redox potentials that were found for non-activated CcO are less reliable than those found for activated CcO since an E-range restricted analysis had to be used. Nevertheless, the values are in good agreement with biochemical literature [184].

The shift in redox potentials which is observed when activating the enzyme is proposed to be due to different structural conformations of the two states of CcO. Effects of conformational changes on the  $E_m$  values of hemes were calculated before using Multi-Conformation Continuum Electrostatics calculations [59].

Integration of the peak area yielded the surface concentration  $\Gamma$ . The value for the averaged surface concentration was found to be  $\bar{\Gamma} \approx 7 \text{ pmol cm}^{-2}$ , thus being compatible with the calculated surface concentration,  $\Gamma = 6 \text{ pmol cm}^{-2}$ , for a densely packed mono-

---

layer of CcO. From these findings it is concluded that the monolayer of CcO is densely packed with the orientation of CcO as shown in figure 5.12.

Electrochemically induced tr-SEIRAS at 400 Hz performed under anaerobic conditions was used to study direct ET to activated CcO. Redox-dependent conformational changes of amino acids in the vicinity of redox centers were detected in the difference spectra as a response to the applied potential pulses. Most of the bands were previously reported in literature [185][123][102][105]. Based on a tentative band assignment according to these data it was shown that vibrational modes of amino acids near the redox centers and the electron pathway contribute to the spectra, whereas residues in the vicinity of the D- and the K-channel do not show any redox-dependent signal. Since the measurement was performed in a deoxygenated solution this finding is consistent with what is expected.

The model of sequential ET was used to analyze the time-dependence of some bands of the difference spectra which were attributed to the environments of single redox centers indicating their redox state. The results corroborate the conclusion drawn in context of fast scan voltammetry.

All attempts to investigate ET to non-activated CcO by means of electrochemically induced tr-SEIRAS at different potential ranges and frequencies failed. The reason for this is not yet known.

Activated CcO under aerobic conditions was also investigated by means of tr-SEIRAS at different oxygen concentrations, frequencies and potential windows. The results are rather puzzling, since the time-dependence of band areas does not show a periodic behavior which indicates non-stable conditions in the system.

## 8 Materials and Methods

### 8.1 Preparation of Samples

#### 8.1.1 Ultraflat Gold Surfaces: Template Stripped Gold

Monocrystalline Si Waver (CrysTec) have been used to fabricate ultraflat gold surfaces. The cut waver pieces were cleaned in a mixed solution of de-ionized (MilliQ) water,  $\text{NH}_3$  and  $\text{H}_2\text{O}_2$  (proportion 5:1:1). The solution with the wavers were then heated up to  $75^\circ\text{C}$  for 30 min. After being cooled down, the Si plates were taken out of the solution and rinsed with de-ionized water and ethanol. If the evaporation is not done immediately, the slides can be stored in ethanol. After having dried the pieces a gold layer of 50 nm was slowly evaporated onto the Si surfaces. Glas slides (LaSFN9 glass from Hellma Optik, Jena, refractive index  $n = 1.85$  at 633 nm) were cleaned with a 2% Hellmanex solution for 30 min in the ultrasonic bath. Afterwards they were rinsed with de-ionized water and ethanol. The dried glas slides were then glued with an epoxide resin (Polytec, EPO-TEK) onto the gold surfaces. The curing process of the glue was done for one hour at a temperature of  $140\text{-}150^\circ\text{C}$ . The glued plates were stored until needed for the experiment. The Si slides have been stripped off the glas slides. The ultraflat gold surface on the glas slide could then be used as an electrode.

#### 8.1.2 Two-Layer Gold Surface

The surfaces of silicon ATR crystals were polished by means of a polishing machine (Buehler PHOENIX 4000) using the polishing cloth TexMet P, VerduTex, and MicroCloth and MetaDi Supreme and polycrystalline diamond suspension, grain size 9  $\mu\text{m}$ , 3  $\mu\text{m}$ , and 1  $\mu\text{m}$ , in that order. After having polished the crystals, they were ultrasonically cleaned with ethanol for 15 min in order to remove the particles from the polish suspension. By means of electrothermal evaporation (Edwards FL 400) a thin (25 nm) gold film was deposited onto the flat surface of the ATR crystal. The gold film had a roughness of about  $R_q = 2$  nm. The evaporated crystal was immersed into 50 mL of an aqueous solution of hydroxylamine hydrochloride ( $\text{NH}_2\text{OH HCl}$ ) (0.4 mM) to which 500  $\mu\text{L}$  of an aqueous solution of gold (III) chloride hydrate (0.3 mM) was added. After two min, the same amount of  $\text{AuCl}_3$  solution was added. This process was repeated five times, so that the nano particles could grow for 10 min. After this procedure the crystals were removed from the growth solution, rinsed with water and dried with nitrogen [130].

#### 8.1.3 Immobilization of the Protein

The Dithiobis (nitriloacetic acid butylamidyl propionate) (short: DTNTA) that is used for functionalizing the gold electrodes was synthesized as described in an earlier publication [131]. CcO which is used here was expressed and purified from *Rhodobacter sphaeroides* and contained a his-tag which was engineered to the C-terminus of subunit II. The protein was kindly provided by the groups of Ferguson-Miller and Gennis. For a detailed description of the purification see literature [35]. Template stripped gold (TSG) electrodes which are used for surface plasmon resonance (SPR) and electrochemistry investigations were immersed for 24 hrs in a solution in dry DMSO of DTNTA and dithiobis (propionic acid) (DTP) mixed at a mole ratio of 0.2 (total concentration 10 mM). After the gold surface was rinsed with DMSO and dried, the slides were immersed for 30 min in 40 mM  $\text{NiSO}_4$

in acetate buffer (50 mM, pH = 5.5) followed by thorough rinsing with de-ionized water pH = 5 to remove the excess NiSO<sub>4</sub>. CeO dissolved in dodecyl β-D-maltoside(DDM)-phosphate-buffer(K<sub>2</sub>HPO<sub>4</sub> 0.05 M, KCl 0.1 M, pH = 8, 0.1 %DDM) was adsorbed onto the NTA-functionalized surface at a final concentration of 10 nM. After approximately 40 min of adsorption the cell was rinsed with DDM-phosphate buffer. A 40 μM DiPhyPC solution in a DDM-phosphate buffer was added. Membrane formation was enabled by in-situ dialysis which was performed by adding biobeads (Bio-Rad Laboratories GmbH, Munich, Germany) to the lipid-detergent solution. Each kind of measurement was not done before 48 hrs of membrane reconstitution.

For the measurements under aerobic conditions a fresh oxygen-saturated buffer solution (K<sub>2</sub>HPO<sub>4</sub> 0.05 M, KCl 0.1 M, pH = 8, flushed with oxygen) was used. The same buffer solution being flushed with argon instead of oxygen and containing an oxygen trap which consisted of glucose (3 mg/ml), glucose oxidase (27 μg/ml) and catalase (2.7 μg/ml) was used for measurements under anaerobic conditions.

## 8.2 Measuring Cells, Setups and Methods

### 8.2.1 Surface Plasmon Resonance

SPR measurements in the Kretschmann-configuration were performed with a measuring cell which was designed for the use of SPR in a combination with electrochemistry (see figure 8.1). The glass slide (LaSFN9 glass from Hellma Optik, Jena, refractive index  $n = 1.85$  at 633 nm) which was used to build the ultraflat gold surface (TSG) was optically matched to the base of a  $90^\circ$  glass prism (LaSFN9). The monochromatic light of a HeNe Laser (Uniphase, San Jose, CA,  $\lambda = 632.8$  nm) has been directed through the prism, coupled into the sample and collected by a custom made photodiode detector. Angle scans have been performed in order to ascertain the angle position of the plasmon. By means of the program Winspall, the scans could be fitted and layer thicknesses could be ascertained. Additionally the reflectivity has been traced at a fixed angle of incidence. The position of this angle was located in the linear branch of the angle scan (In our measurements, we have chosen an angle of  $\approx 54.7^\circ$ ). The kinetics of the adsorption of the protein and reconstitution could be traced in this way. In figure 8.3 the entire SPR setup is demonstrated.

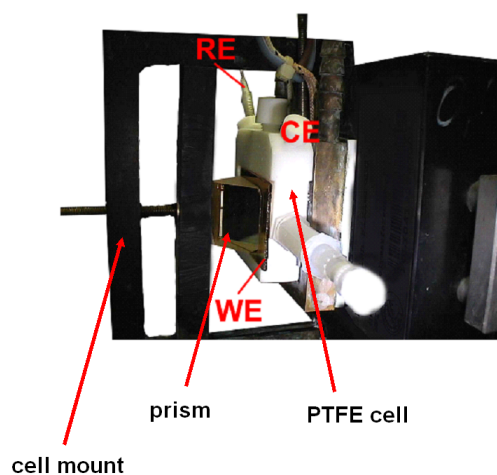


Figure 8.1: Measuring cell for SPR and electrochemical investigations. [81]

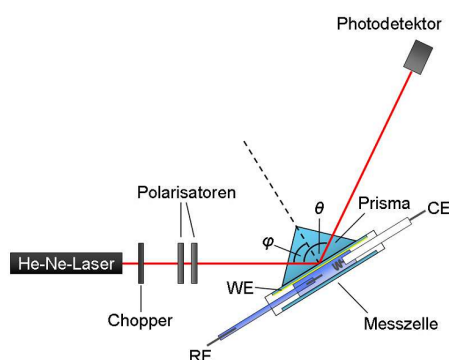


Figure 8.2: Scheme from above of SPR setup with measuring cell. [81]

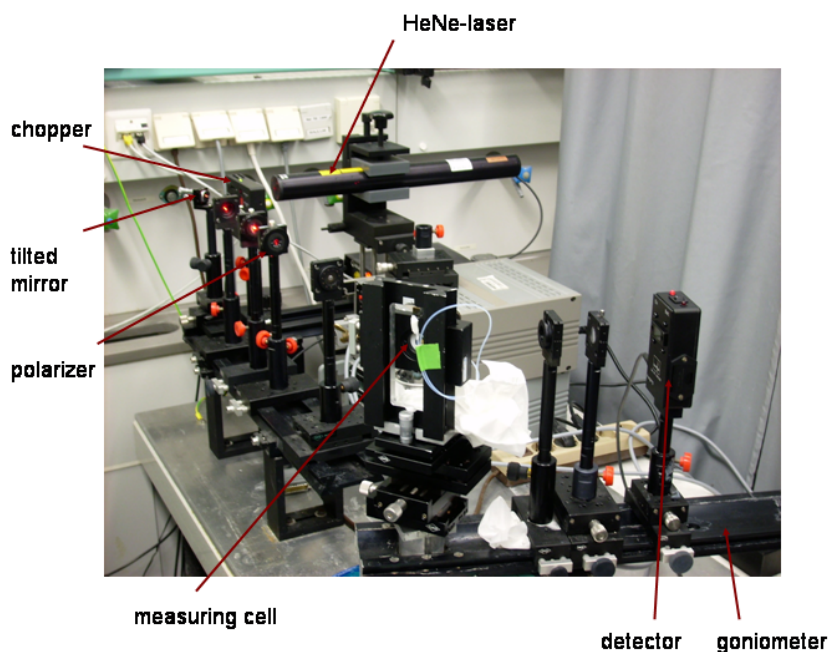


Figure 8.3: SPR setup

### 8.2.2 Electrochemistry

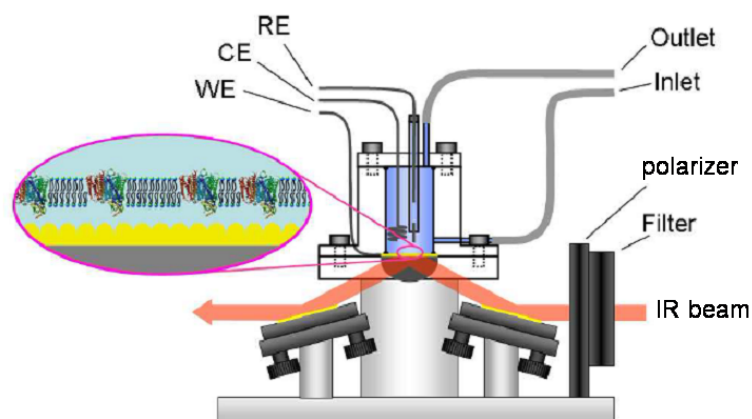
The electrochemical measurements have been performed using the same cell as for the SPR measurements (see figure 8.1). A three electrode configuration with TSG as the working electrode, a  $\text{Ag}|\text{AgCl}, \text{KCl}_{\text{sat}}$  reference, and a platinum wire as the counter electrode have been applied. In general, the electrode potentials are quoted versus SHE ( $E_{\text{SHE}} = E_{\text{Ag}|\text{AgCl}} + 0.197 \text{ V}$ ). For these investigations an Autolab instrument (PGSTAT302) equipped with an FRA2-module for impedance measurements, an ECD-module amplifier for low-currents, an ADC750 module for rapid scan measurements and a SCAN-GEN module for analog potential scanning have been employed. EIS data were recorded in the range of 0.1 MHz - 2 mHz with an excitation amplitude of 10 mV and a bias potential of 0 V against an  $\text{Ag}|\text{AgCl}, \text{KCl}_{\text{sat}}$  reference electrode. Data were analyzed by the complex nonlinear fitting algorithm supplied in the data processing software ZVIEW (Version 2.6, Scribner Associates, Inc.). CV was done with IR drop compensation, particularly at high scan rates.

### 8.2.3 Spectro-Electrochemistry

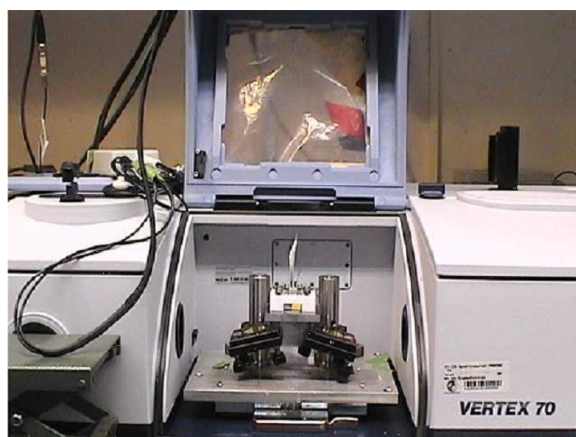
The spectro-electrochemical measurements have been performed using a particular custom made cell (see setup in figure 4(a) and 4(b)). This cell was mounted on top of a trapezoid silicon ATR-crystal (see figure 5(a)) which has been required for a single reflection in the Attenuated Total Reflection Spectroscopy (ATR) mode [129]. The IR beam of an FTIR spectrometer (VERTEX 70 FTIR spectrometer, from Bruker, Karlsruhe) was coupled into the prism at an angle of incidence  $\Theta = 60^\circ$ . The total reflected beam IR intensity was measured with a photovoltaic MCT (mercury cadmium telluride) detector. For potentiostatic titrations the ATR-FTIR setup was equipped with a function



generator which triggered the potentiostat of the Autolab (PGSTAT302) (Eco Chemie, B.V., Utrecht, Netherlands) as well as the spectrometer. [131] Electrochemical measurements were taken in a three electrode configuration with gold as the working electrode, a  $\text{Ag}|\text{AgCl}, \text{KCl}_{\text{sat}}$  reference, and a platinum wire as the counter electrode (see figure 5(b)). All electrode potentials are quoted versus SHE. Spectra were analyzed using the software package OPUS 6 (Bruker Optics GmbH; Ettlingen). [131]

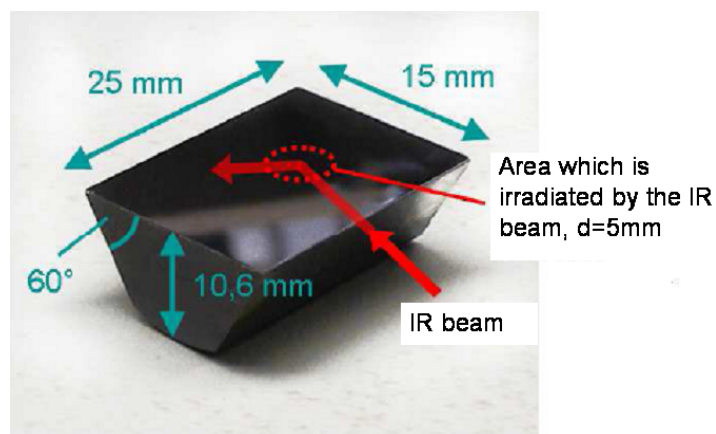


(a)

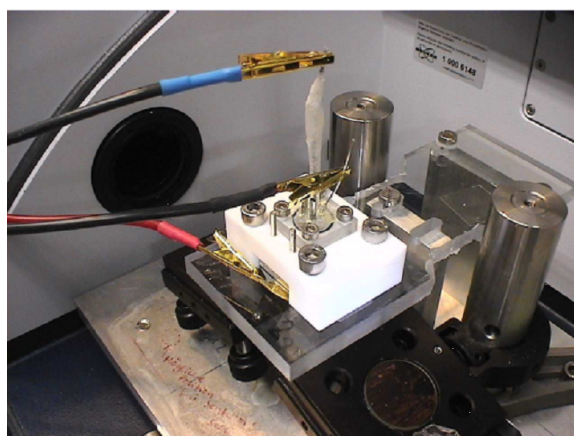


(b)

Figure 8.4: Scheme (a) and photograph (b) of the cell being integrated into the IR setup. [81]



(a)



(b)

Figure 8.5: Silicon ATR crystal (a) and measuring cell with three-electrode configuration (b). [81]

### 8.2.3.1 Time-Resolved (tr) Surface-Enhanced IR Absorption Spectroscopy (SEIRAS)

The ATR-FTIR spectrometer has been connected to a function generator which triggered the potentiostat of the Autolab as well as the spectrometer (see figure 8.6). The step-scan mode has been applied which was controlled by electrochemical excitation. Periodically alternating potentials between -0.8 (fully reduced state of the enzyme) and 0.4 V vs. SHE (fully oxidized state of the enzyme) in a square wave function were applied to the ptBLM on the gold WE. A sudden potential change at the start of each period triggers the tr FTIR measurements. The time-dependent evolution of spectra is recorded indicating the kinetics of the redox transition. The band area of peaks generated by single vibrational modes was obtained from integration. A voigt profile has been used (convolution of 80% Gaussian and 20% Lorentzian band shape) to fit the bands. Therefore a routine included in the OPUS 6 software has been applied. Excitation frequencies between 1 kHz and 10 Hz have been used in the step scan mode, applying 500 coadditions at a time resolution of 1  $\mu$ s. All spectra have been recorded using parallel polarized light.

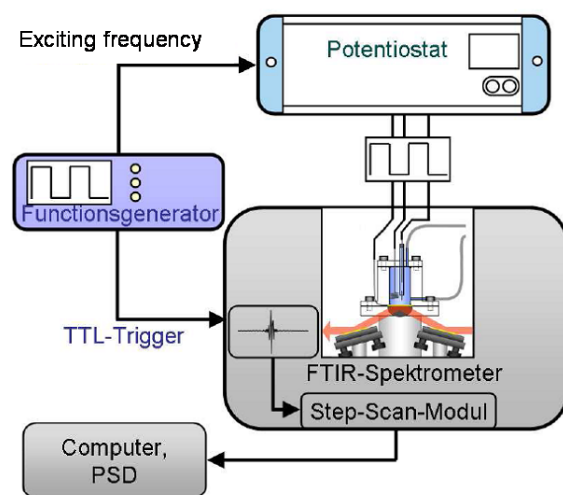


Figure 8.6: Scheme of FTIR Setup. [81]

### 8.3 Chemicals

- ammonia,  $\text{NH}_3$ : 28% [Sigma]
- argon, Ar: purity 6.0 [Westfalen AG, Münster]
- catalase: from bovine liver [Sigma Aldrich]
- detergent, DDM, n-Dodecyl- $\beta$ -D-maltoside: 98% [Sigma Aldrich]
- di-potassium phosphate,  $\text{K}_2\text{HPO}_4$ : [Fluka]
- ethanol: absolut, 99,8 Vol.% [Sigma Aldrich]
- glucose, D-(+)-Glucose: 99,5% [Sigma Aldrich]
- glucose-oxidase (GOX): from *Aspergillus Niger*, 60% [Sigma Aldrich]
- gold: gold granules 99,99% [ESG Edelmetall Service GmbH&Co. k]
- gold(III) chloride hydrate 99.999%,  $\text{AuCl}_3 \cdot \text{H}_2\text{O}$  [Sigma Aldrich]
- hydrochloric acid, HCl: 37% [VWR]
- hydrogen peroxide,  $\text{H}_2\text{O}_2$ : 35% [Riedel de Hæn]
- hydroxylamine hydrochloride 99%,  $\text{NH}_2\text{OH HCl}$  [Sigma Aldrich]
- lipid, DiphyPC, 1,2 Diphytanoyl-sn-Glycero-3-Phosphocholine: [Avanti Polar Lipids]
- 2 mercaptoethanol: 99% [Acros]
- nitrogen,  $\text{N}_2$ : purity 4 [Westfalen AG, Münster]
- potassium carbonate,  $\text{K}_2\text{CO}_3$ : 99,0% [Sigma Aldrich]
- potassium chloride, KCl: 99% [Sigma Aldrich]
- potassium dihydrogen phosphate,  $\text{KH}_2\text{PO}_4$  [Sigma Aldrich]
- sodium chlorate,  $\text{NaClO}_4$  [Sigma Aldrich]
- water: MilliQ

#### 8.4 Materials and Machines

- biobeads: SM-2 Adsorbent, 20-50 mesh [Bio-Rad]
- chopper: 197 [EG&G]
- epoxid glue: TSG EPO-TEK, Ratio 1:10 [Polytec]
- evaporation machine: fl 400, auto 306 [Edwards]
- function generator: 33250A 80MHz Function/Arbitrary waveform Generator [Agilent], 20 MHz 8021 [Tabor Electronics]
- glas slides: BK 7, n=1,5 pure white [Menzel]
- goniometer: [Huber]
- hellmanex II (detergent solution): 2 Vol% [Hellma]
- impedance analysor: SI 1260 impedance/gain-phase analyser [Schlumberger]
- laser: ionpure plasma tube Innova 90 (Kr laser) ( $\lambda=413\text{nm}$ ) [Coherent]; HeNe Laser 15 mW LGK7628, Q4001-K7656 ( $\lambda=632,8\text{nm}$ ) [Siemens]
- lock-in amplifier: 5210 [EG&G]
- magnet sticks: MR 3001 K [Heidolph]
- O-rings: Viton [Rheinwerkzeug]
- pH-meter: 766 Calimatic [Knick]
- platinum wire: 99,99%, Diameter 0,8 mm [Goodfellow]
- acrylic glass : [Cadillac Plastic 's]
- polarisator: [Fa. Halle]
- polishing machine: Phoenix 400 [Buehler]
- polishing fluid: diamond solution, MetaDi Supreme 9  $\mu\text{m}$ , 3  $\mu\text{m}$ , 1  $\mu\text{m}$  [Buehler]
- polishing pads: TexMetP, VerduTex, Microcloth [Buehler]
- potentiostat: potentiostat/galvanostat AutolabPGSTAT302 [Eco Chemie, B.V., Utrecht, Netherlands]
- pre-monochromator: Laserspec III [Spectrolab Research Laboratory, Newbury England]
- prism (SPR): LaSFN-9, refractive index n=1,845
- silica ATR-crystals (SERRS): [Korth Kristalle GmbH]
- silver wire: diameter 1,0 mm, 99,99% [Chempur]
- silica waver: cut, p-Type (B) [CrysTec]

- scanning electron microscope: 1530 Gemini, low voltage, high resolution scanning electron microscope; accelerating voltages: 100V to 30kV, resolution: 4nm@1kV [Leo]
- PTFE: [Cadillac Plastics]
- ultrasonic bath: Super RK510 H [Sonorex]
- vortex machine: Reax 2000 [Heidolph Instruments GmbH]

## 9 Symbols

- A: amplitude, absorbance, active surface area [ $\text{cm}^2$ ]
- $\alpha$ : CPE-P value, position of activation barrier
- $\alpha'$ : Napier's absorption coefficient
- $B(\tilde{\nu})$ : Fourier coefficient
- C: capacitance [F]
- $c/\Gamma$ : protein surface concentration [ $\text{cm}^{-2}$ ]
- $c_0$ : velocity of light in vacuum
- d: distance [cm, m], layer thickness [nm]
- $d_p$ : penetration depth [nm]
- $\Delta E_{\text{ps}}$ : peak separation [V]
- $\Delta\tilde{\mu}_{\text{H}^+}$ : difference of chemical energy
- $\delta$ : optical pathway
- E: potential [V], energy [J]
- $E_o$ : redox potential [V]
- $E_p$ : peak potential [V]
- $\epsilon$ : dielectric constant
- $\epsilon(\nu)$ : extinction coefficient
- $\epsilon_0$ : electric permittivity in vacuum [ $8,854 \cdot 10^{-12} \text{ C}^2\text{J}^{-1}\text{m}^{-1}$ ]
- F: Faraday constant [ $96\,485.339\,9 \text{ C} \cdot \text{mol}^{-1}$ ], force [N]
- G: Gaussian band shape / function
- g: enhancement coefficient
- $\Gamma/c$ : protein surface concentration [ $\text{cm}^{-2}$ ]
- H: Hamiltonian
- h: Planck constant [ $6.626 \cdot 10^{-34} \text{ J} \cdot \text{s}$ ]
- I: intensity
- i: current [A]
- J: flow
- j: current density [ $\text{A cm}^{-1}$ ]

- 
- k: Boltzmann constant [ $1,3806505 \cdot 10^{-23}$  J/K], wave vector, electrochemical rate constant [ $s^{-1}$ ]
  - L: Lorentzian band shape / function
  - l: quantum number (subshell)
  - $\lambda$ : wavelenght [cm]
  - M: molecular weight [ $g \cdot mol^{-1}$ ]
  - m: weight [g, kg]
  - N: mole number
  - $N_A$ : Avogadro constant [ $6.022 \cdot 10^{23}$  mol $^{-1}$ ]
  - n: refractive index, number of electrons
  - $\nu$ : frequency [ $s^{-1}$ ], scan rate [ $V \cdot s^{-1}$ ]
  - $\tilde{\nu}$ : wavenumber [ $cm^{-1}$ ]
  - $\omega$ : angular frequency [ $s^{-1}$ ]
  - p: impulse, probability
  - $\Phi$ : potential [V], phase shift [ $^\circ$ ]
  - Q: charge [C]
  - $\theta$ : angle [ $^\circ$ ]
  - R: reflectivity ; ohmic resistance [ $\Omega$ ] ; molar gas constant [ $8,31441$  Jmol $^{-1}$ K $^{-1}$ ]
  - $\sigma$ : cross section [ $cm^2$ ], charge density [ $C \cdot m^{-3}$ ]
  - T: (absolute) temperature [ $C^\circ$ ] (absolute [K]), transmission
  - t: time [s]
  - $\tau$ : relaxation time [s]
  - u: reduced mass
  - V: Voigt band shape / function
  - x: direction parameter, mole fraction
  - Y: admittance
  - Z: impedance
  - z: valence number



## 10 Acronyms and Abbreviations

- ADP: adenosindiphosphate
- AFM: atomic force microscopy
- ANTA: amino-nitrilotriacetic acid,  $N_{\alpha}'$ ,  $N_{\alpha}''$ -bis(carboxymethyl)-L-lysin
- ATP: adenosintriphosphate
- ATR: attenuated total reflectance
- a.u.: arbitrary unit
- BLM: bilayer lipid membrane
- CAT: catalase
- Cc: Cytochrome c
- CcO: Cytochrome c Oxidase
- CE: counter electrode
- CL: cardiolipin
- CPE: constant phase element
- CV: cyclic voltammogram (in some cases cyclic voltammetry)
- Cyt c: Cytochrome c
- DDM: dodecylmaltoside
- DMSO: dimethylsulfoxyde
- DNA: deoxyribonucleic acid
- DPhyPC: 1,2-diphytanyl-sn-glycero-3-phosphocholin
- DTP: dithio-bis-propionate
- DTSP: dithio-bis-(succinimidyl-propionate)
- EC: electrochemical, electrochemistry
- ECCC: chain of electrochemical reaction followed by three chemical reactions
- EEEE: chain of electrochemical reaction followed by three electrochemical reactions
- EIS: electrical impedance spectroscopy
- EM/SEM/TEM: electron microscope / scanning electron microscope / transmission electron microscope
- EPR: electron paramagnetic resonance

- 
- ET: elektron transfer
  - FTIRA(S): Fourier-transform infrared absorption (spectroscopy)
  - GOX: glucose-Oxidase
  - His-Tag: histidin anchor
  - IR-: infrared
  - kD: [kilo Dalton]
  - LOC: lab-on-a-chip
  - NADH: nicotinamidadenindinukleotid
  - NHE/SHE: normal hydrogen electrode / standard hydrogen electrode
  - NMR: nuclear magnetic resonance
  - NP: nano particle
  - NTA: nitrilotriacetic acid
  - PBS: phosphate buffered saline
  - PDB: protein data bank
  - ptBLM: protein-tethered bilayer lipid membrane
  - QCM: quarz micro balance
  - RE: reference electrode
  - RR: resonance-Raman
  - r.t.: room temperature
  - SAM: self-assembled monolayer
  - sBLM: solid-supported bilayer lipid membrane
  - SEIRAS: surface-enhanced infrared absorption spectroscopy
  - SER(R)S: surface-enhanced (resonance) Raman spectroscopy
  - SNR / SRV: signal to noise ratio
  - SPR: surface plasmon resonance
  - SU: subunit
  - tBLM: tethered bilayer lipid membrane
  - TSG: template stripped gold
  - tr: time-resolved
  - UV-vis: ultraviolet-visible
  - WE: working electrode

## **11 Appendix**

### **.1 Curriculum Vitae**

## .2 List of Publications

C. Nowak & **D. Schach**, V. U. Kirste, J. Zhu, R. B. Gennis, D. Baurecht, D. Walz, W. Knoll, R. L. C. Naumann, *Time-Resolved Surface-Enhanced IR-Absorption Spectroscopy of direct Electron Transfer into Cytochrome c Oxidase*, in preparation

**D. Schach**, M. Grosserüschkamp, C. Nowak, W. Knoll, R. Naumann, *Spectro- Electrochemical Investigation of the bc1 Complex from the yeast Saccharomyces cerevisiae using Surface Enhanced B-Band Resonance Raman Spectroscopy*, book chapter at InTech (title: "Advances in Biomimetics"), in press

C. Nowak, M. G. Santonicola, **D. Schach**, J. Zhu, R. B. Gennis, D. Baurecht, D. Walz, W. Knoll, R. L. C. Naumann, *Conformational Transitions and Molecular Hysteresis of Cytochrome c Oxidase: Varying the Redox State by Electronic Wiring*, SoftMatter, 2010

**D. Schach**, C. Nowak, R. Gennis, S. Ferguson-Miller, W. Knoll, D. Walz, R. Naumann, *Modeling Direct Electron Transfer to a Multi-Redox Center Protein: Cytochrome c Oxidase*, Journal of Electroanalytical Chemistry, 2010

C. Nowak, **D. Schach**, J. Gebert, M. Grosserueschkamp, R. B. Gennis, S. Ferguson-Miller, W. Knoll, D. Walz, R. L. C. Naumann, *Oriented immobilization and electron transfer to the cytochrome c oxidase*, Journal of Solid State Electrochemistry, 2010

C. Nowak, **D. Schach**, M. Grosserueschkamp, W. Knoll, R. L. C. Naumann, *Cytochrome C as a benchmark system for a two-layer gold surface with improved surface-enhancement for spectro-electrochemistry*, Spectroscopy, 24, 2010

M. Grosserueschkamp, C. Nowak, **D. Schach**, W. Schaertl, W. Knoll, R. L. C. Naumann, *Silver Surfaces with Optimized Surface Enhancement by Self-Assembly of Silver Nanoparticles for Spectroelectrochemical Applications*, Journal of Physical Chemistry C, 113, 2009

C. Nowak, C. Luening, **D. Schach**, D. Baurecht, W. Knoll, R. L. C. Naumann, *Electron Transfer Kinetics of Cytochrome C in the Submillisecond Time Regime Using Time-Resolved surface-Enhanced Infrared Absorption Spectroscopy*, Journal of Physical Chemistry C, 113, 2009

## List of Figures

3.1	Scheme of a cell membrane.[203] . . . . .	7
3.2	Scheme of the phospholipid structure.[138] . . . . .	8
3.3	Cristae-type mitochondrion and synapse (cortex cerebri, rat), kindly provided by Dr. med. H. Jastrow. . . . .	9
3.4	Respiratory chain of mitochondria.[72] . . . . .	10
3.5	Scheme of the potential-driven redox cascade in the respiratory chain.[152]	11
3.6	3-Dimensional illustration of SU I and II of cytochrome c oxidase viewed parallel to the membrane. Additional SUs are excluded. [203] . . . . .	12
3.7	Catalytic cycle of Cytochrome c Oxidase. Only heme $a_3$ (Fe) and $Cu_B$ of the catalytic center are shown and proton pumping is omitted.[15] . . . . .	14
3.8	Simplified scheme of the catalytic cycle performed by CcO. This was suggested by Wikström in 1989.[158] . . . . .	15
3.9	Modified scheme of the catalytic cycle performed by CcO. This was suggested by Michel in 1998.[158] . . . . .	16
3.10	Latest model for the catalytic cycle performed by CcO. This was suggested by Wikström in 2000.[158] . . . . .	17
3.11	Possible ET pathways in CcO. Solid black lines indicate the pathways mediated by covalent bonds, the dashed black lines indicate the pathways mediated by hydrogen bonds or through space jumps. Thin and thick colored lines indicate bonds of residues and the heme groups, respectively. The metal atoms are shown as van-der-Waals spheres colored by atom name. [143] . . . . .	18
3.12	Scheme of SU I and II of CcO from <i>Paracoccus denitrificans</i> . The electron pathway (green) and both proton transfer pathways are marked (blue). The D-pathway starts at Asp <sup>124</sup> and leads via several polar residues to Glu <sup>278</sup> . The K-pathway passes Ser <sup>291</sup> , Lys <sup>354</sup> , Thr <sup>351</sup> , Tyr <sup>281</sup> . [158] . . . . .	20
4.1	Scheme of the in-situ dialysis of CcO. In the first preparation step (left) the detergent solubilized CcO is attached via His-tag to the functionalized surface in a strict orientation. The ultraflat gold surface (TSG) has been functionalized with NTA-Ni <sup>2+</sup> ex-situ, before. With the help of biobeads, the in-situ dialysis takes place and the lipid micelles made from detergent-solubilized lipids assemble into a bilayer phase around the proteins during ~ 48 h (right).[134] . . . . .	22
5.1	Optical path of incident, transmitted and reflected light beam at the interface of two media with different refractive indices $n_1$ and $n_2$ . . . . .	23
5.2	Optical path of incident and reflected light beam at the interface of a metal and a dielectricum. The excited surface plasmon decreases exponentially within the z-direction. . . . .	24
5.3	Dispersion relation of the surface plasmon and of the photon in air (1). There is no point of intersection for both curves. An arbitrary increase of the refractive index of the medium produces a point of intersection with only the both curves, but not the laser frequency (3). The choice of a distinct angle of incidence $\Theta_{\text{incid}}$ will evoke a common point of intersection (2). This condition is required for the resonant excitation of the surface plasmon.[96] . . . . .	25

---

5.4	Schematic coupling of prisms for excitation of surface plasmons in two possible configurations: Otto- (left) and Kretschmann-configuration (right).[159]	25
5.5	Angle scan of the reflectivity (left) before (solid line) and after (dashed line) the adsorption of an dielectric molecule layer on the surface. Kinetic trace (right), following the reflectivity at a fixed angle $\Theta^*$ in the course of time.[159]	26
5.6	Proposed model of double-layer region under conditions where anions are specifically adsorbed.	27
5.7	Time-dependence of potential $E(t)$ (red) and current response $i(t)$ (black). $\omega = 2\pi f$ where $f$ denotes the frequency, and $\phi$ is the phase shift.	29
5.8	Scheme of complex impedance.	30
5.9	Linear potential sweep with two reversal potentials $E_1$ and $E_0$ of a cyclic voltammogram.	32
5.10	Cyclic voltammogram with distinct shape. A reversible charge transfer takes place. $E_{p,a}$ : anodic peak, $E_{p,c}$ : cathodic peak, $E_0$ : redox potential, $E_1$ and $E_2$ : reversal potentials. $j_{p,a}$ : anodic peak current density, $j_{p,c}$ : cathodic peak current density. The non-faradaic (or capacitive) current and the faradaic current are shown in green and blue, respectively.	33
5.11	Scheme of the activation barrier at different transfer coefficients being an indicator for the symmetry of the barrier to reaction. The dashed line represents the shift in the curve for the reduction of the oxidized species as the potential is made more positive. [34]	35
5.12	Scheme of ptBLM with CcO being tethered via his-tag to a chelat complex at the linker molecule (DTNTA). The enzyme is embedded into a lipid bilayer membrane in a strict orientation (A). The approximate position of the prosthetic groups is shown in (B). $Cu_A$ is directed towards the electrode.	36
5.13	Scheme of two ET mechanisms towards the redox centers of CcO. (A) The sequential reduction follows the ECCC mechanism, where $Cu_A$ is electrochemically reduced by the electrode. A chemical reduction of the following redox centers by this particular electron takes place subsequently. Further three more electrons can be taken up in this way. (B) The independent ET to the protein, another possible mechanism, bases on the EEEE mechanism, in which each of the redox centers is reduced by the electrode separately.	38
5.14	Detailed description of sequential and independent ET.	40
5.15	Types of molecule excitations. [73]	42
5.16	Chemical bonds and their vibration types for different wavenumbers.[73]	43
5.17	Stretching and bending vibrational modes for $H_2O$ . [71]	44
5.18	Stretching and bending vibrational modes for $CO_2$ . [71]	44
5.19	Classical model for molecule stretching. The molecule consists of two atoms being connected by a backdriving spring force. [71]	45
5.20	Energy curve for a vibrating spring in the classical model (left) and the quantum mechanical model (right). [71]	47
5.21	Energy curve of an anharmonic oscillator. [71]	48
5.22	Example of a polypeptide chain.	50

---

5.23	Principle of a FTIR spectrometer. With the help of the Michelson interferometer the interferogram/spectrum can be recorded. Both are displayed for a monochromatic radiation source in this scheme. $\delta$ is the optical pathway between fixed and movable mirror. [12] . . . . .	51
5.24	Transmission and ATR configuration. $n_1$ and $n_2$ are the refraction indices for the crystal and the sample, respectively. D denotes the detector. [12] .	52
5.25	ATR crystal with multiple reflections.[12] . . . . .	53
5.26	Scheme of the mechanism for the infrared absorption enhancement at the metal surface (SEIRA).[20] . . . . .	54
5.27	Energy scheme of the mechanism of the enhancement effect.[20] . . . . .	55
5.28	Scheme of the step-scanning mirror. [180] . . . . .	56
5.29	Step scan technique: the scanning mirror is kept at a sampling position $x_n$ and the whole sequence of pulses is performed. The IR intensity is recorded for each time slide and predetermined number of pulses. Then the scanner steps to the next position $x_{n+1}$ and procedure is repeated. After having measured the entire range of retardation(i.e. wavenumbers), the time-dependent spectra are reconstructed by the computer software in order to achieve the interferograms corresponding to each time slide $I(t_i)$ . With the help of Fourier transformation the respective spectra can be obtained. The time resolution (i.e. $t_{RES}$ ) is limited by the response time of the detector. [55] . . . . .	57
5.30	Principle of tr-SEIRAS: Periodically alternating potential pulses in the form of square wave functions (top part) . The time-resolved record of FTIR spectra is triggered with the fast potential change at the start of each period (middle part). The band intensities indicating the kinetics of the redox transition as a function of time, are then plotted vs. time (bottom part). . . . .	58
5.31	Externally applied (red) and effective potential (green) caused by the charging effect of the electrode at high frequencies (400 Hz in this case). .	59
6.1	Bode (A) and Admittance plot (B) of the ptBLM at a mole fraction of 0.2 after (solid circles) protein adsorption and after membrane formation (solid triangles). The curves represent the result of fitting the equivalent circuit. . . . .	62
6.2	Equivalent circuit is fitted to the EIS data. . . . .	63
6.3	Capacitances (a) and resistances (b) of the system at mole fractions of 0.1, 0.2 and 0.3 before (shaded bar) and after membrane formation (empty bar). Corresponding change in capacitance (c) and resistance (d) at mole fractions of 0.1, 0.2 and 0.3 during the formation of the membrane. . . . .	64
6.4	CVs of CcO immobilized on an <i>ex-situ</i> functionalized ultraflat gold electrode at different mole fractions, x, 0.1 (blue), 0.2 (black), 0.3 (red), 0.4 (green) under aerobic and otherwise equal conditions. The inset shows the peak current densities for x = 0.1, 0.2, 0.3, 0.4. . . . .	65
6.5	CVs measured in the absence of oxygen thus excluding the proton transfer and concomitant oxygen reduction at mole fractions 0.1 (A), 0.2 (B) and 0.3 (C). This study focusses on the ET to CcO. The scans have been measured at scan rates of 0.05 (solid squares), 0.1 (solid circles), 0.2 (solid triangles), 0.4 (open squares) and 0.8 $Vs^{-1}$ (open circles). . . . .	66

---

6.6	Kinetic SPR trace of the adsorption (A-B) of proteins and membrane formation (C) for $x = 0.2$ and a fixed angle of $54.7^\circ$ . The Inset shows the SPR angle scans that have been performed before (A, black) and after protein adsorption (B, red) and after membrane formation (C, blue). . . . .	67
6.7	Cyclic voltammograms of CcO immobilized in a ptBLM via his-tag on subunit II under anaerobic conditions before activation, scan rates $/(V s^{-1})$ 0.05 (open squares), 0.1 (open circles), 0.2 (open triangles), 0.4 (solid squares), 0.8 (solid circles), 1 (solid triangles) taken at room temperature. . . . .	70
6.8	CVs of CcO on TSG immobilized with the His-tag attached to subunit II, under anaerobic (grey, right hand y-axis) and aerobic (black, left hand y-axis) conditions, both in the activated state measured at scan rate 50 mV/s. CV of CcO immobilized with the his-tag attached to subunit I (grey line and grey squares, right hand y-axis). . . . .	70
6.9	CVs of CcO taken under aerobic conditions at a scan rate of $0.05 V s^{-1}$ and at room temperature. The 1 <sup>st</sup> (red), 5 <sup>th</sup> (green), 10 <sup>th</sup> (dark blue), 15 <sup>th</sup> (light blue), 20 <sup>th</sup> (pink), 25 <sup>th</sup> (purple), 30 <sup>th</sup> (black) scan is displayed demonstrating the shift of the electron and proton peaks from more negative values to $-0.2 V$ and $-0.55 V$ , respectively (a). The peaks at $\approx 0.4 V$ which occurred under anaerobic conditions for non-activated CcO vanish with successive scans (b). . . . .	71
6.10	CVs of activated CcO under aerobic conditions at room temperature using a buffer solution which is not flushed (red) or flushed with oxygen (blue) taken at a scan rate of $0.05 V s^{-1}$ . The peak currents that are attributed to the electron and the proton transfer are enhanced with an increase of substrate $O_2$ . . . . .	72
6.11	CVs taken under anaerobic conditions after activation, scan rates $/(V s^{-1})$ 0.05 (open squares), 0.1 (open circles), 0.2 (open triangles), 0.4 (solid squares), 0.8 (solid circles), and 1 (solid triangles) taken at room temperature. . . . .	73
6.12	Comparison of CVs of activated (red, dark blue) and non-activated (brown, light blue) CcO under aerobic (light blue, dark blue) and anaerobic (brown, red) conditions taken at a scan rate of $0.05 V s^{-1}$ and at room temperature. The scans taken under aerobic conditions refer to the left scale (blue) and the scans taken under anaerobic conditions refer to the right scale (red). The peak at approximately $-0.2 V$ which was attributed to the ET in the case of activated CcO under aerobic conditions (blue) persists if changing to anaerobic conditions (red). . . . .	73
6.13	Experimental and simulated baseline-corrected and -normalized CVs of activated CcO. The CVs were taken under anaerobic conditions at $pH = 8$ and at scan rates 0.05 (A), 0.4 (B) and $2 V s^{-1}$ (C). The experimental data (solid circles), the simulated total current density (solid line) and the components resulting from $Cu_A$ (open squares), heme a (open circles), heme $a_3$ (open triangles), and $Cu_B$ (solid triangles) are plotted vs. the applied potential $E$ . The CVs have been simulated by means of the model of sequential ET. The fit parameters are listed in table 7. . . . .	76



---

6.14	Experimental and simulated CVs for non-activated CcO at pH 8. Baseline-corrected and $\nu$ -normalized CVs at scan rates 0.05 (A) and 0.2 V s <sup>-1</sup> (B). The experimental data (solid line), the simulated total current density (solid circles) and the components resulting from Cu <sub>A</sub> (solid triangles), heme a (open circles), heme a <sub>3</sub> (open triangles), and Cu <sub>B</sub> (open squares) are plotted vs. the applied potential E. CVs were simulated with the model of sequential ET and the fitted parameter values listed in table 9. . . . .	78
6.15	Tr-SEIRA spectra taken at 400 Hz under anaerobic conditions (pH = 8) in the range between 1200 and 1400 (a) and 1400 and 1550 (b) which is the fingerprint region. Difference spectra refer to oxidative (red) and reductive half period (black). . . . .	80
6.16	Tr-SEIRA spectra taken at 400 Hz under anaerobic conditions (pH = 8) in the range between 1550 and 1650 (a) and 1650 and 1750 (b) which is the amide region. Difference spectra refer to oxidative (red) and reductive half period (black). . . . .	81
6.17	Several important residues (green, labeled light blue) near the redox centers (Cu <sub>A</sub> (orange), the hemes (blue with red center) and Cu <sub>B</sub> (orange)) which have been assigned to some of the vibrational modes occurring in our spectra. . . . .	83
6.18	Plots of band area vs. time (full circles) for the bands at 1517 (A), 1603 (B) and 1693 cm <sup>-1</sup> (C) referring to the environment of Cu <sub>A</sub> . The plots were fitted by means of the model of sequential ET to CcO (red line). . .	87
6.19	Plots of band area vs. time (full circles) for the bands at 1529 (A) and 1666 cm <sup>-1</sup> (B) referring to the environment of heme a. The plots were fitted by means of the model of sequential ET to CcO (red line). . . . .	88
6.20	Plots of band area vs. time (full circles) for the bands at 1463 (A), 1638 (B) and 1677 cm <sup>-1</sup> (C) referring to the environment of heme a <sub>3</sub> . The plots were fitted by means of the model of sequential ET to CcO (red line). . .	89
6.21	Plot of band area vs. time (full circles) for the bands at 1476 cm <sup>-1</sup> referring to the environment of Cu <sub>B</sub> . The plot was fitted by means of the model of sequential ET to CcO (red line). . . . .	90
6.22	Tr-SEIRA spectra taken at 1 kHz under aerobic conditions (pH = 8) in the range between 1250 and 1500 (a) and 1500 and 1700 (b) which is the fingerprint and the amide region, respectively. Spectra refer to oxidative (blue) and reductive half period (black). . . . .	91
6.23	Band area vs. time plots for activated CcO under aerobic conditions measured at an exciting pulse frequency of 100 Hz and a mixing ratio Ar:O <sub>2</sub> of 8:2 (a) and 0:9 (b). Both bands at 1438 (a) and 1429 cm <sup>-1</sup> (b) could be assigned to the same vibrational mode of the Cu <sub>A</sub> environment. The irreversibility of the band areas seems to be dependent on the O <sub>2</sub> concentration and could indicate a constant change of the system, thus tr-SEIRAS is not applicable in this particular case. . . . .	92
8.1	Measuring cell for SPR and electrochemical investigations. [81] . . . . .	98
8.2	Scheme from above of SPR setup with measuring cell. [81] . . . . .	98
8.3	SPR setup . . . . .	99
8.4	Scheme (a) and photograph (b) of the cell being integrated into the IR setup. [81] . . . . .	100

## LIST OF FIGURES

---

8.5	Silicon ATR crystal (a) and measuring cell with three-electrode configuration (b). [81]	101
8.6	Scheme of FTIR Setup. [81]	102

**List of Tables**

1	Regions of the electromagnetic spectrum. . . . .	42
2	Net number of fundamental vibrations for two different molecule types. . .	44
3	Fit parameters: capacitance and resistance of the system at a molar fraction of 0.2 before and after membrane formation. . . . .	63
4	Averaged protein surface concentrations found for mole fractions $x = 0.1, 0.2, 0.3$ . Values for $x = 0.2$ were calculated with oxidative and reductive branch, whereas those for $x = 0.1$ and $0.3$ apply only to the reductive branch. . . . .	67
5	Thickness of layers in the ptBLM determined by SPR. . . . .	68
6	Surface coverages and scaling factors $f_p$ for activated CcO at different scan rates with $\Gamma_0 = 6 \text{ pmol cm}^{-2}$ . . . . .	74
7	Parameter values obtained by fitting different ET models to the CVs of activated CcO. Values that contain uncertainties indicated by $\pm$ are fitted, whereas values without uncertainties are fixed in the fitting procedure. Note that in the 3 <sup>rd</sup> column $\Delta E_{ps}$ was fixed and $k_{e,1}$ was fitted while in the 4 <sup>th</sup> column $\Delta E_{ps}$ was fitted and $k_{e,1}$ was fixed. red and ox denote the reductive and the oxidative branch of the CV, respectively. . . . .	75
8	Surface concentration $\Gamma$ and scaling factor $f_p$ for non-activated CcO with $\Gamma_0 = 12 \text{ pmol cm}^{-2}$ . Red and ox refer to the reductive (cathodic) and oxidative (anodic) branch of CVs, respectively. . . . .	77
9	Parameter values obtained by fitting the sequential ET model to the CVs of non-activated CcO. Values that contain uncertainties indicated by $\pm$ are not fixed, whereas values without uncertainties are fixed in the fitting procedure. Only experimental data within the range of E indicated by limits were included. . . . .	77
10	Low wavenumber-band position (1 <sup>st</sup> column) and redox state (2 <sup>nd</sup> column) found experimentally. Tentative band assignments according to [184] and [123] (latter marked with *). Redox states marked with n.d. were not defined. Wavenumber of bands (3 <sup>rd</sup> column), redox state (4 <sup>th</sup> column) and environments assigned to redox centers (5 <sup>th</sup> column) found from literature. Wavenumbers given in bold denote bands which have been further analyzed. Bands in the spectra without assignment have not yet been reported in the literature. . . . .	85
11	High wavenumber-band positions (1 <sup>st</sup> column) and redox state (2 <sup>nd</sup> column) found experimentally. Tentative band assignments according to [184] and [123] (latter marked with *). Redox states marked with n.d. were not defined. Wavenumber of bands (3 <sup>rd</sup> column), redox state (4 <sup>th</sup> column) and environments assigned to redox centers (5 <sup>th</sup> column) found from literature. Wavenumbers given in bold denote bands which have been further analyzed. Bands in the spectra without assignment have not yet been reported in the literature. . . . .	86
12	Parameter values obtained by fitting the sequential ET model to the time-dependence of band areas (see figures 6.18, 6.19, 6.20 and 6.21) for activated CcO. Values that contain uncertainties indicated by $\pm$ are fitted, whereas values without uncertainties are fixed in the fitting procedure. . .	88

LIST OF TABLES

---

13  $\Delta A$  (3<sup>rd</sup> column) and  $A_0$  (4<sup>th</sup> column) (see equation 5.86) referring to the bands (1<sup>st</sup> column) that have been analyzed to study the redox kinetics of the redox centers (2<sup>nd</sup> column). . . . . 90

## References

- [1] P. Brzezinski; P. Adelroth. Pathways of proton transfer in cytochrome c oxidase. *J. Bioenerg. Biomembr.*, 30(1):99–107, Feb 1998.
- [2] L. Powers; B. Chance; Y. Ching; P. Angiolillo. Structural features and the reaction mechanism of cytochrome oxidase: iron and copper X-ray absorption fine structure. *Biophys. J.*, 34(3):465–498, Jun 1981.
- [3] C. Léger; S.J. Elliott; K.R. Hoke; L.J.C. Jeuken; A.K. Jones; F.A. Armstrong. Enzyme electrokinetics: using protein film voltammetry to investigate redox enzymes and their mechanisms. *Biochemistry*, 42(29):8653–8662, Jul 2003.
- [4] F. A. Armstrong. Insights from protein film voltammetry into mechanisms of complex biological electron-transfer reactions. *J. Chem. Soc. Dalton*, 5:661–671, 2002.
- [5] F. A. Armstrong. Protein Film Voltammetry: Revealing the Mechanisms of Biological Oxidation and Reduction. *Russ. J. Electrochem.*, 38:49–62, 2002.
- [6] L.J.C. Jeuken; A.K. Jones; S.K. Chapman; G. Cecchini; F.A. Armstrong. Electron-transfer mechanisms through biological redox chains in multicenter enzymes. *J. Am. Chem. Soc.*, 124(20):5702–5713, May 2002.
- [7] R. Aroca. *Surface-Enhanced Vibrational Spectroscopy*. Wiley, 2006.
- [8] S. Ferguson-Miller; G.T. Babcock. Heme/Copper Terminal Oxidases. *Chem. Rev.*, 96(7):2889–2908, Nov 1996.
- [9] J. Darnell; H. Lodish; D. Baltimore. *Molecular Cell Biology (international student edition)*; *Scientific American Books*. W.H. Freeman & Co. Ltd. New York., 1986.
- [10] S. Krimm; J. Bandekar. Vibrational spectroscopy and conformation of peptides, polypeptides, and proteins. *Adv. Protein. Chem.*, 38:181–364, 1986.
- [11] A. Barth. The infrared absorption of amino acid side chains. *Progress in Biophys. and Molecular Biol.*, 74(3-5):141–173, 2000.
- [12] D. Baurecht. lecture notes, Biophysik I: Aufbau und Strukturanalyse von Biomolekülen, Institut für Biophysikalische Chemie. Uni Wien, 2006.
- [13] R.H. Sands; H. Beinert. On the function of copper in cytochrome oxidase. *Biochem. Biophys. Res. Commun.*, 1:175–179, 1959.
- [14] B. Michel; H. R. Bosshard. Spectroscopic analysis of the interaction between cytochrome c and cytochrome c oxidase. *J. Biol. Chem.*, 259(16):10085–10091, Aug 1984.
- [15] K. Budiman. *Spektroskopische Charakterisierung von Intermediaten der Cytochrom c Oxidase von Paracoccus denitrificans*. PhD thesis, Johann Wolfgang Goethe Universität, Frankfurt am Main, 2006.
- [16] R.A. Capaldi. Structure and Function of Cytochrome c Oxidase. *Ann. Rev. Biochem.*, 59:569–596, 1990.

## REFERENCES

---

- [17] R.A. Scott; P.M. Li; S.I. Chan. The binuclear site of cytochrome c oxidase. Structural evidence from iron X-ray absorption spectroscopy. *Ann. N. Y. Acad. Sci.*, 550:53–58, 1988.
- [18] T.H. Stevens; C.T. Martin; H. Wang; G.W. Brudvig; C.P. Scholes; S.I. Chan. The nature of CuA in cytochrome c oxidase. *J. Biol. Chem.*, 257(20):12106–12113, Oct 1982.
- [19] T.H. Stevens; S.I. Chan. Histidine is the axial ligand to cytochrome alpha 3 in cytochrome c oxidase. *J. Biol. Chem.*, 256(3):1069–1071, Feb 1981.
- [20] G.I. Dovbeshko; O.M. Fesenko; Yu.M. Shirshov; V.I. Chegel. The enhancement of optical processes near rough surface of metals. *Semiconductor Physics, Quantum Electronics & Optoelectronics.*, 7:411–424, 2004.
- [21] S. Tan; H. T. Tan; M.C.M. Chung. Membrane proteins and membrane proteomics. *Proteomics*, 8(19):3924–3932, Oct 2008.
- [22] D. Schach; C. Nowak; R.B. Gennis; Sh. Ferguson-Miller; W. Knoll; D. Walz; R.L. C.Naumann. Modeling direct electron transfer to a multi-redox center protein: Cytochrome c oxidase. *J. Electroanal. Chem.*, 649:268–276, 2010.
- [23] S.R. Lynch; R.H. Carter; R.A. Copeland. Resonance Raman spectroscopy of the cytochrome c oxidase from *Paracoccus denitrificans*. *Biochemistry*, 32(27):6923–6927, Jul 1993.
- [24] R.A. Capaldi; F. Malatesta; V.M. Darley-Usmar. Structure of cytochrome c oxidase. *Biochim. Biophys. Acta*, 726(2):135–148, Jul 1983.
- [25] P.R. Cullis; B. de Kruijff. Lipid polymorphism and the functional roles of lipids in biological membranes. *Biochim. Biophys. Acta*, 559(4):399–420, Dec 1979.
- [26] R. Ramharack ; R.G. Deeley. Structure and evolution of primate cytochrome c oxidase subunit II gene. *J. Biol. Chem.*, 262(29):14014–14021, Oct 1987.
- [27] T.H. Haines; N.A. Dencher. Cardiolipin: a proton trap for oxidative phosphorylation. *FEBS Lett.*, 528(1-3):35–39, Sep 2002.
- [28] C. Le Moigne; B. Schoepp; S. Othman; A. Verméglio; A. Desbois. Distinct structures and environments for the three hemes of the cytochrome bc1 complex from *Rhodospirillum rubrum*. A resonance Raman study using B-band excitations. *Biochemistry*, 38(3):1066–1076, Jan 1999.
- [29] T. Lichtor; G.J. Dohrmann. Respiratory patterns in human brain tumors. *Neurosurgery*, 19(6):896–899, Dec 1986.
- [30] J. A. Bailey; F. L . Tomson; S. L. Mecklenburg; G. M. MacDonald; A. Katsonouri; A. Puustinen; R. B. Gennis; W. H. Woodruff; R. B. Dyer. Time-Resolved Step-Scan Fourier Transform Infrared Spectroscopy of the CO Adducts of Bovine Cytochrome c Oxidase and of Cytochrome bo3 from *Escherichia coli*. *Biochemistry*, 41(8):2675–2683, 2002.

## REFERENCES

---

- [31] K.E. Georgiadis; N.I. Jhon; O. Einarsdóttir. Time-resolved optical absorption studies of intramolecular electron transfer in cytochrome c oxidase. *Biochemistry*, 33(31):9245–9256, Aug 1994.
- [32] K.E. Georgiadis; N.I. Jhon; O. Einarsdóttir. Time-resolved optical absorption studies of intramolecular electron transfer in cytochrome c oxidase. *Biochemistry*, 33(31):9245–9256, Aug 1994.
- [33] K.M. Eyster. The membrane and lipids as integral participants in signal transduction: lipid signal transduction for the non-lipid biochemist. *Adv. Physiol. Educ.*, 31(1):5–16, Mar 2007.
- [34] A. J. Bard; L. R. Faulkner. *Electrochemical Methods: Fundamentals and Applications*. John Wiley & Sons, Inc, 2001, 2nd Edition.
- [35] C. Hiser; D. A. Mills; M. Schall; S. Ferguson-Miller. C-terminal truncation and histidine-tagging of cytochrome c oxidase subunit II reveals the native processing site, shows involvement of the C-terminus in cytochrome c binding, and improves the assay for proton pumping. *Biochemistry*, 40(6):1606–1615, Feb 2001.
- [36] D.A. Mills; S. Ferguson-Miller. Influence of structure, pH and membrane potential on proton movement in cytochrome oxidase. *Biochim. Biophys. Acta*, 1555(1-3):96–100, Sep 2002.
- [37] L. Qin; J. Liu; D.A. Mills; D.A. Proshlyakov; C. Hiser; S. Ferguson-Miller. Redox-dependent conformational changes in cytochrome C oxidase suggest a gating mechanism for proton uptake. *Biochemistry*, 48(23):5121–5130, Jun 2009.
- [38] L. Qin; J. Liu; D.A. Mills; D.A. Proshlyakov; C. Hiser; S. Ferguson-Miller. Redox-dependent conformational changes in cytochrome C oxidase suggest a gating mechanism for proton uptake. *Biochemistry*, 48(23):5121–5130, Jun 2009.
- [39] R. Gennis; S. Ferguson-Miller. Structure of cytochrome c oxidase, energy generator of aerobic life. *Science*, 269(5227):1063–1064, Aug 1995.
- [40] D.E. Green; S. Fleischer. The role of lipids in mitochondrial electron transfer and oxidative phosphorylation. *Biochim. Biophys. Acta*, 70:554–582, Oct 1963.
- [41] F. A. Armstrong; J. C. Fontecilla-Camps. Biochemistry. A natural choice for activating hydrogen. *Science*, 321:498–499, 2008.
- [42] C.A. Naumann; W. Knoll; C.W. Frank. Hindered diffusion in polymer-tethered membranes: a monolayer study at the air-water interface. *Biomacromolecules*, 2(4):1097–1103, 2001.
- [43] J. Crum; K. J. Gruys; T. G. Frey. Electron microscopy of cytochrome c oxidase crystals: labeling of subunit III with a monomaleimide undecagold cluster compound. *Biochemistry*, 33(46):13719–13726, Nov 1994.
- [44] T. Ohnishi; R. LoBrutto; J.C. Salerno; R.C. Bruckner; T.G. Frey. Spatial relationship between cytochrome a and a<sub>3</sub>. *J. Biol. Chem.*, 257(24):14821–14825, Dec 1982.

- [45] H. Fricke. The electric capacity of suspensions with special reference to blood. *J. Gen. Physiol.*, 9(2):137–152, Nov 1925.
- [46] M. Friedrich. *Vibrational Spectroscopic and Electrochemical Investigations of Multi-centered Heme Proteins in Biomimetic Membrane Architectures*. PhD thesis, Johannes Gutenberg Universität Mainz, 2007.
- [47] J. G. Antonini; M. Brunori; A. Colosimo; F. Malatesta; P. Sarti. Pulsed cytochrome c oxidase. *J. Inorg. Biochem.*, 23:289–293, 1985.
- [48] D. Zaslavsky; R. B. Gennis. Proton pumping by cytochrome oxidase: progress, problems and postulates. *Biochim. Biophys. Acta*, 1458(1):164–179, May 2000.
- [49] J. Hemp; R.B. Gennis. Diversity of the heme-copper superfamily in archaea: insights from genomics and structural modeling. *Results Probl. Cell Differ.*, 45:1–31, 2008.
- [50] J.P. Shapleigh; J.J. Hill; J.O. Alben; R.B. Gennis. Spectroscopic and genetic evidence for two heme-Cu-containing oxidases in *Rhodobacter sphaeroides*. *J. Bacteriol.*, 174(7):2338–2343, Apr 1992.
- [51] J.P. Shapleigh; R.B. Gennis. Cloning, sequencing and deletion from the chromosome of the gene encoding subunit I of the aa3-type cytochrome c oxidase of *Rhodobacter sphaeroides*. *Mol. Microbiol.*, 6(5):635–642, Mar 1992.
- [52] M. W. Calhoun; J. W. Thomas; R. B. Gennis. The cytochrome oxidase superfamily of redox-driven proton pumps. *Trends Biochem. Sci.*, 19(8):325–330, Aug 1994.
- [53] M. F. Bauer; K. Gempel; S. Hofmann; M. Jaksch; C. Philbrook; K. D. Gerbitz. Mitochondrial disorders. a diagnostic challenge in clinical chemistry. *Clin. Chem. Lab. Med.*, 37(9):855–876, Sep 1999.
- [54] A.E. Vallejo; C.A. Gervasi. *Advances in Planar Lipid Bilayers and Liposomes, Vol. 3*, chapter 10, On the Use of Impedance Spectroscopy for Studying Bilayer Lipid Membranes, pages 331–353. Elsevier, 2006.
- [55] K. Gerwert. *Infrared and Raman Spectroscopy of Biological Materials: Chapter 6, "Time-Resolved FT-IR Difference Spectroscopy: A Tool to Monitor Molecular Reaction Mechanisms of Proteins"*. Marcel Dekker, Inc., Basel, 2001.
- [56] A.K. Udit; M.G. Hill; H.B. Gray. *Langmuir*, 22:10854, 2006.
- [57] B.E. Ramirez; B.G. Malmström; J.R. Winkler; H.B. Gray. The currents of life: the terminal electron-transfer complex of respiration. *Proc. Natl. Acad. Sci. USA*, 92(26):11949–11951, Dec 1995.
- [58] B.C.Hill; C. Greenwood. The reaction of fully reduced cytochrome c oxidase with oxygen studied by flow-flash spectrophotometry at room temperature. *Biochem. J.*, 218:913–21, 1984.
- [59] Z. Zheng; M.R. Gunnar. Analysis of the electrochemistry of hemes with Ems spanning 800 mV. *Proteins*, 75:719–34, 2009.



## REFERENCES

---

- [60] Y. Hatefi. The mitochondrial electron transport and oxidative phosphorylation system. *Annu. Rev. Biochem.*, 54:1015–1069, 1985.
- [61] D. Heitbrink; H. Sigurdson; C. Bolwien; P. Brzezinski; J. Heberle. Transient binding of CO to Cu(B) in cytochrome c oxidase is dynamically linked to structural changes around a carboxyl group: a time-resolved step-scan Fourier transform infrared investigation. *Biophys. J.*, 82:1, 2002.
- [62] R.M. Nyquist; D. Heitbrink; C. Bolwien; R.B. Gennis; J. Heberle. Direct observation of protonation reactions during the catalytic cycle of cytochrome c oxidase. *PNAS USA*, 100:8715–20, 2003.
- [63] R.M. Nyquist; D. Heitbrink; C. Bolwien; T.A. Wells; R.B. Gennis; J. Heberle. Perfusion-induced redox differences in cytochrome c oxidase: ATR/FT-IR spectroscopy. *FEBS Lett*, 505:63–67, 2001.
- [64] J. Behr; H. Michel; W. Mantele; P. Hellwig. Functional properties of the heme propionates in cytochrome c oxidase from *paracoccus denitrificans*. evidence from ftir difference spectroscopy and site-directed mutagenesis. *Biochemistry*, 39:1356–63, 2000.
- [65] J. Castresana; M. Lübben; M. Saraste; D. G. Higgins. Evolution of cytochrome oxidase, an enzyme older than atmospheric oxygen. *EMBO J.*, 13(11):2516–2525, Jun 1994.
- [66] M.G. Friedrich; F. Giebeta; R. Naumann; W. Knoll; K. Ataka; J. Heberle; J. Hrabakova; D.H. Murgida; P. Hildebrandt. Active site structure and redox processes of cytochrome c oxidase immobilised in a novel biomimetic lipid membrane on an electrode. *Chem. Commun. (Camb)*, 21(21):2376–2377, Nov 2004.
- [67] A.K. Udit; K.D. Hagen; P.J. Goldman; A. Star; J.M. Gillan; H.B. Gray; M.G. Hill. *Journal of the American Chemical Society*, 128:10320, 2006.
- [68] B.C. Hill. Modeling the sequence of electron transfer reactions in the single turnover of reduced, mammalian cytochrome c oxidase with oxygen. *J. Biol. Chem.*, 269:2419–25, 1994.
- [69] T.L. Hill. *Free Energy Transduction in Biology*. Acad. Press, New York, 1977.
- [70] M. Tsubaki; K. Matsushita; O. Adachi; S. Hirota; T. Kitagawa; H. Hori. Resonance Raman, infrared, and EPR investigation on the binuclear site structure of the heme-copper ubiquinol oxidases from *Acetobacter acetii*: effect of the heme peripheral formyl group substitution. *Biochemistry*, 36(42):13034–13042, Oct 1997.
- [71] <http://orgchem.colorado.edu/hndbksupport/irtutor/tutorial.html>.
- [72] <http://www.biocenter.helsinki.fi/bi/biophys>.
- [73] <http://www.wag.caltech.edu/home/jang/genchem/infrared.htm>.
- [74] C. Lange; J.H. Nett; B.L. Trumpower; C. Hunte. Specific roles of protein-phospholipid interactions in the yeast cytochrome bc<sub>1</sub> complex structure. *EMBO J*, 20(23):6591–6600, Dec 2001.

## REFERENCES

---

- [75] A.G. Marr; J.L. Ingraham. Effect of temperature on the composition of fatty acids in *Escherichia coli*. *J. Bacteriol.*, 84(6):1260–1267, Dec 1962.
- [76] E.P. Carpenter; K. Beis; A.D. Cameron; S. Iwata. Overcoming the challenges of membrane protein crystallography. *Curr. Opin. Struct. Biol.*, 18(5):581–586, Oct 2008.
- [77] M. Svensson-Ek; J. Abramson; G. Larsson; S. Tornroth; P. Brzezinski; S. Iwata. The X-ray crystal structures of wild-type and EQ(I-286) mutant cytochrome c oxidases from *Rhodobacter sphaeroides*. *J. Molec. Biol.*, 321:329–339, 2002.
- [78] H. Michel; J. Behr; A. Harrenga; A. Kannt. Cytochrome c oxidase: structure and spectroscopy. *Annu. Rev. Biophys. Biomol. Struct.*, 27:329–356, 1998.
- [79] D. Keilin. On cytochrome, a respiratory pigment, common to animals, yeast, and higher plants. *Proc. R. Soc. B*, 100:129–151, 1925.
- [80] R. Mascarenhas; Y.H. Wei; C.P. Scholes; T.E. King. Interaction in cytochrome c oxidase between cytochrome a<sub>3</sub> ligated with nitric oxide and cytochrome a. *J. Biol. Chem.*, 258(9):5348–5351, May 1983.
- [81] V.U. Kirste. *Elektrochemisch gesteuerte zeitaufgelöste Infrarotspektroskopie an Redox-Membranproteinen in einer Biomimetrischen Membran-Architektur*. PhD thesis, Fachbereich Chemie, Pharmazie und Geowissenschaften der Johannes Gutenberg Universität, Mainz, 2007.
- [82] D. A. Proshlyakov; T. Ogura; K. Shinzawa-Itoh; S. Yoshikawa; T. Kitagawa. Resonance Raman/absorption characterization of the oxo intermediates of cytochrome c oxidase generated in its reaction with hydrogen peroxide: pH and H<sub>2</sub>O<sub>2</sub> concentration dependence. *Biochemistry*, 35(26):8580–8586, Jul 1996.
- [83] D. Okuno; T. Iwase; K. Shinzawa-Itoh; S. Yoshikawa; T. Kitagawa. FTIR detection of protonation/deprotonation of key carboxyl side chains caused by redox change of the Cu(A)-heme a moiety and ligand dissociation from the heme a<sub>3</sub>-Cu(B) center of bovine heart cytochrome c oxidase. *J. Am. Chem. Soc.*, 125:7209–18, 2003.
- [84] D.A. Proshlyakov; T. Ogura; K. Shinzawa-Itoh; S. Yoshikawa; T. Kitagawa. Microcirculating system for simultaneous determination of Raman and absorption spectra of enzymatic reaction intermediates and its application to the reaction of cytochrome c oxidase with hydrogen peroxide. *Biochemistry*, 35(1):76–82, Jan 1996.
- [85] T. Ogura; S. Hirota; D.A. Proshlyakov; K. Shinzawa-Itoh; S. Yoshikawa; T. Kitagawa. Time-Resolved Resonance Raman Evidence for Tight Coupling between Electron Transfer and Proton Pumping of Cytochrome c Oxidase upon the Change from the Fe<sup>IV</sup> Oxidation Level to the Fe<sup>V</sup> Oxidation Level. *J. Am. Chem. Soc.*, 118:5443–5449, 1996.
- [86] Y. Kim; K. Shinzawa-Itoh; S. Yoshikawa; T. Kitagawa. Presence of the heme-oxo intermediate in oxygenation of carbon monoxide by cytochrome c oxidase revealed by resonance Raman spectroscopy. *J. Am. Chem. Soc.*, 123:757, 2001.

- [87] E. Klimov. *Zeitaufgelöste Step-Scan FT-IR Spektroskopie niedermolekularer nematischer Flüssigkristalle im elektrischen Wechselfeld*. PhD thesis, Universität Duisburg-Essen, Fachbereich Chemie, 2003.
- [88] F. Giess; M.G. Friedrich; J. Heberle; R.L. Naumann; W. Knoll. The protein-tethered lipid bilayer: a novel mimic of the biological membrane. *Biophys. J.*, 87(5):3213–3220, Nov 2004.
- [89] S.M. Schiller; R. Naumann; K. Lovejoy; H. Kunz; W. Knoll. Archaea analogue thiolipids for tethered bilayer lipid membranes on ultrasmooth gold surfaces. *Angew. Chem. Int. Ed. Engl.*, 42(2):208–211, Jan 2003.
- [90] V.A. Kosobukin. Effect of enhancement of external electric field near metal surface and its manifestation in spectroscopy. *Surface. Physics, chemistry, mechanics*, 12:5–20, 1983.
- [91] V.A. Kosobukin. *Reports of Academy of Sciences of USSR, Physical edition*, 48(7):1281–1288, 1984.
- [92] V.A. Kosobukin. Collective modes in enhancement of external electric field on the surface of the metals. *Reports of Academy of Sciences of USSR, Physical edition*, 49(6):1111–1120, 1985.
- [93] E. Kretschmann. Die Bestimmung optischer Konstanten von Metallen durch Anregung von Oberflächenplasmaschwingungen. *Z.Phys.*, 241:313, 1971.
- [94] S. Fleischer; G. Rouser; B. Fleischer; A. Casu; G. Kritchevsky. Lipid composition of mitochondria from bovine heart, liver, and kidney. *J. Lipid Res.*, 8(3):170–180, May 1967.
- [95] M.L. Latash. *Neurophysiological basis of movement*. Human Kinetics Publishers, 2007.
- [96] H. Lauer. *Die molekulare Architektur von Thiopeptid- und Thiolipopeptidmonoschichten auf Goldoberflächen und ihre Verwendung als Spacersysteme für festkörpergestützte Lipiddoppelschichten*. PhD thesis, Johannes Gutenberg Universität Mainz, 2001.
- [97] E. Laviron. Voltammetric methods for the study of adsorbed species. in: *A.J. Bard (Ed.), Electroanal. Chem.: A Series of Advances, Marcel Dekker, New York*, 12:53, 1982.
- [98] A.G. Lee. How lipids affect the activities of integral membrane proteins. *Biochim. Biophys. Acta*, 1666(1-2):62–87, Nov 2004.
- [99] B. Brügger; G. Erben; R. Sandhoff; F. T. Wieland; W. D. Lehmann. Quantitative analysis of biological membrane lipids at the low picomole level by nano-electrospray ionization tandem mass spectrometry. *PNAS*, 94(6):2339–2344, Mar 1997.
- [100] B. Chance; C. Saronio; J. S. Leigh. Functional intermediates in the reaction of membrane-bound cytochrome oxidase with oxygen. *J. Biol. Chem.*, 250(24):9226–9237, Dec 1975.

## REFERENCES

---

- [101] O.M. Richter; B. Ludwig. Cytochrome c oxidase—structure, function, and physiology of a redox-driven molecular machine. *Rev. Physiol. Biochem. Pharmacol.*, 147:47–74, 2003.
- [102] P. Hellwig; A. Boehm; U. Pfitzner; W. Maentele; B. Ludwig. Spectroscopic study on the communication between a heme a<sub>3</sub> propionate, Asp399 and the binuclear center of cytochrome c oxidase from *Paracoccus denitrificans*. *BBA-Bioenergetics*, 1777:220, 2008.
- [103] R.W. Hendler; K. Pardhasaradhi; B. Reynafarje; B. Ludwig. Comparison of energy-transducing capabilities of the two- and three-subunit cytochromes aa<sub>3</sub> from *Paracoccus denitrificans* and the 13-subunit beef heart enzyme. *Biophys. J.*, 60(2):415–423, Aug 1991.
- [104] A. Colosimo F. Malatesta P. Sarti M. G. Jones M. T. Wilson M. Brunori, G. Antonini. *J. Inorg. Biochem.*, 23:373–379, 1985.
- [105] P. Hellwig; T. Soulimane; W. Maentele. Electrochemical, FT-IR and UV/VIS spectroscopic properties of the caa<sub>3</sub> oxidase from *T. thermophilus*. *Eur. J. Biochem.*, 269:4830–38, 2002.
- [106] B. G. Malmström. Enzymology of oxygen. *Annu. Rev. Biochem.*, 51:21–59, 1982.
- [107] J.J. Regan; B.E. Ramirez; J.R. Winkler; H.B. Gray; B.G. Malmström. Pathways for electron tunneling in cytochrome c oxidase. *J. Bioenerg. Biomembr.*, 30(1):35–39, Feb 1998.
- [108] M. Oliveberg; P. Brzezinski; B.G. Malmström. The effect of pH and temperature on the reaction of fully reduced and mixed-valence cytochrome c oxidase with dioxygen. *Biochim. Biophys. Acta*, 977:322–28, 1989.
- [109] P. Brzezinski; B. G. Malmström. The mechanism of electron gating in proton pumping cytochrome c oxidase: the effect of pH and temperature on internal electron transfer. *BBA - Bioenergetics*, 894(1):29–38, Oct 1987.
- [110] P. Hellwig; B. Rost; U. Kaiser; C. Ostermeier; H. Michel; W. Mantele. Carboxyl group protonation upon reduction of the *Paracoccus denitrificans* cytochrome c oxidase: direct evidence by FTIR spectroscopy. *FEBS Lett.*, 385:53–57, 1996.
- [111] S. Ferguson-Miller; D. L. Brautigan; E. Margoliash. Correlation of the kinetics of electron transfer activity of various eukaryotic cytochromes c with binding to mitochondrial cytochrome c oxidase. *J. Biol. Chem.*, 251(4):1104–1115, Feb 1976.
- [112] S. Ferguson-Miller; D. L. Brautigan; E. Margoliash. Definition of cytochrome c binding domains by chemical modification. III. Kinetics of reaction of carboxydinitrophenyl cytochromes c with cytochrome c oxidase. *J. Biol. Chem.*, 253(1):149–159, Jan 1978.
- [113] J.E.A. McIntosh; R.P. McIntosh. *Mathematical Modelling and Computers in Endocrinology*. Springer Verlag, Berlin, Heidelberg, New York, 1980.
- [114] H. Michel. The mechanism of proton pumping by cytochrome c oxidase. *Proc. Natl. Acad. Sci. USA*, 95(22):12819–12824, Oct 1998.

## REFERENCES

---

- [115] J. Koepke; E. Olkhova; H. Angerer; H. Müller; G. Peng; H. Michel. High resolution crystal structure of *Paracoccus denitrificans* cytochrome c oxidase: new insights into the active site and the proton transfer pathways. *Biochim. Biophys. Acta*, 1787(6):635–645, Jun 2009.
- [116] S. Iwata; C. Ostermeier; B. Ludwig; H. Michel. Structure at 2.8 Å resolution of cytochrome c oxidase from *Paracoccus denitrificans*. *Nature*, 376(6542):660–669, Aug 1995.
- [117] D. Walz; S. R. Caplan; D. R. L. Scriven; D. Mikulecky. *Bioelectrochemistry: General Introduction*. Birkhäuser, Basel, 1995.
- [118] R.A. Capaldi; V. Darley-USmar; S. Fuller; F. Millett. Structural and functional features of the interaction of cytochrome c with complex III and cytochrome c oxidase. *FEBS Lett.*, 138(1):1–7, Feb 1982.
- [119] P. Mitchell. Coupling of phosphorylation to electron and hydrogen transfer by a chemi-osmotic type of mechanism. *Nature*, 191:144–148, Jul 1961.
- [120] P. Mitchell. Chemiosmotic coupling in oxidative and photosynthetic phosphorylation. *Biol. Rev. Camb. Philos. Soc.*, 41(3):445–502, Aug 1966.
- [121] P. Hellwig; C. Ostermeier; H. Michel; B. Ludwig; W. Mäntele. Electrochemically induced FT-IR difference spectra of the two- and four-subunit cytochrome c oxidase from *P. denitrificans* reveal identical conformational changes upon redox transitions. *Biochim. Biophys. Acta*, 1409(2):107–112, Dec 1998.
- [122] P. Hellwig; J. Behr; C. Ostermeier; O. M. Richter; U. Pfitzner; A. Odenwald; B. Ludwig; H. Michel; W. Mäntele. Involvement of glutamic acid 278 in the redox reaction of the cytochrome c oxidase from *Paracoccus denitrificans* investigated by FTIR spectroscopy. *Biochemistry*, 37(20):7390–7399, May 1998.
- [123] P. Hellwig; S. Grzybek; J. Behr; B. Ludwig; H. Michel; W. Mäntele. Electrochemical and ultraviolet/visible/infrared spectroscopic analysis of heme a and a<sub>3</sub> redox reactions in the cytochrome c oxidase from *Paracoccus denitrificans*: separation of heme a and a<sub>3</sub> contributions and assignment of vibrational modes. *Biochemistry*, 38(6):1685–1694, Feb 1999.
- [124] P. Hellwig; T. Soulimane; W. Mäntele. Electrochemical, FT-IR and UV/VIS spectroscopic properties of the caa3 oxidase from *T. thermophilus*. *Eur. J. Biochem.*, 269(19):4830–4838, Oct 2002.
- [125] R. Bisson; G. Schiavo; C. Montecucco. ATP induces conformational changes in mitochondrial cytochrome c oxidase. Effect on the cytochrome c binding site. *J. Biol. Chem.*, 262(13):5992–5998, May 1987.
- [126] M. Wikström; J.E. Morgan. The dioxygen cycle. Spectral, kinetic, and thermodynamic characteristics of ferryl and peroxy intermediates observed by reversal of the cytochrome oxidase reaction. *J. Biol. Chem.*, 267(15):10266–10273, May 1992.
- [127] J. Raba; H.A. Mottola. Glucose Oxidase as an Analytical Reagent. *Crit. Rev. Anal. Chem.*, 25(1):1–42, 1995.

## REFERENCES

---

- [128] T.G. Frey; J.M. Murray. Electron microscopy of cytochrome c oxidase crystals. Monomer-dimer relationship and cytochrome c binding site. *J. Mol. Biol.*, 237(3):275–297, Apr 1994.
- [129] C. Nowak; C. Luening; D. Schach; D. Baurecht; W. Knoll; R.L.C. Naumann. Electron Transfer Kinetics of Cytochrome C in the Submillisecond Time Regime Using Time-Resolved Surface-Enhanced Infrared Absorption Spectroscopy. *J. Phys. Chem. C*, 113(6):2256–2262, 2009.
- [130] C. Nowak; C. Luening; W. Knoll; R. L. C. Naumann. A Two-Layer Gold Surface with Improved Surface Enhancement for Spectro-Electrochemistry Using Surface-Enhanced Infrared Absorption Spectroscopy. *Appl. Spectr.*, 63:1068–1074, 2009.
- [131] C. Nowak; D. Schach; J. Gebert; M. Grosserueschkamp; R.B. Gennis; S. Ferguson-Miller; W. Knoll; D. Walz; R.L.C. Naumann. Oriented immobilization and electron transfer to the cytochrome c oxidase. *J. Solid State Electrochem.*, 15:105–114, 2010.
- [132] C. Nowak; M. G. Santonicola; D. Schach; J. P. Zhu; R. B. Gennis; S. Ferguson-Miller; D. Baurecht; D. Walz; W. Knoll; R. L. C. Naumann. Conformational transitions and molecular hysteresis of cytochrome c oxidase: Varying the redox state by electronic wiring. *Soft Matter*, 6:5523–5532, 2010.
- [133] M.G. Friedrich; J.W.F. Robertson; D. Walz; W. Knoll; R.L.C. Naumann. Electronic wiring of a multi-redox site membrane protein in a biomimetic surface architecture. *Biophys. J.*, 94(9):3698–3705, May 2008.
- [134] M.G. Friedrich; M.A. Plum; M.G. Santonicola; V.U. Kirste; W. Knoll; B. Ludwig; R.L.C. Naumann. In situ monitoring of the catalytic activity of cytochrome C oxidase in a biomimetic architecture. *Biophys. J.*, 95(3):1500–1510, Aug 2008.
- [135] M.G. Friedrich; V.U. Kirste; J. Zhu; R.B. Gennis; W. Knoll; R.L.C. Naumann. Activity of membrane proteins immobilized on surfaces as a function of packing density. *J. Phys. Chem. B*, 112(10):3193–3201, Mar 2008.
- [136] S.J. Singer; G.L. Nicolson. The fluid mosaic model of the structure of cell membranes. *Science*, 175(23):720–731, Feb 1972.
- [137] K. Muramoto; K. Hirata; K. Shinzawa-Itoh; S. Yokoyama; E. Yamashita; H. Aoyama; T. Tsukihara; S. Yoshikawa. A histidine residue acting as a controlling site for dioxygen reduction and proton pumping by cytochrome c oxidase. *Proc. Natl. Acad. Sci. USA*, 104(19):7881–7886, May 2007.
- [138] University of Florida Agricultural and Biological Engineering/ Website of David P. Chynoweth MSPH.
- [139] T. Kitagawa; T. Ogura. *Oxygen Activation Mechanism at the Binuclear Site of Heme-Copper Oxidase Superfamily as Revealed by Time-Resolved Resonance Raman Spectroscopy*. *Progr. Inorg. Chem.*, Volume 45, 1997.
- [140] T. Tsudzuki; K. Okunuki. EPR studies on cytochrome oxidase at 20 degree K. *J. Biochem.*, 66(2):281–283, Aug 1969.

## REFERENCES

---

- [141] F. Gao; H. Qin; D.B. Knaff; L. Zhang; L. Yu; C. A. Yu; M. R. Ondrias. Q-band resonance Raman spectra of oxidized and reduced mitochondrial bc<sub>1</sub> complexes. *Biochemistry*, 37(27):9751–9758, Jul 1998.
- [142] I. A. Balabin; J. N. Onuchic. Dynamically controlled protein tunneling paths in photosynthetic reaction centers. *Science*, 290(5489):114–117, Oct 2000.
- [143] M.-L. Tan; I. Balabin; J.N. Onuchic. Dynamics of electron transfer pathways in cytochrome c oxidase. *Biophys. J.*, 86(3):1813–1819, Mar 2004.
- [144] Y. Orii. Intermediates in the reaction of reduced cytochrome oxidase with dioxygen. *Ann. N.Y. Acad. Sci.*, 550:105–17, 1988.
- [145] A. Otto. Excitation of nonradiative surface plasma waves in silver by the method of frustrated total reflection. *Z.Phys*, 216:398–410, 1968.
- [146] O. Farver; O. Einarsdóttir; I. Pecht. Electron transfer rates and equilibrium within cytochrome c oxidase. *Eur. J. Biochem.*, 267(4):950–954, Feb 2000.
- [147] O. Farver; O. Einarsdóttir; I. Pecht. Electron transfer rates and equilibrium within cytochrome c oxidase. *Eur. J. Biochem.*, 267:950–4, 2000.
- [148] H. Muirhead; M.F. Perutz. Structure of haemoglobin. A three-dimensional Fourier synthesis of reduced human haemoglobin at 5.5 Å resolution. *Nature*, 199:633–638, Aug 1963.
- [149] J.C. Kendrew; G. Bodo; H.M. Dintzis; R.G. Parrish; H. Wyckoff; D.C. Phillips. A three-dimensional model of the myoglobin molecule obtained by x-ray analysis. *Nature*, 181(4610):662–666, Mar 1958.
- [150] R. Palmer; J. Chao; R. Dittmar; V. Gregoriou; S. Plunkett. Investigation of Time-Dependent Phenomena by Use of Step-Scan FT-IR. *Appl. Spectrosc.*, 47(9):1297–1310, 1993.
- [151] H. Raether. *Surface Plasmons*. Springer Verlag, 1988.
- [152] J.v. Koolman; K.-H. Röhm. *Color Atlas of Biochemistry*. Thieme, 2005.
- [153] A.J. Moody; U. Brandt; P.R. Rich. Single electron reduction of 'slow' and 'fast' cytochrome-c oxidase. *FEBS Lett.*, 293(1-2):101–105, Nov 1991.
- [154] R. Mitchell; P. R. Rich. Proton uptake by cytochrome c oxidase on reduction and on ligand binding. *Biochim. Biophys. Acta*, 1186(1-2):19–26, Jun 1994.
- [155] B. Ludwig; M. Grabo; I. Gregor; A. Lustig; M. Regenass; J.P. Rosenbusch. Solubilized cytochrome c oxidase from *Paracoccus denitrificans* is a monomer. *J. Biol. Chem.*, 257(10):5576–5578, May 1982.
- [156] S. Han; Y.C. Ching; D.L. Rousseau. Ferryl and hydroxy intermediates in the reaction of oxygen with reduced cytochrome c oxidase. *Nature*, 348(6296):89–90, Nov 1990.

## REFERENCES

---

- [157] H. Wienk; O. Maneg; C. Lücke; P. Pristovsek; F. Löhr; B. Ludwig; H. Rüterjans. Interaction of cytochrome c with cytochrome c oxidase: an NMR study on two soluble fragments derived from *Paracoccus denitrificans*. *Biochemistry*, 42(20):6005–6012, May 2003.
- [158] M. Ruitenber. *Elektronen- und Protonentransport der Cytochrom c Oxidase aus Paracoccus Denitrificans*. PhD thesis, Johann Wolfgang Goethe-Universität in Frankfurt am Main, 2001.
- [159] O. Salomon. *Charakterisierung des Ladungstransfers von immobilisiertem Cytochrom c*. PhD thesis, RWTH Aachen, 2006.
- [160] M. Wikstrom; K. Krab; M. Saraste. *Cytochrome Oxidase: A synthesis*. New York: Academic, 1981.
- [161] E. Hochuli; H. Döbeli; A. Schacher. New metal chelate adsorbent selective for proteins and peptides containing neighbouring histidine residues. *J. Chromatogr.*, 411:177–184, Dec 1987.
- [162] B. Ludwig; G. Schatz. A two-subunit cytochrome c oxidase (cytochrome aa3) from *Paracoccus denitrificans*. *Proc. Natl. Acad. Sci. USA*, 77(1):196–200, Jan 1980.
- [163] S. DiMauro; E.A. Schon. Mitochondrial disorders in the nervous system. *Ann. Rev. Neurosci.*, 31:91–123, 2008.
- [164] R. A. Scott. Functional significance of cytochrome c oxidase structure. *Structure*, 3(10):981–986, Oct 1995.
- [165] A. Seelig; J. Seelig. Phospholipid composition and organization of cytochrome c oxidase preparations as determined by  $^{31}\text{P}$ -nuclear magnetic resonance. *Biochim. Biophys. Acta*, 815(2):153–158, May 1985.
- [166] M.A. Kiebish; X. Han; H. Cheng; J.H. Chuang; T.N. Seyfried. Cardiolipin and electron transport chain abnormalities in mouse brain tumor mitochondria: lipidomic evidence supporting the Warburg theory of cancer. *J. Lipid. Res.*, 49(12):2545–2556, Dec 2008.
- [167] S. Yoshikawa; T. Tsukihara; K. Shinzawa-Itoh. Crystal structure of fully oxidized cytochrome c-oxidase from the bovine heart at 2.8 Å resolution. *Biokhimiia*, 61(11):1931–1940, Nov 1996.
- [168] S.J. Singer. A fluid lipid-globular protein mosaic model of membrane structure. *Ann. N. Y. Acad. Sci.*, 195:16–23, Jun 1972.
- [169] S.J. Ferguson; M.C. Sorgato. Proton electrochemical gradients and energy-transduction processes. *Annu. Rev. Biochem.*, 51:185–217, 1982.
- [170] J.M. Berg; J.L. Tymoczko; L. Stryer. *Biochemie*. Spektrum Akademischer Verlag, 2003.
- [171] D.M. Medvedev; I. Daizadeh; A.A. Stuchebrukhov. Electron Transfer Tunneling Pathways in Bovine Heart Cytochrome c Oxidase. *J. Am. Chem. Soc.*, 122(28):6571–6582, 2000.



## REFERENCES

---

- [172] I. Daizadeh; D.M. Medvedev; A.A. Stuchebrukhov. Electron transfer in ferredoxin: are tunneling pathways evolutionarily conserved? *Mol. Biol. Evol.*, 19(4):406–415, Apr 2002.
- [173] X. Zheng; D.M. Medvedev; J. Swanson; A.A. Stuchebrukhov. Computer simulation of water in cytochrome c oxidase. *Biochim. Biophys. Acta*, 1557(1-3):99–107, Mar 2003.
- [174] A. Wisniewska; J. Draus; W.K. Subczynski. Is a fluid-mosaic model of biological membranes fully relevant? Studies on lipid organization in model and biological membranes. *Cell Mol. Biol. Lett.*, 8(1):147–159, 2003.
- [175] H. Susi. *Structure and Stability of Biological Macromolecules.*, pages 575–663. Dekker, 1969.
- [176] O. Einarsdóttir; I. Szundi. Time-resolved optical absorption studies of cytochrome oxidase dynamics. *Biochim. Biophys. Acta*, 1655(1-3):263–273, Apr 2004.
- [177] R. Nakashima; R. Yaono; S. Yoshikawa T. Tsukihara; H. Aoyama; E. Yamashita; T. Tomizaki; H. Yamaguchi; K. Shinzawa-Itoh. The whole structure of the 13-subunit oxidized cytochrome c oxidase at 2.8 Å. *Science*, 272(5265):1136–1144, May 1996.
- [178] M.M. Pereira; M. Santana; M. Teixeira. A novel scenario for the evolution of haem-copper oxygen reductases. *Biochim. Biophys. Acta*, 1505(2-3):185–208, Jun 2001.
- [179] D.H. Murgida; P. Hildebrandt; S. Todorovic. *Biomimetics Learning from Nature*, chapter Immobilized Redox Proteins: Mimicking Basic Features of Physiological Membranes and Interfaces, pages 21–48. InTech, 2010.
- [180] T. Nakano; T. Yokoyama; H. Toriumi. One- and Two-Dimensional Infrared Time-Resolved Spectroscopy Using a Step-Scan FT-IR Spectrometer: Application to the Study of Liquid Crystal Reorientation Dynamics. *Appl. Spectr.*, 47:1354–1366, 1993.
- [181] E. A. Berry; B. L. Trumpower. Isolation of ubiquinol oxidase from *paracoccus denitrificans* and resolution into cytochrome bc<sub>1</sub> and cytochrome c-aa<sub>3</sub> complexes. *J Biol Chem*, 260(4):2458–2467, Feb 1985.
- [182] E. Pinakoulaki; C. Varotsis. Time-resolved resonance Raman and time-resolved step-scan FTIR studies of nitric oxide reductase from *Paracoccus denitrificans*: comparison of the heme b<sub>3</sub>-FeB site to that of the heme-CuB in oxidases. *Biochemistry*, 42(50):14856–14861, Dec 2003.
- [183] E. Pinakoulaki; U. Pfitzner; B. Ludwig; C. Varotsis. The role of the cross-link His-Tyr in the functional properties of the binuclear center in cytochrome c oxidase. *J. Biol. Chem.*, 277:13563–13568, 2002.
- [184] E.A. Gorbikova; K. Vuorilehto; M. Wikström; M.I. Verkhovsky. Redox titration of all electron carriers of cytochrome c oxidase by Fourier transform infrared spectroscopy. *Biochemistry*, 45(17):5641–5649, May 2006.

## REFERENCES

---

- [185] E.A. Gorbikova; K. Vuorilehto; M. Wikstrom; M.I. Verkhovsky. Redox titration of all electron carriers of cytochrome c oxidase by Fourier transform infrared spectroscopy. *Biochemistry*, 45:5641–5649, 2006.
- [186] T.L.W. Bischoff; C. Voit. *Die Gesetze der Ernaehrung des Pflanzenfressers durch neue Untersuchungen festgestellt. Leipzig, Heidelberg.* 1860.
- [187] J.W.F. Robertson; M.G. Friedrich; A. Kibrom; W. Knoll; R.L.C. Naumann; D. Walz. Modeling ion transport in tethered bilayer lipid membranes. 1. Passive ion permeation. *J Phys Chem B*, 112(34):10475–10482, Aug 2008.
- [188] R.K. Hite; T. Gonen; S.C. Harrison; T. Walz. Interactions of lipids with aquaporin-0 and other membrane proteins. *Pflugers. Arch.*, 456(4):651–661, Jul 2008.
- [189] O. Warburg. Iron, the oxygen-carrier of respiration-ferment. *Science*, 61(1588):575–582, Jun 1925.
- [190] J.E. Morgan; M.I. Verkhovsky; M. Wikström. Observation and assignment of peroxy and ferryl intermediates in the reduction of dioxygen to water by cytochrome c oxidase. *Biochemistry*, 35(38):12235–12240, Sep 1996.
- [191] M. Wikström. Identification of the electron transfers in cytochrome oxidase that are coupled to proton-pumping. *Nature*, 338(6218):776–778, Apr 1989.
- [192] M. Wikström. Proton translocation by cytochrome c oxidase: a rejoinder to recent criticism. *Biochemistry*, 39(13):3515–3519, Apr 2000.
- [193] M. Wikström. Cytochrome c oxidase: 25 years of the elusive proton pump. *Biochim. Biophys. Acta*, 1655(1-3):241–247, Apr 2004.
- [194] M. Wikström. Cytochrome c oxidase: 25 years of the elusive proton pump. *Biochim. Biophys. Acta*, 1655(1-3):241–247, Apr 2004.
- [195] M. Wikström. *Cytochrome Oxidase.* John Wiley & Sons, 2006.
- [196] M. Wikström. *Encyclopedia of Life Sciences: "Cytochrome c Oxidase".* John Wiley & Sons, 2010.
- [197] M.I. Verkhovsky; A. Jasaitis; M.L. Verkhovskaya; J.E. Morgan; M. Wikström. Proton translocation by cytochrome c oxidase. *Nature*, 400(6743):480–483, Jul 1999.
- [198] S. Riistama; A. Puustinen; A. García-Horsman; S. Iwata; H. Michel; M. Wikström. Channelling of dioxygen into the respiratory enzyme. *Biochim. Biophys. Acta*, 1275(1-2):1–4, Jul 1996.
- [199] M.K. Wikstrom. Proton pump coupled to cytochrome c oxidase in mitochondria. *Nature*, 266(5599):271–273, Mar 1977.
- [200] M.K. WIKSTROM. Proton pump coupled to cytochrome c oxidase in mitochondria. *Nature*, 266:271–273, 1977.
- [201] M. Winterhalter. Black lipid membranes. *Curr. Opinion Coll. & Interf. Sci.*, 5(3-4):250 – 255, 2000.

## REFERENCES

---

- [202] B.H. McMahon; M. Fabian; F. Tomson; T.P. Causgrove; J.A. Bailey; F.N. Rein; R.B. Dyer; G. Palmer; R.B. Gennis; W.H. Woodruff. FTIR studies of internal proton transfer reactions linked to inter-heme electron transfer in bovine cytochrome c oxidase . *Bba-Bioenergetics*, 1655:321–331, 2004.
- [203] [www.wikipedia.de](http://www.wikipedia.de).
- [204] T. Yonetani. Studies on cytochrome oxidase. III. Improved preparation and some properties. *J. Biol. Chem.*, 236:1680–1688, Jun 1961.
- [205] J.A. Fee; D. Kuila; M.W. Mather; T. Yoshida. Respiratory proteins from extremely thermophilic, aerobic bacteria. *Biochim. Biophys. Acta*, 853(2):153–185, 1986.
- [206] M.J. Fei; E. Yamashita; N. Inoue; M. Yao; H. Yamaguchi; T. Tsukihara; K. Shinzawa-Itoh; R. Nakashima; S. Yoshikawa. X-ray structure of azide-bound fully oxidized cytochrome c oxidase from bovine heart at 2.9 Å resolution. *Acta Crystallogr. D Biol. Crystallogr.*, 56(Pt 5):529–535, May 2000.
- [207] T. Tomizaki; E. Yamashita; H. Yamaguchi; H. Aoyama; T. Tsukihara; K. Shinzawa-Itoh; R. Nakashima; R. Yaono; S. Yoshikawa. Structure analysis of bovine heart cytochrome c oxidase at 2.8 Å resolution. *Acta Crystallogr. D Biol. Crystallogr.*, 55(Pt 1):31–45, Jan 1999.
- [208] T. Tsukihara; H. Aoyama; E. Yamashita; T. Tomizaki; H. Yamaguchi; K. Shinzawa-Itoh; R. Nakashima; R. Yaono; S. Yoshikawa. Structures of metal sites of oxidized bovine heart cytochrome c oxidase at 2.8 Å. *Science*, 269(5227):1069–1074, Aug 1995.
- [209] T.J. Johnson; G. Zachmann. *Introduction to Step-Scan FTIR*. Bruker Optik GmbH, 2000.